

A Study Of Beta-Delayed Deuteron Emission From ${}^6\text{He}$

by

Don Anthony

B.Sc., Simon Fraser University, 1993

A THESIS SUBMITTED IN PARTIAL FULFILLMENT
OF THE REQUIREMENTS FOR THE DEGREE OF
MASTER OF SCIENCE
in the Department
of
Chemistry

© Don Anthony 1995
SIMON FRASER UNIVERSITY
November 1995

All rights reserved. This work may not be
reproduced in whole or in part, by photocopy
or other means, without the permission of the author.



National Library
of Canada

Acquisitions and
Bibliographic Services Branch

395 Wellington Street
Ottawa, Ontario
K1A 0N4

Bibliothèque nationale
du Canada

Direction des acquisitions et
des services bibliographiques

395, rue Wellington
Ottawa (Ontario)
K1A 0N4

Your file *Votre référence*

Our file *Notre référence*

The author has granted an irrevocable non-exclusive licence allowing the National Library of Canada to reproduce, loan, distribute or sell copies of his/her thesis by any means and in any form or format, making this thesis available to interested persons.

The author retains ownership of the copyright in his/her thesis. Neither the thesis nor substantial extracts from it may be printed or otherwise reproduced without his/her permission.

L'auteur a accordé une licence irrévocable et non exclusive permettant à la Bibliothèque nationale du Canada de reproduire, prêter, distribuer ou vendre des copies de sa thèse de quelque manière et sous quelque forme que ce soit pour mettre des exemplaires de cette thèse à la disposition des personnes intéressées.

L'auteur conserve la propriété du droit d'auteur qui protège sa thèse. Ni la thèse ni des extraits substantiels de celle-ci ne doivent être imprimés ou autrement reproduits sans son autorisation.

ISBN 0-612-16774-7

Canada

APPROVAL

Name: Don Anthony
Degree: Master of Science
Title of thesis: A Study Of Beta-Delayed Deuteron Emission From ^6He

Examining Committee: Dr. Fred Einstein
Chair

Dr. John D'Auria
Senior Supervisor
Simon Fraser University

Dr. Ian Gay
Department of Chemistry
Simon Fraser University

Dr. Ralph Korteling
Department of Chemistry
Simon Fraser University

Dr. K. Peter Jackson
Internal/External Examiner
Tri-University Meson Facility (TRIUMF)

Date Approved:


Dec. 6, 1995

PARTIAL COPYRIGHT LICENSE

I hereby grant to Simon Fraser University the right to lend my thesis, project or extended essay (the title of which is shown below) to users of the Simon Fraser University Library, and to make partial or single copies only for such users or in response to a request from the library of any other university, or other educational institution, on its own behalf or for one of its users. I further agree that permission for multiple copying of this work for scholarly purposes may be granted by me or the Dean of Graduate Studies. It is understood that copying or publication of this work for financial gain shall not be allowed without my written permission.

Title of Thesis/Project/Extended Essay:

A Study of Beta-Delayed
Deuteron Emissions from ${}^6\text{He}$

Author: 
(signature)

(name)

Dec. 7th / 95
(date)

Abstract

The decay of ${}^6\text{He}$ has been well studied for its strong ground-state to ground-state, Gamow-Teller beta transition. Recently, the nuclide has been the subject of intense study as it exhibits new, unique decay properties reflecting an exotic nuclear structure. Studies have shown that ${}^6\text{He}$ decays weakly by beta-delayed deuteron emission while other, independent measurements have revealed a halo-like distribution of the ${}^6\text{He}$ neutron matter.

It has been postulated that observable quantities such as the ${}^6\text{He}$ break-up probability and the energy spectrum of the emitted deuterons are sensitive probes of the so-called 'Neutron Halo' phenomenon. However, the two previous determinations of the branching ratio for deuteron emission are not self-consistent and the published particle energy spectra lack the statistical accuracy necessary for conclusive theoretical interpretation.

A recent study conducted at the TRIUMF facility employed a coincidence technique to re-measure the deuteron emission probability and to generate the energy spectra of the emitted particles. The branching ratio for the emission of deuterons above the 350 keV laboratory threshold has been measured to be $(1.9 \pm 0.2 \pm 0.7 * 10^{-6})$ while the deuteron energy spectrum collected with this technique shows a statistical improvement of better than an order of magnitude over those previously reported.

Within this study, K- and R-Matrix nuclear reaction theories have been utilized to estimate the total integrated break-up probability and to understand the observed decay in terms of the anomalous halo structure.

Acknowledgments

The author is extremely grateful for the guidance provided by all members of the TISOL research group. Special thanks to Dr. Ulrich Giesen for his boundless patience, and to Dr. John D'Auria for providing professional, academic, and personal support at every stage of this process. The author would also like to express his appreciation to his parents, David and Marcelle Anthony, friends and other family members for their continuing support and, above all, to Paola – without whom the fruition of this project could never have been realized.

Dedication

To the Memory of Theodore Gladstone Kennedy

Contents

Abstract	iii
Acknowledgments	iv
Dedication	v
List of Tables	vii
List of Figures	viii
1 Introduction	1
1.1 General	1
1.2 Nuclear Structure	1
1.2.1 Tanihata Experiments	3
1.2.2 Kobayashi Experiment	4
1.3 Exotic Decay	5
1.3.1 Branching Ratio	5
1.4 Synthesis	7
1.4.1 Theoretical Models	7
1.5 Summary	9
2 Experiment	11
2.1 Production	11
2.2 Detector End Station	15
2.3 Electronics	17
2.4 Beam Purity	18
3 Particle Energy Spectra	22
3.1 Energy Calibrations	22
3.2 Gadolinium Break Through	28

3.3	${}^6\text{He}$ Particle Energy Correction	28
3.4	Detector Resolution	34
3.5	Particle Identification	34
3.6	Particle Identification (Experimental)	39
3.7	Summary	50
4	Branching Ratio	52
4.1	Introduction	52
4.2	Number of Detected Beta Particles N_β	53
4.3	Beta Conversion Factor β_{con}	54
4.4	Coincidence Efficiency ϵ_c	55
4.5	Number of Detected Deuterons N_d	59
4.6	Ratio of Detection Efficiencies $\epsilon_\beta/\epsilon_d$	59
	4.6.1 Geometric Method	60
	4.6.2 Sources Method	63
	4.6.3 Coincidence Efficiencies Method	70
	4.6.4 Efficiency Ratio Summary	75
4.7	Branching Ratio Results	77
4.8	Systematic Errors	80
	4.8.1 Beta Cut-Off	80
	4.8.2 False Events	81
	4.8.3 Calibration Errors	82
	4.8.4 Geometric Systematic Errors	82
	4.8.5 Detector Non-Linearity	83
	4.8.6 Systematic Error Summary	83
4.9	Branching Ratio Summary	84
5	K-Matrix Analysis	88
5.1	General	88
5.2	K-Matrix Theory	91
	5.2.1 Theoretical Fitting Terms	93
	5.2.2 Theoretical Transition Probability	94
5.3	K-Matrix Fit Results	97

5.4	Total Integrated ($\alpha + d$) Branching Ratio	101
5.5	Published Theoretical Spectra	103
5.6	Summary	109
5.7	R-Matrix Analysis	111
5.7.1	General	111
5.7.2	Analysis	111
5.7.3	Interpretation	112
5.7.4	Summary	116
6	Summary and Conclusions	117

List of Tables

1.1	Theoretical and Experimental ($\alpha + d$) break-up probabilities	10
3.1	Corrected energy of calibration sources due to losses incurred in Carbon, Gold and Gadolinium	24
3.2	ADC channel response to the calibration sources in D1 and D2	26
3.3	Calibration points for particle detectors D1 and D2	26
3.4	Summary of depletion region calibrations based on an assumed linear response	28
3.5	Parameter values for the particle energy correction curves of D1 and D2	33
3.6	Parameter values for particle energy corrections in D1 and D2	33
4.1	Number of detected beta particles	54
4.2	Coincidence efficiency for Detectors D1 and D2 as a function of ${}^6\text{He}$ run number	58
4.3	Number of deuterons detected in D1 and D2 as a function of ${}^6\text{He}$ run number	59
4.4	Parameter values necessary to determine the Geometric efficiency of the various charged particle detectors at station(1)	62
4.5	Geometric solid angle for the various charged particle detectors at station (i)	62
4.6	Half-life fits to beta spectra collected during the ${}^8\text{Li}$ calibration runs .	66
4.7	Fraction of Beta events due to the decay of ${}^8\text{Li}$	68
4.8	Values for parameters necessary to calculate the ratio of efficiencies, $\epsilon_\beta/\epsilon_d$, in the ${}^8\text{Li}$ calibration runs	69

4.9	Ratio of detection efficiencies, $\epsilon_\beta/\epsilon_d$, for each particle detector and ^8Li calibration run	69
4.10	Summary of efficiency ratio calculation derived by the source calibration method	70
4.11	Branching Ratio determinations for Detectors D1 and D2 as a function of ^6He run number	80
4.12	Summary of systematic effects leading to uncertainties in the $(\alpha + d)$ Branching Ratio	83
4.13	Final Branching Ratio results with statistical and systematic errors	84
5.1	K-Matrix fit results to pertinent particle energy spectra	97
5.2	Calculated value of the Integrated $(\alpha + d)$ Branching Ratio	103
5.3	Best fit parameter values for R-Matrix spectra	115

List of Figures

1.1	Energy levels of the mass ($A=6$) isobars	6
2.1	Main features of the TISOL isotope production system	12
2.2	Detector Arrangement and Designations at the three counting stations	16
2.3	Electronics set-up for ${}^6\text{He}$ experiments	19
2.4	Beam Purity half-life test at mass-to-charge ratio ($A = 6$)	21
3.1	Alpha particle's path to detector depletion region	23
3.2	Alpha particle energy losses to detector D2 as a function of energy for ${}^{18}\text{N}$ emissions	25
3.3	Calibration of D2 depletion region based on corrected source energies and D2 ADC response information	27
3.4	ADC response of detector D1 to 3.183 MeV alpha emitted in the decay of ${}^{148}\text{Gd}$	29
3.5	${}^6\text{He}$ alpha particle energy losses in the Carbon foil and Gold layer prior to detection in the calibrated depletion region	31
3.6	High energy polynomial and low energy linear fit to D2 alpha particle, energy correction curve	32
3.7	Detector D1 response to precision pulser signals	35
3.8	Two known branches of the ${}^6\text{He}$ decay	36
3.9	Particle detector response to transmitted betas	38
3.10	Two-dimensional spectrum of coincidence data recorded at detector station (1)	40
3.11	Pulse height ratio spectrum collected at detector station (1)	41

3.12	Pulse height ratio spectrum collected at detector station (1) with the deuteron or acceptance window displayed	43
3.13	Raw deuteron spectrum collected in detector D2 with the acceptance window imposed on the data	44
3.14	Pulse height ratio spectrum collected at detector station (1) with the acceptance window and background window displayed	45
3.15	Raw deuteron spectrum in D2 overlaid by background spectrum collected in D2	46
3.16	Net deuteron spectrum in D2 where the background spectrum has been scaled and subtracted from the raw deuteron spectrum	47
3.17	Four total or raw spectra collected at detector station (1)	48
3.18	Alpha spectra collected in D1 and D2 where the background features have been scaled and subtracted from the raw spectra	49
4.1	The coincidence efficiencies and their dependence on the source/detector geometry	56
4.2	The coincidence efficiency of Detector D2 as a function of ADC channel	57
4.3	General case diagram for relative source/detector geometry	60
4.4	Fit to beta Half-life spectrum assuming contributions from ^8He and ^8Li	67
4.5	Singles and Coincidence geometries as a function of source and detector arrangement	71
4.6	Observed relationship between the coincidence efficiencies of D1 and D2	73
4.7	Branching Ratio results for the data collected in Detector D1	78
4.8	Branching Ratio results for the data collected in Detector D2	79
5.1	Energy region available for $(\alpha + d)$ break-up	90
5.2	K-Matrix fit to deuteron spectrum collected in detector D2	98
5.3	K-Matrix fit to alpha spectrum collected in detector D2	99
5.4	K-Matrix fit to alpha spectrum collected in detector D1	100
5.5	Full theoretical deuteron energy spectrum as derived from the best fit K-Matrix parameters	102

5.6	Comparison of Varga's theoretical deuteron energy spectrum with that collected experimentally	105
5.7	Comparison of Descouvemont's theoretical deuteron energy spectrum with that collected experimentally	106
5.8	Comparison of Zhukov's theoretical deuteron energy spectrum with that collected experimentally	107
5.9	Comparison of Borge's theoretical deuteron energy spectrum with that collected experimentally	108
5.10	Comparison of Barker's theoretical deuteron energy spectrum with that collected experimentally	110
5.11	Theoretical spectrum corresponding to a channel radius of 4.5 fm . .	113
5.12	Theoretical spectrum corresponding to a channel radius of 4.6 fm . .	114

Chapter 1

Introduction

1.1 General

Nuclear science is a branch of chemistry and physics that is fundamentally concerned with the structural, quasi-static and dynamic properties of the atomic nucleus. An important area of research in this field involves the investigation of nuclides that are unstable with respect to nuclear decay. One radioactive nuclide that has become a focus of attention over the last decade is ${}^6\text{He}$. The reason for the renewed interest in the properties of this nuclide is twofold; first, the nuclear structure of ${}^6\text{He}$ has shown non conformity with accepted theoretical models and, second, ${}^6\text{He}$ has recently been observed to exhibit an exotic decay transition that has not been seen in any other nucleus. These two anomalies are discussed separately in the following sections.

1.2 Nuclear Structure

Since Rutherford's famous experiment of 1911 in which he discovered the existence of what we now call the atomic nucleus, the focus of many experimental studies has been to quantify the parameter referred to as the nuclear radius. Even this seemingly discrete quantity is ambiguous. It is important to know whether the quantity being measured by experiment relates to the proton, neutron, or total matter distribution of the nuclear system. Fortunately, different experimental techniques are available

to measure one or another of these quantities independently. For example, coulomb scattering, electron scattering, neutron scattering and isotope shift experiments may be utilized to parameterize either the proton or total matter distribution radii.

When these different experiments were conducted on the same nuclear species, the results obtained for the proton and total matter distributions were found to be in very close agreement. This suggested that, within the nucleus, the protons and neutrons distribute themselves in such a way that the ratio of the number of protons to neutrons is effectively constant over the nuclear volume.

The equivalency between the proton and matter radii is somewhat intuitive when one considers the nucleus as a fluid body. To elaborate; the motion of the nucleons within the nuclear potential is such that the protons and neutrons appear to distribute themselves uniformly throughout the nuclear volume. The effect of a uniform distribution is to minimize the coulombic repulsion experienced by the positively charged protons. It is therefore not surprising that the lowest energy state for any nucleus is to distribute the protons such that over any volume element, dV , the neutron to proton ratio is constant. As a direct consequence of this nucleon ratio uniformity, the charge radius and the matter radius must be equal.

Comparing the results of the nuclear radii over all masses, an important correlation was found. Inspection of the data showed that the nuclear radius is intimately linked to the nuclear mass. It was discovered that over all nuclei, the number of nucleons per unit volume is roughly constant. This equivalency over all nuclei lead to the standard first order radius equation,

$$R = r_0 * A^{1/3} \tag{1.1}$$

where R is the nuclear radius, A is the number of nucleons in the system and r_0 is the constant of proportionality relating the two.

Although experimental evidence exists to suggest that this relationship does not hold below mass ($A=10$), in general terms the linearity of this relationship has been demonstrated repeatedly and the results have formed the basis of many nuclear force and nuclear structure theories.

1.2.1 Tanihata Experiments

Until recently, nuclear radius measurements have been limited to stable or long lived isotopes. However, with the rapid development of radioactive ion beam (RIB) technologies, experiments designed to elucidate the nuclear parameters of unstable species are now feasible. The first comprehensive RIB project developed with these species in mind was performed by Isao Tanihata and his group at Berkeley in 1985 [1]. Their experiments were designed to measure a quantity called the Nuclear Interaction Radius (derived from the cross section observed for the scattering of energetic projectiles) and to convert this parameter into values for the proton, neutron and total matter distribution radii for various short lived species.

The results of these experiments were very surprising, indeed. The investigation of numerous low Z nuclei indicated that some radioactive species have nuclear dimensions, specifically neutron distribution radii, much larger than the first order radius formula predicts. The results showed that the neutron rich isotopes of several low Z elements, including ${}^6\text{He}$, have neutron density distributions up to 30% larger than predicted by theory (${}^{11}\text{Li}$ being the largest). In addition, this experiment reported the first observation of differences in the matter radii among isobars (nuclides with the same number of nucleons). This inequality is a direct contravention of the first order radius equation.

These nuclides have since become known as the Neutron Halo nuclides. The interpretation of the experimental results has been that the additional neutrons above stability may exist as a diffuse neutron cloud surrounding a more dense nuclear core. The diffuse structure of the neutron distribution extends the Interaction Radius of these species to larger radial distances from the nuclear centre of mass. Unfortunately, the contemporary theories could not derive or predict the existence of such extended nuclear dimensions.

This result represented a departure from the understanding of some of the basic elements of nuclear structure and has cast into doubt some of the underlying assumptions in theoretical nuclear physics – specifically, the first order radius equation and the constant density hypothesis. This can be demonstrated by the number of recent

publications designed to re-evaluate the nuclear potential and incorporate the observable quantities of the Neutron Halo phenomenon into their formalism [2][3][4][5].

1.2.2 Kobayashi Experiment

Further evidence of the neutron halo was uncovered in an experiment conducted by Kobayashi and his group at KEK [6]. In this study, a lead target was bombarded, in turn, by an ion beam of a so-called halo nuclide (^{11}Li) and by an ion beam of a stable isotope with similar mass (^{12}C). The quantity of interest was the transverse momentum of the nuclide fragment less two neutrons (^9Li , ^{10}C).

The theory behind the experiment was based on the uncertainty principle. If the outermost neutrons truly exist as a halo then the spatial distribution of the two halo neutrons must be larger than the corresponding neutrons in the stable counterpart. If the spatial distribution of the halo neutrons is larger than for the stable species then the corresponding momentum spread of the halo neutrons should be lower than for the stable species.

In terms of the uncertainty principle, if there is a large uncertainty in the *position* of the halo neutrons then there must be a small uncertainty in the *momenta* of those neutrons. By measuring the transverse momentum of the ^9Li and ^{10}C fragments, the validity of the neutron halo hypothesis could be tested.

The results of the experiment showed that the uncertainty in the transverse momentum of the halo fragment (^9Li) was lower than the uncertainty in the transverse momentum of the stable fragment (^{10}C) by about a factor of six. The dramatic difference between the range of the two fragments' transverse momenta indicates a significantly lower momentum uncertainty for the halo neutrons as compared with the stable species. From the low momentum uncertainty, a high spatial uncertainty may be inferred and the existence of the so-called neutron halo is confirmed indirectly.

1.3 Exotic Decay

The ${}^6\text{He}$ nuclide is a radioactive, heavy isotope of helium that decays with a characteristic beta decay half-life of (0.8067) seconds [8]. In this process a ${}^6\text{He}$ neutron is converted to a proton with the subsequent emission of an electron (beta) and a neutrino to maintain overall charge and spin conservation.



Prior to 1990 it was thought that the decay scheme of ${}^6\text{He}$ was a remarkably simple one. It was believed that the ${}^6\text{He}$ decay consisted of only one branch; that to the stable ground state of ${}^6\text{Li}$.



On the basis of this single branch interpretation, ${}^6\text{He}$ became a textbook example of a mono-energetic beta decay transition [24] [37].

In 1990, however, Riisager's group at CERN reported the first observation of an additional weak branch in the ${}^6\text{He}$ decay scheme [7]. They observed that for a small fraction of ${}^6\text{He}$ decays, the beta transition was followed by the emission of a deuteron rather than a direct decay to the ${}^6\text{Li}$ ground state. Figure 1.1 shows the two branches of the ${}^6\text{He}$ beta decay scheme with respect to the energy levels of the mass ($A = 6$) isobars [8] where the quoted energies are in MeV relative to the ${}^6\text{Li}$ ground state and the spins and parities of the various levels are included in the figure.

This beta delayed deuteron emission is completely unique to ${}^6\text{He}$. Of the over two thousand nuclides that have been produced and investigated, ${}^6\text{He}$ is the only known example of a beta delayed deuteron emitter.

1.3.1 Branching Ratio

When an isotope exhibits more than one branch (or exit channel) in its decay scheme it is useful to characterize the strength of each branch on a normalized scale. This is done by measuring the probability that any one given decay will proceed through a given exit channel. These probabilities are commonly referred to as Branching Ratios.

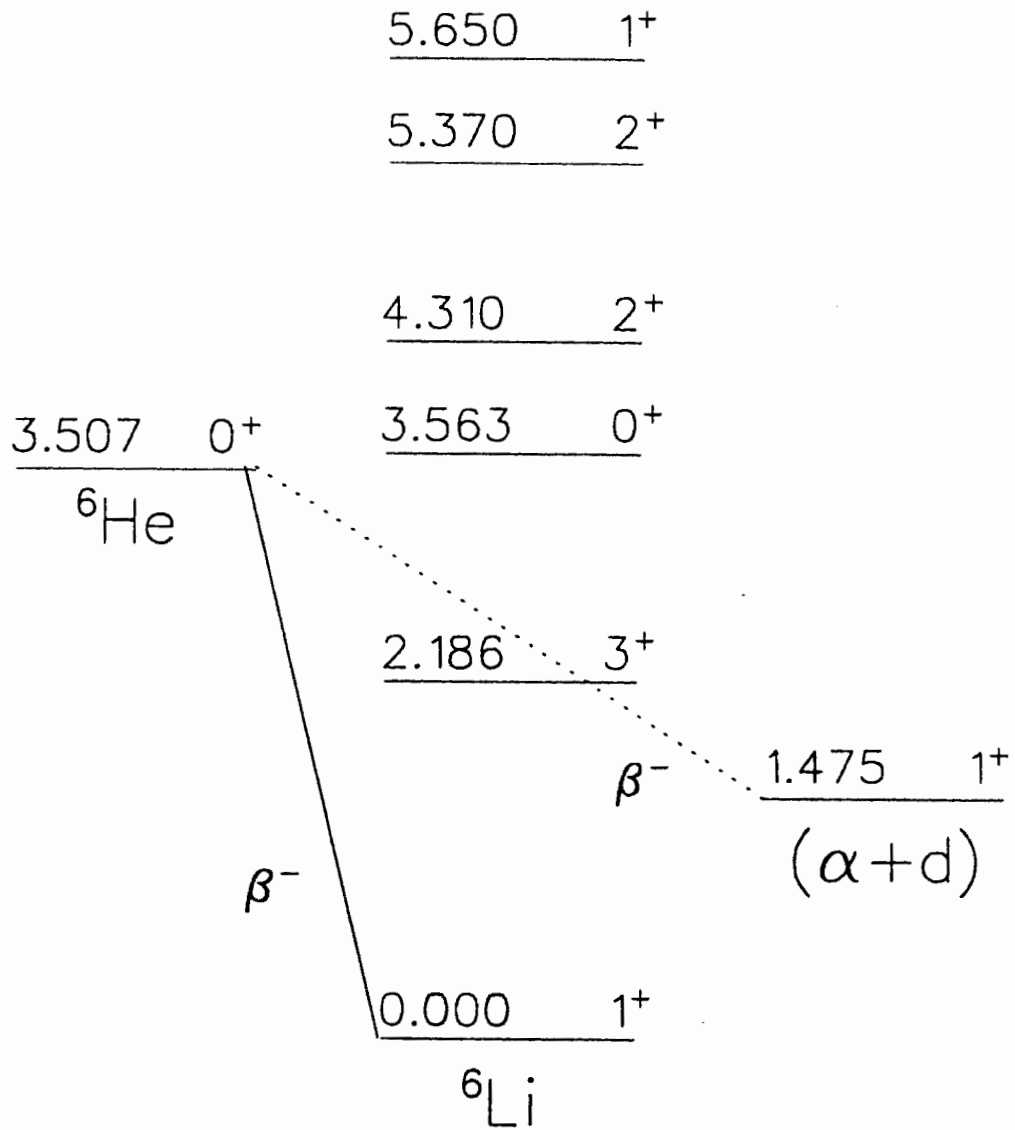


Figure 1.1: Energy levels of the mass ($A=6$) isobars

Since the first observation of the exotic deuteron emission, two experiments have been performed to characterize the $(\alpha + d)$ exit channel by determining the branching ratio of ${}^6\text{He}$ decaying to the unbound $(\alpha + d)$ state. The first, Riisager's original experiment, determined the probability of ${}^6\text{He}$ emitting a deuteron to be $(2.8 \pm 0.5) * 10^{-6}$ [7]. The second experiment, conducted by Borge's group in 1993, determined the branching ratio to be $(7.6 \pm 0.6) * 10^{-6}$ [9].

Clearly, the two experimental results for the branching ratio of ${}^6\text{He}$ proceeding through the $(\alpha + d)$ exit channel do not agree. The disagreement between the two published results indicates that one or both of these determinations are incorrect. In addition, a second quantity of interest, the energy spectrum of the emitted deuterons, has not been adequately measured. Although both Riisager and Borge included particle energy spectra in their papers, the number of events in these spectra are so few that their inferred shapes are suspect.

1.4 Synthesis

The existence of the ${}^6\text{He}$ neutron halo has spawned considerable activity on the part of nuclear theorists to develop new models of the ${}^6\text{He}$ structure that are consistent with the halo phenomenon. Two of the observable quantities that comprehensive theories will be able to predict are the ${}^6\text{He}$ branching ratio to the $(\alpha + d)$ state and the energy spectra of the emitted alphas and deuterons. Therefore, the suitability of a particular theoretical model may be tested against the experimentally determined quantities such as the branching ratio and the particle energy spectra.

1.4.1 Theoretical Models

Over the course of the past few years, a multitude of potential model calculations and many-body descriptions of the ${}^6\text{He}$ nuclide have been published. One of the earliest models viewed the ${}^6\text{He}$ structure as a two cluster system [10]. In this description, ${}^6\text{He}$ was assumed to exist as an alpha core and a dineutron. The dineutron cluster assumed that the two outermost neutrons were highly correlated, meaning that the

position of one neutron was dependent on the position of the second. From this model, a theoretical branching ratio for the $(\alpha + d)$ emission and a deuteron spectrum shape were extracted. It was found that the deuteron spectrum shape was not consistent with the spectra collected experimentally and that the theoretical branching ratio over-estimated the observed branching ratio by *orders of magnitude*.

In this original two cluster model the existence of the neutron halo is largely ignored. An alpha particle and dineutron model is more or less the default interpretation of the ${}^6\text{He}$ structure. The overestimation of the $(\alpha + d)$ break-up by this model is due to the fact that the more highly correlated the two neutrons are, the greater the likelihood that they will think they are a deuteron. In more academic terms, the more correlated the neutrons, the greater the overlap between the ${}^6\text{He}$ and $(\alpha + d)$ wave functions. Therefore, because the branching ratio is overestimated in this two cluster approach and because the model minimizes the halo, the discordant result has been taken as indirect evidence of the neutron halo's existence.

Later theoretical models have viewed the ${}^6\text{He}$ structure as being a three body system. In this framework, the ${}^6\text{He}$ structure is that of an alpha core surrounded by two, single neutrons. In simple terms, this model views the outermost neutrons as being, for the most part, uncorrelated. The effect of the uncorrelated neutron approach is to dramatically reduce the probability of $(\alpha + d)$ break-up.

The first of the three cluster models [11] was able to reproduce the beta decay probability of ${}^6\text{He}$ decaying to the ${}^6\text{Li}$ ground state with a high degree of accuracy. However, the reported deuteron branching ratio was about an order of magnitude too high. Furthermore, even with the high uncertainty in the published experimental deuteron spectrum, the shape of the theoretically derived spectrum is not the same as what has been observed.

The second of the three cluster models [13] underestimated the observed deuteron branching ratio by about a factor of two. However, the shape of the deuteron spectrum appears to agree with the experimentally collected spectrum. The low statistics of the experimental spectrum, though, make it difficult to draw any definite conclusions.

The third of the three cluster models [12] was able to reproduce the proton, neutron, and total matter distributions of Tanihata's experiment with fairly close agreement. However, once again, the shape of the theoretical spectrum appears to be very different from the experimental spectrum and, although the authors do not quote a branching ratio, it is clear from the spectrum that the theoretical value underestimates the Borge experimental value of $(7.6 \pm 0.6) * 10^{-6}$ [9] due to the fact that the magnitude of the theoretical form underestimates the experimental data at all energies.

The uncorrelated neutron models do uncover one item of great interest. They show that, even though the neutrons are treated independently, there still exist two configurations in which the neutrons experience a high degree of correlation. These occur when the two neutrons are adjacent, and when the two neutrons are on opposite sides of the nucleus. The authors suggest that the relative strength of these correlated configurations is a critical factor in the magnitude of the $(\alpha + d)$ branching ratio. In all of the three body models, the authors report that the magnitude of the branching ratio is extremely sensitive to the dimensions of the neutron halo.

1.5 Summary

The ${}^6\text{He}$ nuclide has shown anomalous behavior in two ways. It has exhibited a neutron halo structure and it has been observed to emit beta delayed deuterons. Theoretical analyses of the halo structure have indicated that observable quantities such as the $(\alpha + d)$ break-up probability and the shape of the emitted particles' energy spectra may be sensitive probes of the halo phenomenon.

The two previously published results for the $(\alpha + d)$ branching ratio not only disagree with each other but they also have not been reproduced within the theoretical models (See table 1.1). Furthermore, one author [13] notes that, when integrated, the experimental deuteron spectrum published by Borge *et al* does not agree with the reported branching ratio of the same reference.

With regard to the published deuteron energy spectra, there have been many attempts to fit the observed spectra with theoretical forms. The results have met

Table 1.1: Theoretical and Experimental ($\alpha + d$) break-up probabilities

METHOD	BRANCHING RATIO $E_d > 350\text{keV}$	REFERENCE
Experimental	$(2.8 \pm 0.5) * 10^{-6}$	[7]
Experimental	$(7.6 \pm 0.6) * 10^{-6}$	[9]
Theoretical	$2 * 10^{-4}$	[10]
Theoretical	$3.5 * 10^{-5}$	[12]
Theoretical	$3.1 * 10^{-6}$	[13]

with varying degrees of success. However, it has been suggested [32] that to truly test a theoretical model a deuteron spectrum with better statistics may be required.

In light of the conflicting experimental values of the ($\alpha + d$) branching ratio and the low number of counts in the published particle energy spectra, an experiment was performed at TRIUMF on the ${}^6\text{He}$ nuclide. The goals of this experiment were to re-measure the branching ratio for the decay of ${}^6\text{He}$ to the ($\alpha + d$) state, and to generate the energy spectra of the emitted alphas and deuterons with sufficient statistics that theoretical models of the anomalous ${}^6\text{He}$ structure may be accurately tested.

In this work, the main features of the TRIUMF experiment are outlined in chapter two. The data analysis and results for the determination of the particle energy spectra and ($\alpha + d$) branching ratio are in chapters three and four, respectively, while chapter five outlines an attempt to fit the particle energy spectra within the framework of K-matrix theory – the idea being to determine the total branching ratio of the ($\alpha + d$) break-up. In addition, chapter five compares some of the previously published theoretical spectra with the spectra generated in this work. Finally, a general summary of the experiment and its results is presented in chapter six.

Chapter 2

Experiment

2.1 Production

The only naturally occurring sources of the ${}^6\text{He}$ isotope are the hot, dense environments of stellar media. When this fact is taken together with the short ${}^6\text{He}$ half-life (806.7 milliseconds) it should not be surprising that there are no terrestrial samples of this nuclide upon which experiments may be performed. The investigation of this isotope's nuclear properties thus requires a physics laboratory capable of artificially producing ${}^6\text{He}$ in yields commensurate with the experimental goals.

One such laboratory is the TISOL facility (TRIUMF Isotope Separator On-Line) located at the TRIUMF meson factory in Vancouver, Canada. The TISOL facility, as its name suggests, uses an ISOL or Thick-Target method for the production of short-lived nuclides. The main features of the TISOL isotope production system are illustrated in figure 2.1. What follows is a brief description of each of the major components involved in the TISOL process. More detailed descriptions of these devices may be found elsewhere [14][15][16][17].

In the TISOL process, a beam of 500 MeV protons generated by the TRIUMF cyclotron is focused into the TISOL target chamber. The cylindrical target chamber has dimensions (2in x 19in) and is filled with a stable target compound, the composition of which is selected beforehand based on the mass region of the desired product.

When the energetic protons collide with the stationary target nuclei, spallation

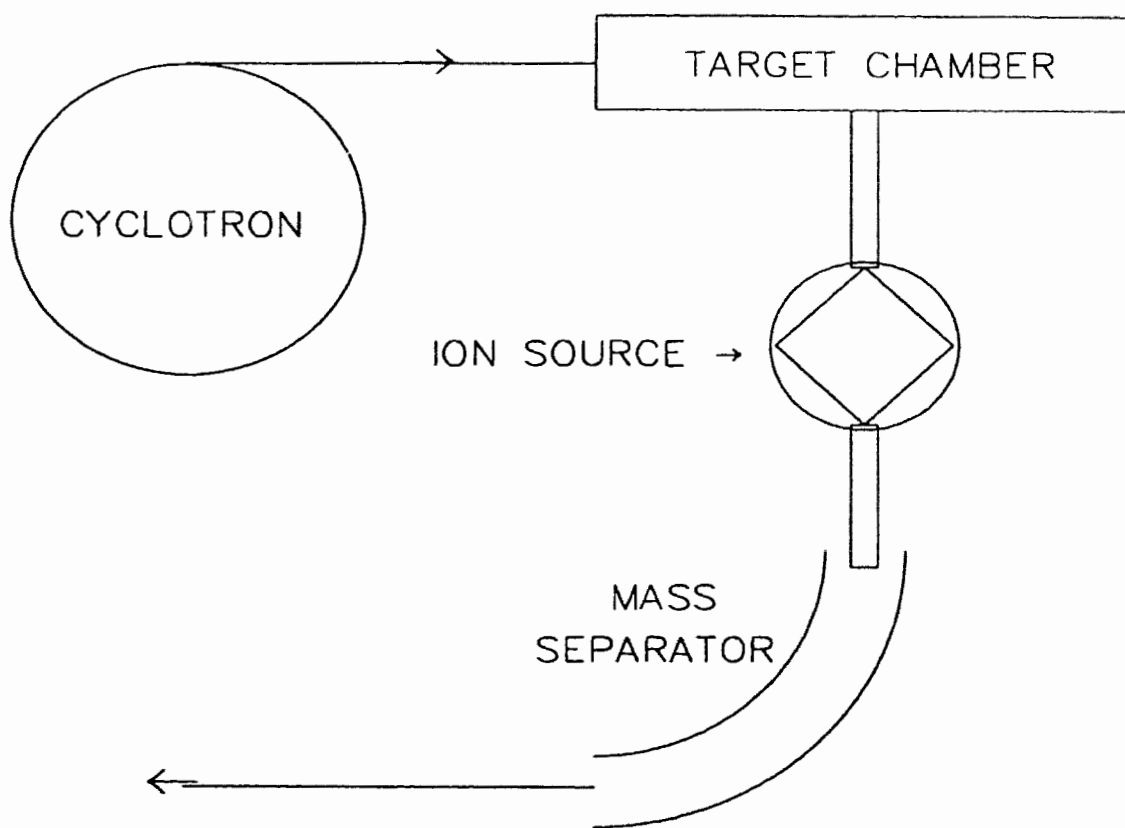


Figure 2.1: Main features of the TISOL isotope production system

and fragmentation processes are induced. The result of these nuclear reactions is the creation of various fragment isotopes, including a multitude of atomic and molecular species, with isotopic masses ranging from $A=1$ up to the combined mass of the projectile and target nuclei involved in the reaction. Typically, the target chamber is heated to about 2000 degrees Kelvin. In this high temperature environment, the created species diffuse out of the target chamber and into the TISOL Ion Source area via a transfer line.

For this particular experiment, an Electron-Cyclotron Resonance (ECR) source was utilized to ionize the products formed in the proton/target interaction. In this device, a small sample of inert gas, typically Argon or Krypton, is introduced to the ECR chamber. This gas is ionized by a radio-frequency pulse supplied by an RF generator. The energy of the pulse and the shape of the magnetic field applied to the ECR ionization chamber are designed to circulate the free electrons at their cyclotron resonance frequency. What develops is a gas plasma containing electrons and ions bound by the applied magnetic field. When an isotope created in the target chamber diffuses into this plasma, collisions between the energetic electrons and the reaction products cause the isotope to be converted to its ionic form.

Once in a charged atomic (or perhaps molecular) state, the species are withdrawn from the ion source by the application of an electric field to the system through an extraction electrode (EE). The extracted nuclei are then focused into a manageable beam and transported, using various electromagnetic devices, to the TISOL Mass Analyzing Magnet.

The mass analyzer is simply a large dipole magnet. When a charged species enters the dipole field of the magnet, its direction of propagation will be bent in a circular path with a radius of curvature defined as:

$$R = \frac{p}{qB} = \frac{m\nu}{qB} \quad (2.1)$$

where p , q , m , ν are the particles momentum, ionic charge, mass, and velocity, respectively, and B is the magnitude of the applied magnetic field. Knowing that all species, regardless of mass, are extracted at a constant potential V , the kinetic

energy of particle (i) is simply:

$$1/2m_i\nu_i^2 = q_iV \quad (2.2)$$

From this equation it can be shown that all species with the same mass-to-charge ratio (A/q) also have the same velocity ν . Substitution of this result back into equation 2.1 suggests, then, that all species with the same (A/q) value will be bent with the same radius of curvature in a constant magnetic field. Therefore, by adjusting the current in the dipole magnet, a radius of curvature may be selected for which only those species with the appropriate (A/q) will be transmitted through the dipole magnet. In this way, beam contaminants are removed from the product of interest at the mass analyzing stage of the TISOL radioactive beam production sequence.

From the mass analyzer, the resultant beam is directed and focused by electromagnetic elements and transported to a low background experimental area where physics and chemistry experiments can be performed.

For the ${}^6\text{He}$ experiment, development tests indicated that high yields of ${}^6\text{He}^+$ were obtainable with a variety of target materials including Zeolite, Thorium-Carbide, Uranium-Carbide, and Carbon graphite. However, it was also discovered (from the beta half-life spectra) that the heavier mass target materials (Zeolite, Thorium-Carbide, Uranium-Carbide) yielded ${}^{18}\text{Ne}^{3+}$ in appreciable quantities. The problem, then, is that ${}^{18}\text{Ne}^{3+}$ having the same (A/q) as ${}^6\text{He}^+$, was not separated from the ion beam by the mass analyzing magnet. Since ${}^{18}\text{Ne}^{3+}$ is radioactive (a beta emitter), large quantities of this isotope would seriously hamper the ${}^6\text{He}$ experiment. Consequently, the target utilized for the production of ${}^6\text{He}$ was the Carbon graphite material. This target did not produce ${}^{18}\text{Ne}^{3+}$ upon proton bombardment.

Experimental results have indicated that the yields of ${}^6\text{He}$ achieved at the Data Acquisition centre were on the order of 10^7 nuclei per second for every micro-amp of proton beam extracted from the cyclotron.

2.2 Detector End Station

The purified ${}^6\text{He}$ beam transmitted through the TISOL mass analyzer was directed to the Data Acquisition area housing the detector stations. The radioactive beam passed through an 8mm collimator and was deposited into thin carbon foils (thickness = $35 \mu\text{g}/\text{cm}^2$). The carbon implantation foils were mounted on aluminum cards which were themselves mounted on a rotating wheel. Three separate detector stations were located at successive 90 degree intervals from the ion implantation position. The wheel was designed to rotate a ${}^6\text{He}$ implanted foil from the collection position through to each detector station before being re-exposed to the ion beam. By mounting four foils with 90 degree relative spacing about the circumference of the wheel, at any given time one foil was being implanted with the ${}^6\text{He}$ activity while decay events from the other three foils were recorded at each of the three detector stations [18].

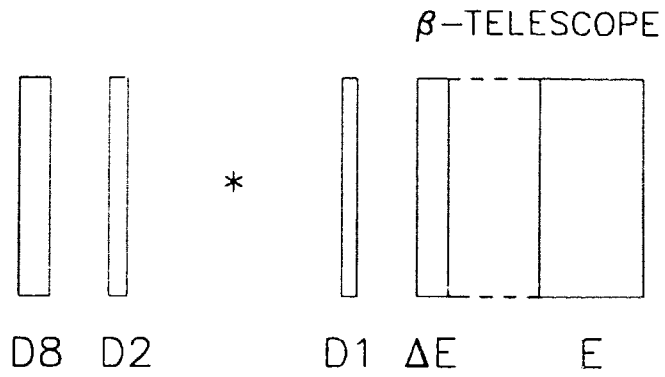
The movement of the wheel was controlled by a stepping motor. In general, the wheel holding time at the implantation/detection positions was set at about 1.1 seconds. The time interval for each 90 degree rotation was measured to be between 0.20 and 0.25 seconds.

At each of the detector stations, the ${}^6\text{He}$ sample was rotated into position between a pair of coaxial, opposite facing, charged particle detectors. These detectors were thin (10.6 to $30 \mu\text{m}$), surface barrier silicon detectors with their thicknesses chosen to preferentially detect alpha and deuteron particle events within the high beta field.

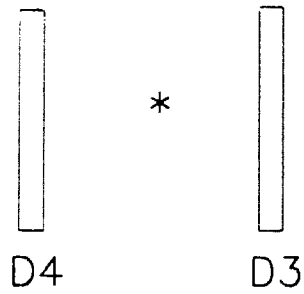
In addition to the particle (alpha and deuteron) detectors, the first detector station housed a Beta telescope detector and a second silicon detector to facilitate beta particle determinations. The beta telescope consisted of a thick ($500 \mu\text{m}$) surface barrier silicon detector and a 1mm thick Germanium crystal. The beta telescope was mounted directly behind one of the opposite facing particle detectors while the second beta counter, a $500 \mu\text{m}$ silicon surface barrier detector, was mounted immediately behind the other particle detector. Figure 2.2 shows a schematic diagram of the three detector stations used in this experiment. In addition, the figure shows the detector designations that will be used for the bulk of this thesis.

Due to the short half-life of ${}^6\text{He}$ (806.7 ms) with respect to the wheel hold/move

STATION (1)



STATION (2)



STATION (3)

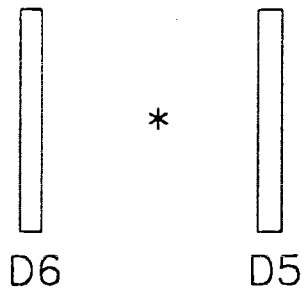


Figure 2.2: Detector Arrangement and Designations at the three counting stations

duration (1.3 seconds) the most useful data for both the particle energy spectra and the $(\alpha + d)$ branching ratio were recorded at the first detector station. Except where otherwise indicated, the analysis and discussion in this work refer to data acquired at detector station (1).

The entire detector array was encased within a sealed aluminum vacuum chamber. The vacuum levels at the detector end station were consistently better than 10^{-6} torr over the ${}^6\text{He}$ experimental runs.

2.3 Electronics

Signals produced in the particle detectors (D1 through D6) were preamplified and fed to the input ports of two main amplifiers. One amplifier shaped the input pulse for $3\mu\text{s}$ with the subsequent unipolar output pulse fed directly into one of the input slots of the Analog to Digital Converter (ADC). This process provided the energy signature of the charged particle event. The other main amplifier shaped the input pulse for $1\mu\text{s}$ with the bipolar output used as the timing signal for the event. The reference point of the timing signature was taken to be the zero-crossing point of the bipolar pulse.

Each bipolar timing output was fed into two discriminators set in parallel. The Upper Level Discriminator (ULD) threshold was set to pass events with energies in excess of about (250 keV) on an alpha energy scale. The Lower Level Discriminator (LLD) was set to pass events with energies in excess of approximately 50 keV on an alpha energy scale.

Signals in any particle detector (D1 to D6) passing through the LLD were fed into the Time to Digital Converter (TDC) with each detector having an individual 'START'. The ULD outputs for the six particle detectors were combined in a logical 'OR' to generate a master trigger for particle events. The master trigger output was subject to a wheel movement and computer busy 'VETO' with the idea of eliminating electronic noise due to the operation of the stepping motor, and to suppress electronic pile-up in the data acquisition computer. The master trigger opened the ADC gate and provided a common TDC stop after a 700 ns delay. The master trigger was

also fed into one input of the C212 CAMAC unit, providing a particle event LAM (Look-At-Me) that instructed the CAMAC to begin its data reading protocol.

Signals in the ΔE component of the beta telescope were preamplified and fed into the input slots of two main amplifiers. One amplifier shaped the pulse for $1\mu s$ and was fed into the ADC for an energy reference. The second amplifier shaped the pulse for $0.5\mu s$ with one of the outputs going to the TDC, while the second was fed into a beta coincidence unit.

Signals in the E component of the Beta telescope were preamplified and formed the input signal to one main amplifier. The amplifier shaped the signal for $0.5\mu s$ with the unipolar output going directly to the ADC. One of the amplifier's bipolar outputs was fed into the TDC while a second bipolar signal was combined with the bipolar output of the ΔE detector at the coincidence unit in a logical 'AND'. One logical output signal from the beta coincidence unit was subject to the wheel movement and computer busy 'VETO' and provided a common stop. The second logical output provided a beta event gate for the CAMAC through a second slot in the C212 unit.

A precision pulser signal was presented at the test input of each preamplifier over the course of the experiment. The pulser signal provided a pulser event gate to the CAMAC through a third slot in the C212 unit. The pulser generated signals at the rate of 10 Hz and proved to be a useful monitor of detector drift and gain changes over the experimental runs. Figure 2.3 shows a schematic diagram of the principal features of the data acquisition electronics. Events were processed via standard CAMAC protocol on an event-by-event basis and written to 8mm magnetic tape for subsequent analysis off-line.

2.4 Beam Purity

The purity of the ${}^6\text{He}$ ion beam was tested by monitoring the beta activity at the data acquisition area. This was performed with the collection/hold time of the wheel set at ten seconds to allow for long lived background contaminants to be observed. The number of events detected in the beta telescope was plotted as a function of time to enable a half-life determination. The observed spectrum was fit to a function of

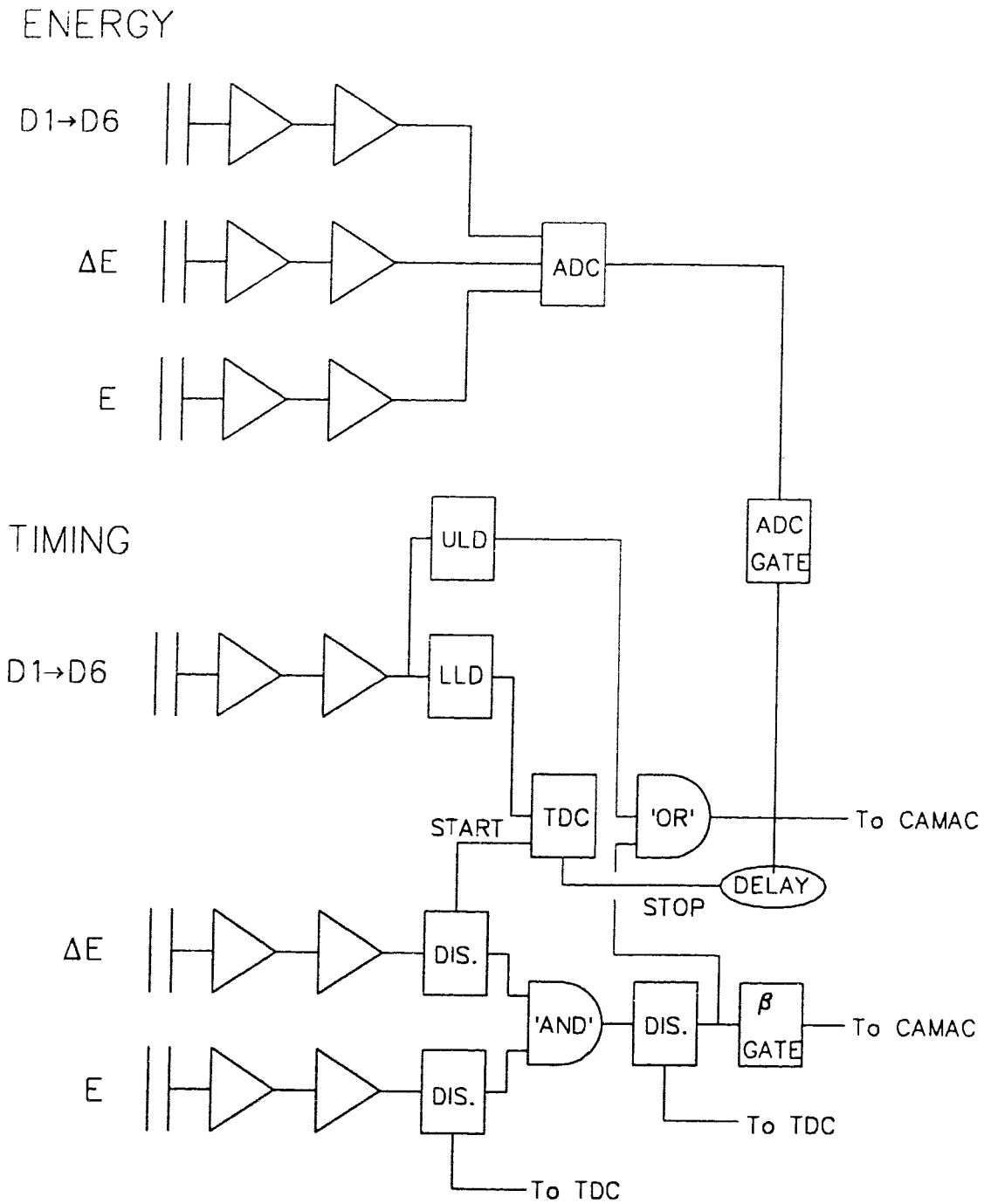


Figure 2.3: Electronics set-up for ${}^6\text{He}$ experiments

the form,

$$A = A^{\circ} * \exp(-\lambda * T) + C \quad (2.3)$$

where A° , λ , and C were allowed to vary freely.

The results of the fit in this beam purity run are shown in figure 2.4. The fitted half-life of the decay was found to be (0.810 ± 0.008) seconds; which is in excellent agreement with the literature value of (0.8067 ± 0.0015) [8] seconds for the half-life of ${}^6\text{He}$. From this beam purity run it was concluded that the ion beam extracted at a mass-to-charge ratio of ($A = 6$) from the graphite target was exclusively ${}^6\text{He}$ and very nearly background free.

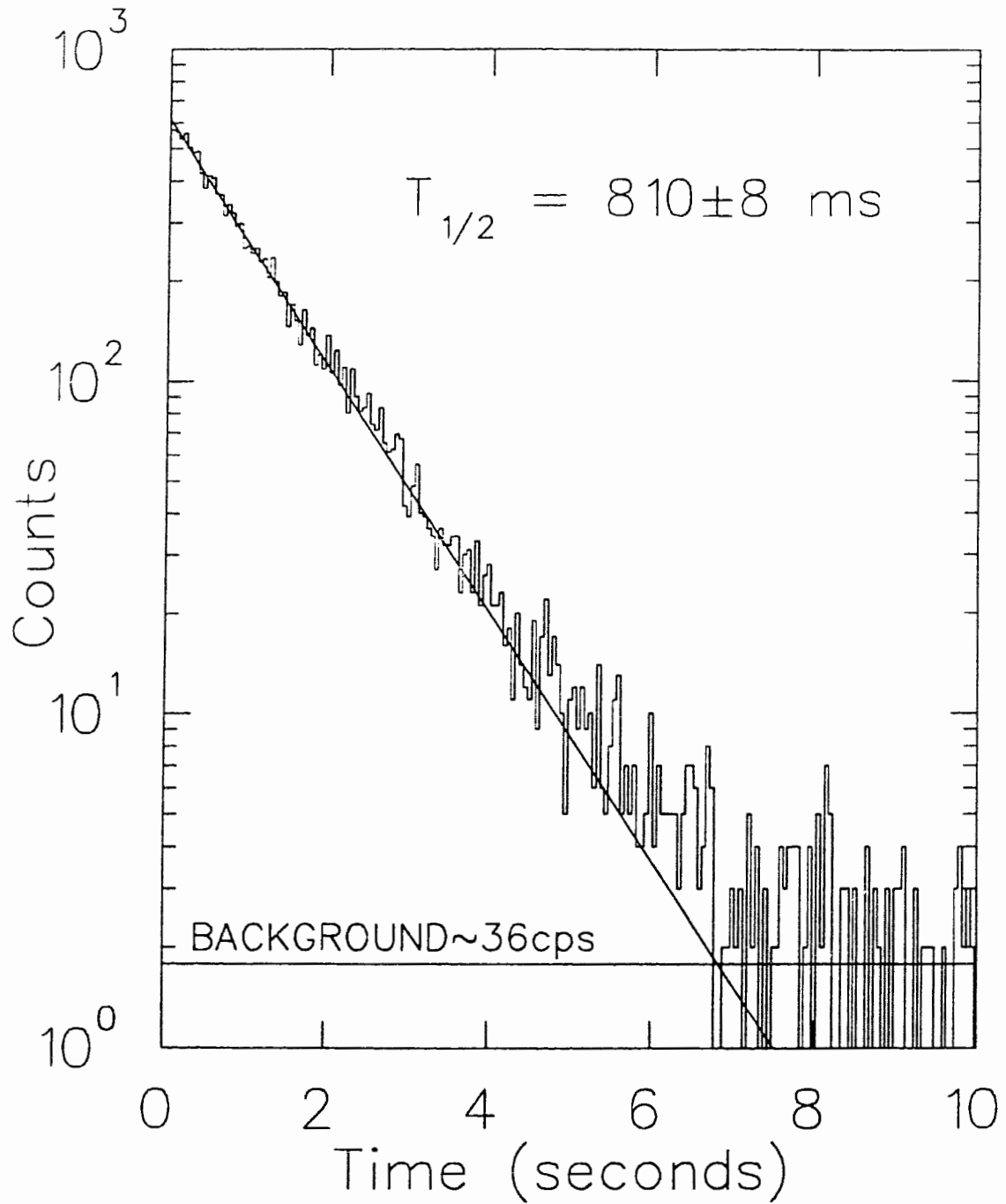


Figure 2.4: Beam Purity half-life test at mass-to-charge ratio ($A = 6$)

Chapter 3

Particle Energy Spectra

3.1 Energy Calibrations

The calibration of particle detectors D1 and D2 on an alpha particle energy scale was accomplished with the beta-delayed alpha lines of ^{18}N (1.081 and 1.409 MeV) [18] and the 3.182 MeV alpha decay line of ^{148}Gd . The ^{18}N source was produced at the TISOL facility from a zeolite target and monitored in the detector station under conditions identical to those of the ^6He runs. The ^{148}Gd source was a calibrated standard that was mounted onto an aluminium holder and periodically inserted into the detector array over the course of the experiment.

Before entering the depletion region of one of the particle detectors, D1 or D2, an alpha particle emitted by the ^{18}N source must pass through a portion of the Carbon implantation foil and through the Gold surface barrier layer of the detection device. Similarly, an alpha particle emitted by the ^{148}Gd source must pass through a portion of the finite Gadolinium source itself and through the Gold surface layer of the detection device. In each of these steps, the kinetic energy of the transmitted alpha particle will be degraded by an increment dependent on the thickness of the barrier and the atomic number of the material involved. Because of these energy degradations, an energy calibration curve can not be determined simply by plotting the literature energy of the alpha line versus the ADC response of the detector. The energies of the alpha lines must be corrected for losses incurred prior to detection in

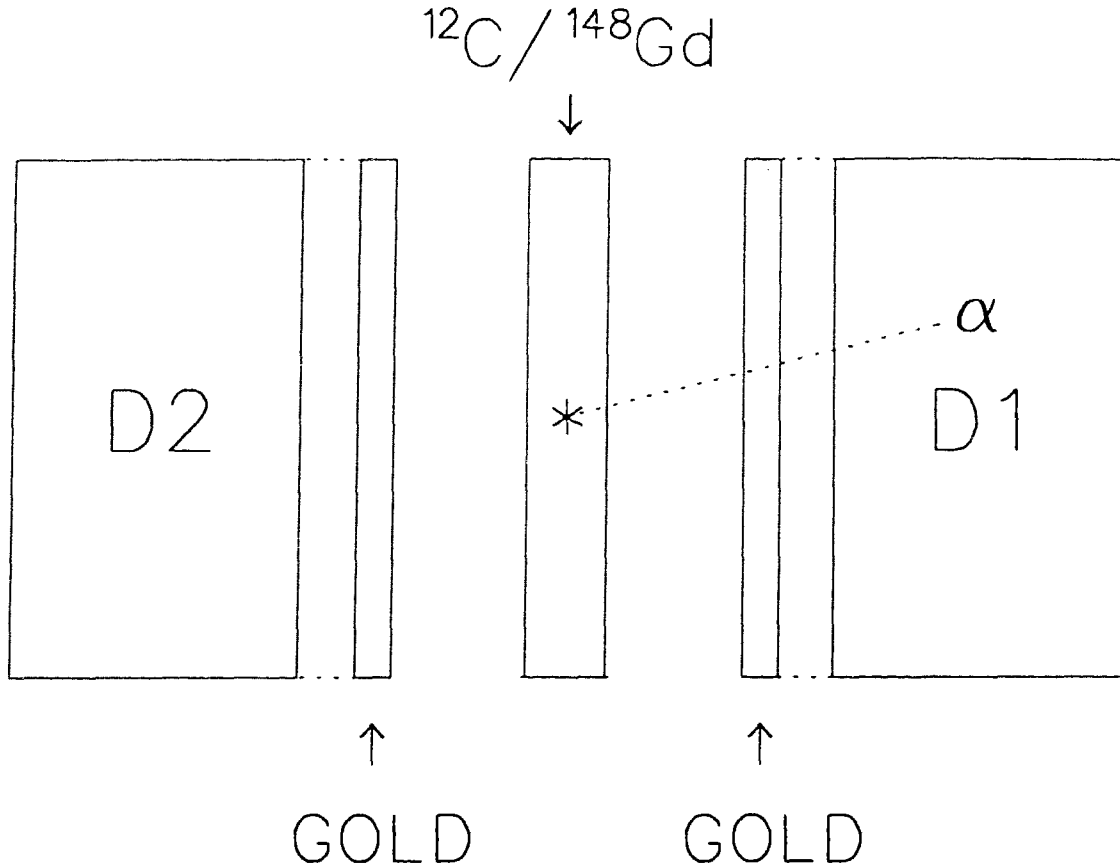


Figure 3.1: Alpha particle's path to detector depletion region

the depletion region of the particle detectors. Figure 3.1 shows a schematic diagram of a particle's path to the depletion region of detector D1. To correct for the alpha particle energy losses, the monte carlo program, TRIM [23], was used to calculate the implantation depth of ^{18}N nuclei into the Carbon collection foil. The result of the calculation indicates that the mean depth of implantation for 12 keV ^{18}N nuclei into a $10\mu\text{g}/\text{cm}^2$ carbon foil is $3\mu\text{g}/\text{cm}^2$. Therefore, knowing the Carbon foil thickness and the implantation depth it can be shown that an alpha particle emitted in the decay of ^{18}N must pass through $3\mu\text{g}/\text{cm}^2$ of Carbon prior to detection in D1, and $7\mu\text{g}/\text{cm}^2$ of Carbon prior to detection in D2. The same program has suggested that, due to straggling, the implantation depth is uncertain by about 30%.

The thickness of the Gold surface barrier layer, for both D1 and D2, is reported in the manufacturers' specifications as being $40\mu\text{g}/\text{cm}^2$. Therefore, in order to

Table 3.1: Corrected energy of calibration sources due to losses incurred in Carbon, Gold and Gadolinium

SOURCE	Literature Energy (keV)	Calibration Energy(D1) (keV)	Calibration Energy(D2) (keV)
$^{18}\text{N } \alpha_1$	1083.4 ± 1.3	1060.7 ± 6	1053.6 ± 6
$^{18}\text{N } \alpha_2$	1408.7 ± 0.4	1388.7 ± 6	1382 ± 6
^{148}Gd	3183 ± 1	3167.3 ± 2	3167.3 ± 2

construct a calibration curve, the energy of the ^{18}N alpha lines must be corrected for energy losses in $3\mu\text{g}/\text{cm}^2$ of Carbon plus $40\mu\text{g}/\text{cm}^2$ of Gold for detector D1 and $7\mu\text{g}/\text{cm}^2$ of Carbon and $40\mu\text{g}/\text{cm}^2$ of Gold for detector D2.

Again, the TRIM program was used to calculate the energy losses incurred by an alpha particle passing through (the appropriate thicknesses) of Carbon and Gold as a function of alpha particle energy. Figure 3.2 shows the results of this monte carlo calculation for detector D2 with the barrier thicknesses included in the figure. Here, it should be noted that the energy loss calculations for the emitted alpha particles have not been adjusted for possible effects due to the system geometry and crystal 'channeling'.

From these curves, the total energy losses at the two ^{18}N alpha particle energies were extracted. The energy of the alpha particle when it enters the depletion region of the detector can thus be determined by subtracting the calculated energy loss value from the published value of the alpha energy lines. This new value became the Calibration Energy of the alpha particle for the detectors' energy response.

A procedure completely analogous with the above description was conducted for the ^{148}Gd alpha line. In this case, though, energy losses in Carbon were replaced by energy losses in Gadolinium.

The results of the calibration energy corrections for both D1 and D2 as well as the final Alpha Calibration Energies are listed in Table 3.1. The uncertainties in the corrected Calibration Energy values are largely due to uncertainties in the Carbon foil thickness, beam implantation depth and Gadolinium source thickness.

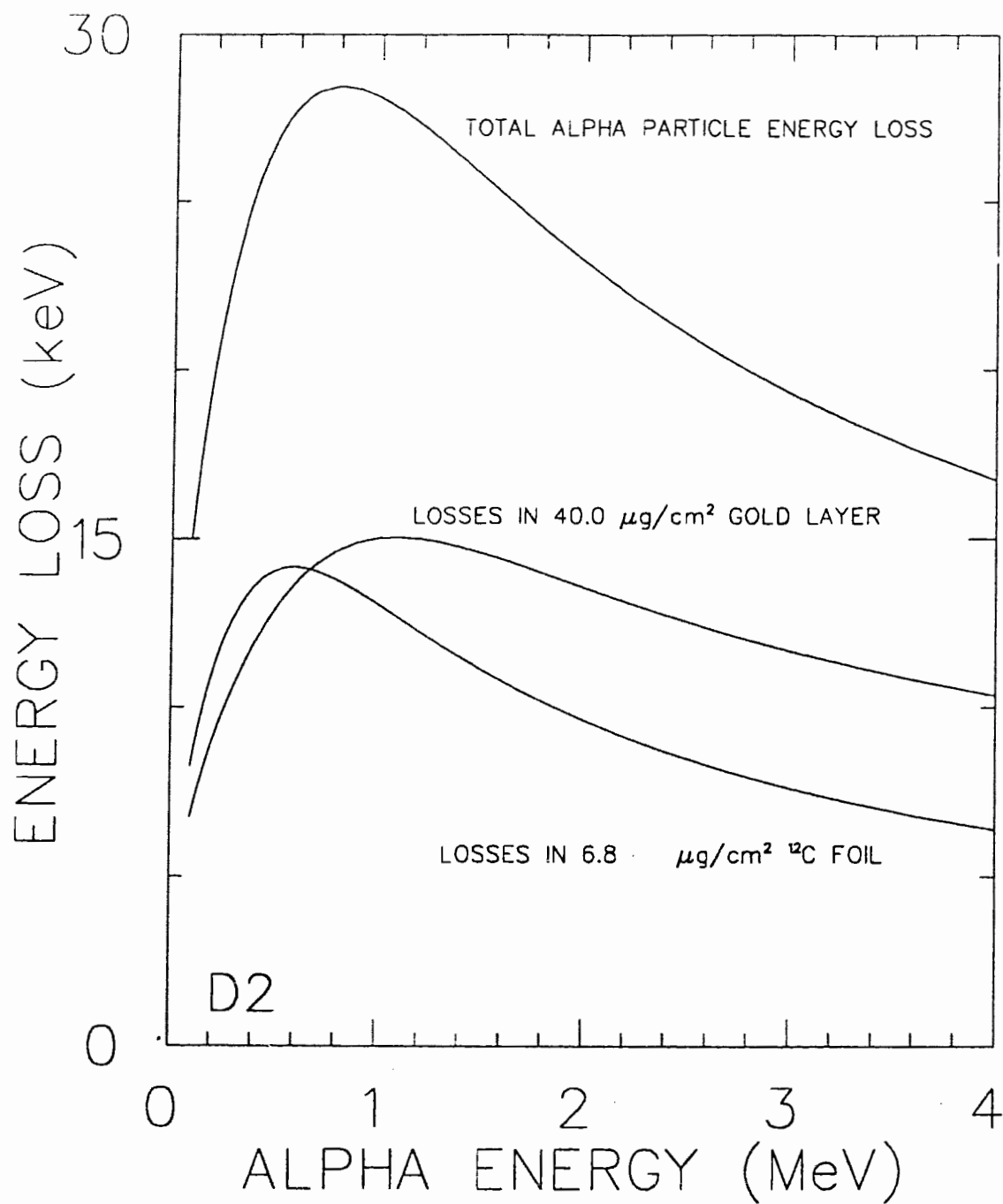


Figure 3.2: Alpha particle energy losses to detector D2 as a function of energy for ^{18}N emissions

Table 3.2: ADC channel response to the calibration sources in D1 and D2

SOURCE	D1 ADC Centroid	FWHM	D2 ADC Centroid	FWHM
$^{18}\text{N } \alpha_1$	526.0 ± 0.7	25 ± 2	477.2 ± 0.6	22 ± 1.2
$^{18}\text{N } \alpha_2$	698 ± 2	30 ± 5	627 ± 1.2	24 ± 3
^{148}Gd	1590.4 ± 0.2	16.8 ± 0.5	1443.2 ± 0.1	14.7 ± 0.2

Table 3.3: Calibration points for particle detectors D1 and D2

D1 Energy (keV)	D1 Channel	D2 Energy (keV)	D2 Channel
1060.7 ± 6	526.0 ± 0.7	1053.6 ± 6	477.2 ± 0.6
1388.7 ± 6	698 ± 2	1382.4 ± 6	627 ± 1.2
3167.3 ± 2	1590.4 ± 0.2	3167.3 ± 2	1443.2 ± 0.1

The actual ^{18}N alpha peaks recorded in D1 and D2 were fit to a gaussian shape with the centroid ADC channel and Full Width at Half Maximum (FWHM) being output parameters from the fit. An identical procedure was followed for the ^{148}Gd peaks and from these fits the ADC channel corresponding to the specific calibration energy of each source was extracted. Table 3.2 lists the alpha peaks and ADC response information gathered in both detectors.

From the experimentally determined ADC detector response to the alpha emissions and the corrected final Calibration Energies, energy calibrations of the detectors' Depletion Regions were derived. Table 3.3 lists the corrected final Calibration Energies and corresponding ADC response channel for each of the peaks in both detectors D1 and D2. Assuming that the pulse height recorded in the depletion region is a linear function of particle energy, the calibrations for the depletion regions of D1 and D2 were calculated. As an example, the calibration curve for detector D2 is shown in figure 3.3 while the results of the linear fits for D1 and D2 are listed in table 3.4. With these calibrations of the ADC response, particles detected in the depletion region of D1 and D2 may be converted to detected energy from the appropriate calibration

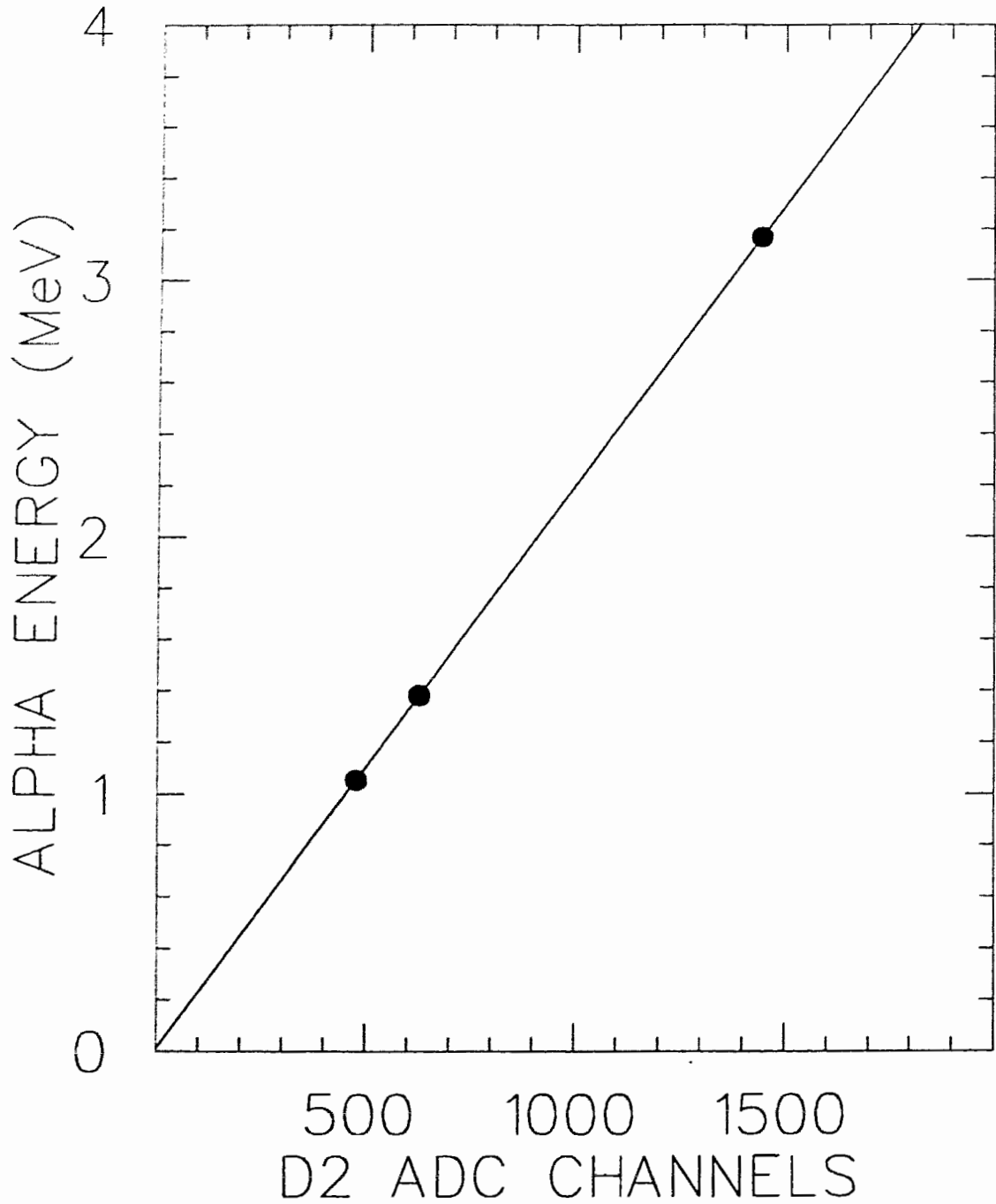


Figure 3.3: Calibration of D2 depletion region based on corrected source energies and D2 ADC response information

Table 3.4: Summary of depletion region calibrations based on an assumed linear response

Detector	Slope (keV/ch)	Offset (keV)
D1	1.985 ± 0.007	10 ± 11
D2	2.188 ± 0.005	10 ± 10

conversion.

3.2 Gadolinium Break Through

The thickness of detector D1 was insufficient to completely stop the alpha particles emitted in the decay of ^{148}Gd . This fact is demonstrated by the obvious break through in figure 3.4. The gaussian fit to this peak included only those points in the ^{148}Gd spectrum close to the the observed maximum. It was not clear that this peak, and hence this calibration point, could be rejected on the basis of the break through.

If the break through shifted the peak maximum, a correspondingly large peak width would be expected for the fit. It was found that the ratio of the ^{148}Gd peak width to the ^{18}N peak widths were identical for D1 and D2. It was therefore concluded that the ^{148}Gd peak width was not broadened due to the break through and that the ^{148}Gd calibration point for D1 was, in fact, reliable.

3.3 ^6He Particle Energy Correction

As was the case with the ^{18}N alpha lines, the alphas and deuterons emitted in the decay of ^6He must pass through the Carbon foil and Gold surface barrier layers prior to detection in the depletion regions. Therefore, the energy of the event detected in the depletion region must be augmented for particle energy losses incurred in the Carbon and Gold.

The monte carlo program, TRIM, was used to calculate the mean ^6He implantation

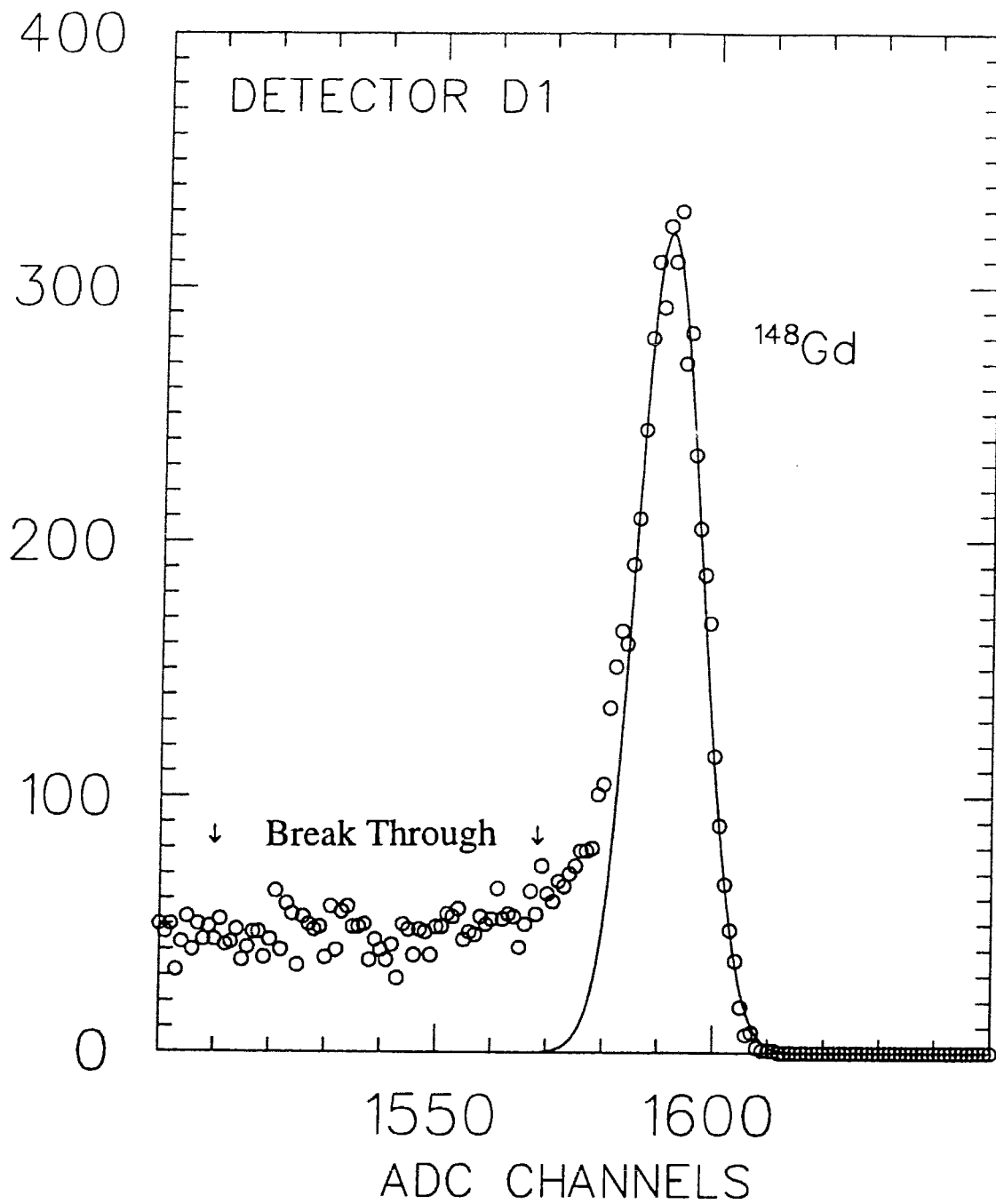


Figure 3.4: ADC response of detector D1 to 3.183 MeV alpha emitted in the decay of ^{148}Gd

depth into a $35 \mu\text{g}/\text{cm}^2$ Carbon foil with the beam energy set at a constant 12 keV. The result of the calculation indicates that the depth of implantation was $24 \mu\text{g}/\text{cm}^2$ – meaning that particles detected in D1 passed through $24 \mu\text{g}/\text{cm}^2$ of Carbon while particles detected in D2 passed through $11 \mu\text{g}/\text{cm}^2$ of Carbon. In both cases the same particles also pass through the $40 \mu\text{g}/\text{cm}^2$ Gold surface barrier layer before entering the depletion region.

Once again, TRIM was used to construct energy loss curves for each of the particle types (alpha and deuteron) as a function of emission energy. As an example, figure 3.5 shows the energy loss curves determined by this method for alpha particles *en route* to detector D2.

The alpha and deuteron spectra span a large energy range, therefore corrections for particle energy losses must be applied over the entire spectrum rather than at discrete points as was the case for the ^{18}N and ^{148}Gd corrections. To do so, the total energy loss curve (Eloss in Carbon + Eloss in Gold) was fit to an energy dependent function. It turned out that the best way to accomplish this was to fit the low energy part of the energy loss curve to a polynomial in energy, and to fit the high energy part of the total energy loss curve to a function linear in energy. As an example, the functional fit to the total energy loss curve for alpha particles on route to D2 is shown in figure 3.6 with the functional form of the best fits shown in both the low and high energy regions.

The energy correction procedure was to compare the detected energy of the particle, in this case an alpha in D2, with the setpoint energy value (the point at which the low and high energy fitted functions cross). If the detected energy was larger than the setpoint, the linear correction was used and if the detected energy was below the setpoint, the polynomial correction function was employed. For each detector and both particle types the polynomial correction was of the form:

$$E_{corr} = A * (E_{det} - B)^N + C \quad (3.1)$$

Where A , B and C were allowed to vary freely in the fit and N was the order of the polynomial that best approximated the low energy portion of the curve. The high

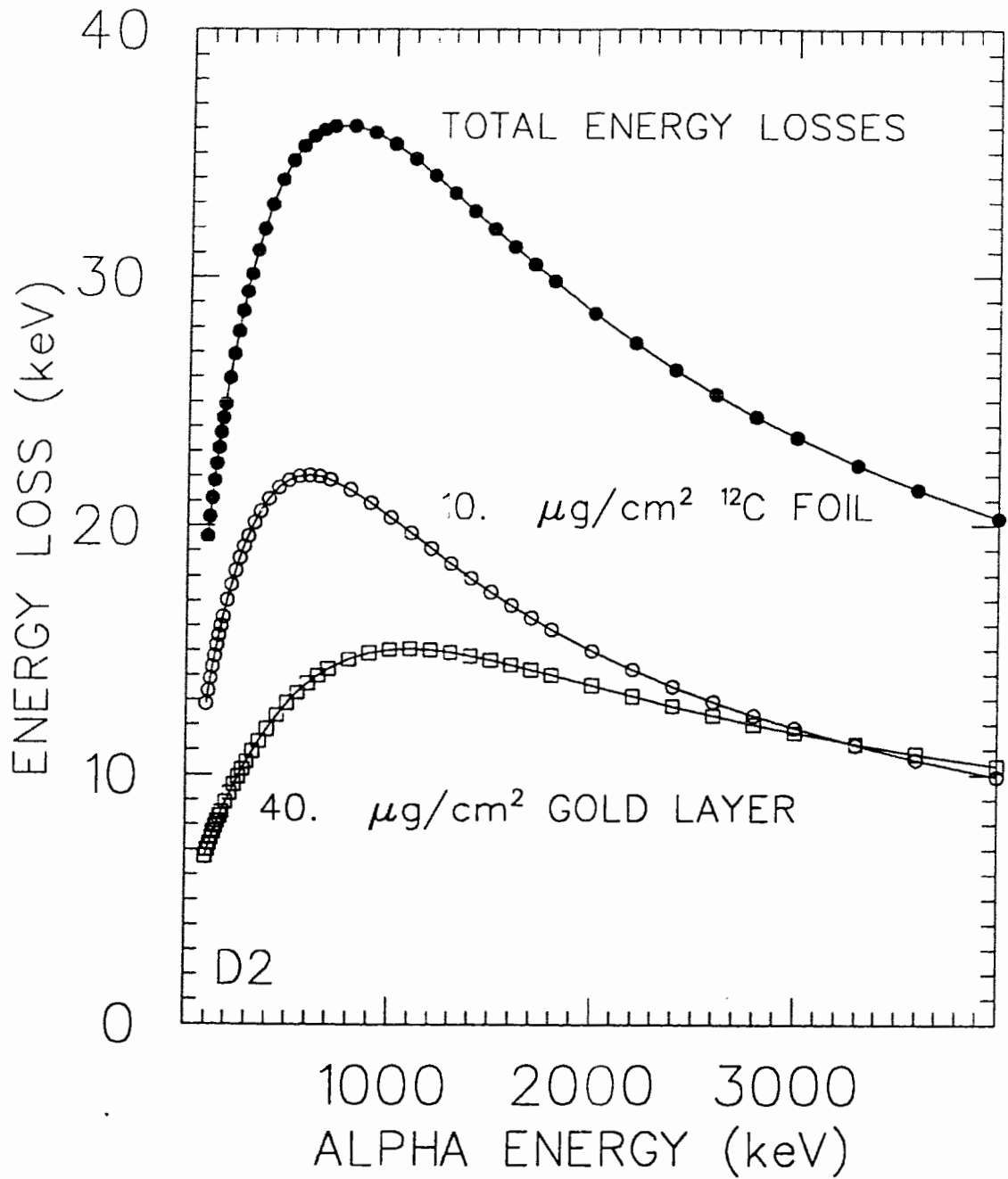


Figure 3.5: ^6He alpha particle energy losses in the Carbon foil and Gold layer prior to detection in the calibrated depletion region

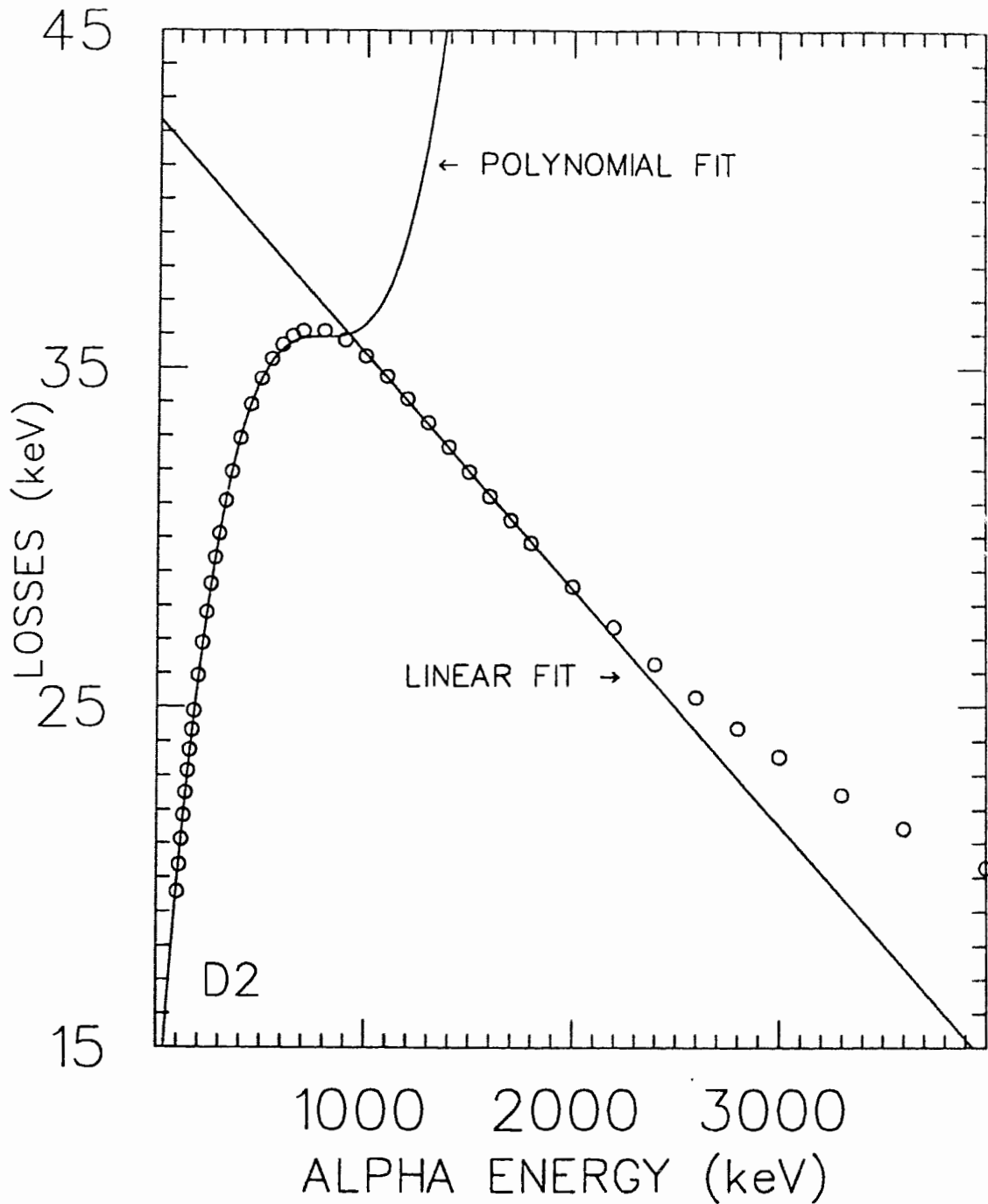


Figure 3.6: High energy polynomial and low energy linear fit to D2 alpha particle, energy correction curve

Table 3.5: Parameter values for the particle energy correction curves of D1 and D2

SPECTRUM	Polynomial			
	A	B	C	N
D1 Alphas	$(1.1 \pm 0.2) * 10^{-7}$	720 ± 30	63.6 ± 0.4	3
D1 Deuterons	$(-1.3 \pm 0.6) * 10^{-4}$	220 ± 20	21.9 ± 0.4	2
D2 Alphas	$(4.7 \pm 1.2) * 10^{-8}$	800 ± 60	35.9 ± 0.4	3
D2 Deuterons	$(-7 \pm 6) * 10^{-5}$	230 ± 30	12.1 ± 0.4	2

Table 3.6: Parameter values for particle energy corrections in D1 and D2

SPECTRUM	Linear	
	M	b
D1 Alphas	$(-1.4 \pm 0.1) * 10^{-2}$	74 ± 1
D1 Deuterons	$(-9.3 \pm 0.7) * 10^{-3}$	22.3 ± 0.6
D2 Alphas	$(-7 \pm 1) * 10^{-3}$	42 ± 2
D2 Deuterons	$(-4.9 \pm 0.7) * 10^{-3}$	12.6 ± 0.6

energy correction was of the form:

$$E_{corr} = M * E_{det} + b \quad (3.2)$$

where the slope and offset variables, (M, b) were allowed to vary freely.

The results of these fits for alphas and deuterons in detectors D1 and D2 are summarized in tables 3.5 and 3.6.

From the detected energy in the depletion region and the ${}^6\text{He}$ particle energy correction increments it was possible to convert the ADC response of a detector into an energy value corresponding to the particle's energy of emission in the ${}^6\text{He}$ decay. This enabled experimental determinations of the particle energy spectra from the $(\alpha + d)$ break-up of the ${}^6\text{He}$ nuclide – with the assumption that the energy calibration is the same for particle types.

3.4 Detector Resolution

The electronic resolution of the particle detectors was first estimated from the response of D1 and D2 to signals presented by the precision pulser. The observed pulser peaks were fit to a gaussian shape with the Full Width at Half Maximum (FWHM) extracted from the fit. As an example, figure 3.7 shows one of the pulser peaks collected in D1 parameterized by this method. The FWHM values were taken as being equivalent to the detector resolution. Converting the FWHM from ADC channels to energy, the resolution of detectors D1 and D2 were found to be 21 keV and 26 keV, respectively.

A similar resolution analysis was conducted on the detectors' response to a true alpha source ^{148}Gd . This analysis indicated that the resolution of detector D1 was 30 keV while the resolution of detector D2 was 32keV. Because the ^{148}Gd source more closely approximates the ^6He source than does the pulser, the quoted energy resolution for detectors D1 and D2 are 30 keV and 32 keV respectively.

3.5 Particle Identification

The two known branches of the ^6He decay scheme are shown on figure 3.8. The dominant branch is where the ^6He nuclide converts a neutron to a proton by the emission of a beta particle and neutrino to form the ^6Li ground state. The weak branch occurs when, after the conversion of a neutron to a proton, the resultant nucleus (containing three neutrons and three protons) further decays by the emission of a deuteron to form the unbound ($\alpha + d$) state. One of the goals of this experiment was to detect those transitions to the ($\alpha + d$) state and to generate the energy spectra of the alphas and deuterons emitted. To do so it was critical to be able to detect alpha and deuteron events and extract them from the field of the betas. This was accomplished by selecting particle detectors D1 and D2 to be thick enough to stop the alphas and deuterons but sufficiently thin that the detectors collect little or no energy from transmitted beta particles.

Figure 3.9 shows, as an example, the spectrum collected in D2 when it was exposed to a pure beta source ^{90}Sr which has an endpoint energy similar to that of ^6He . The

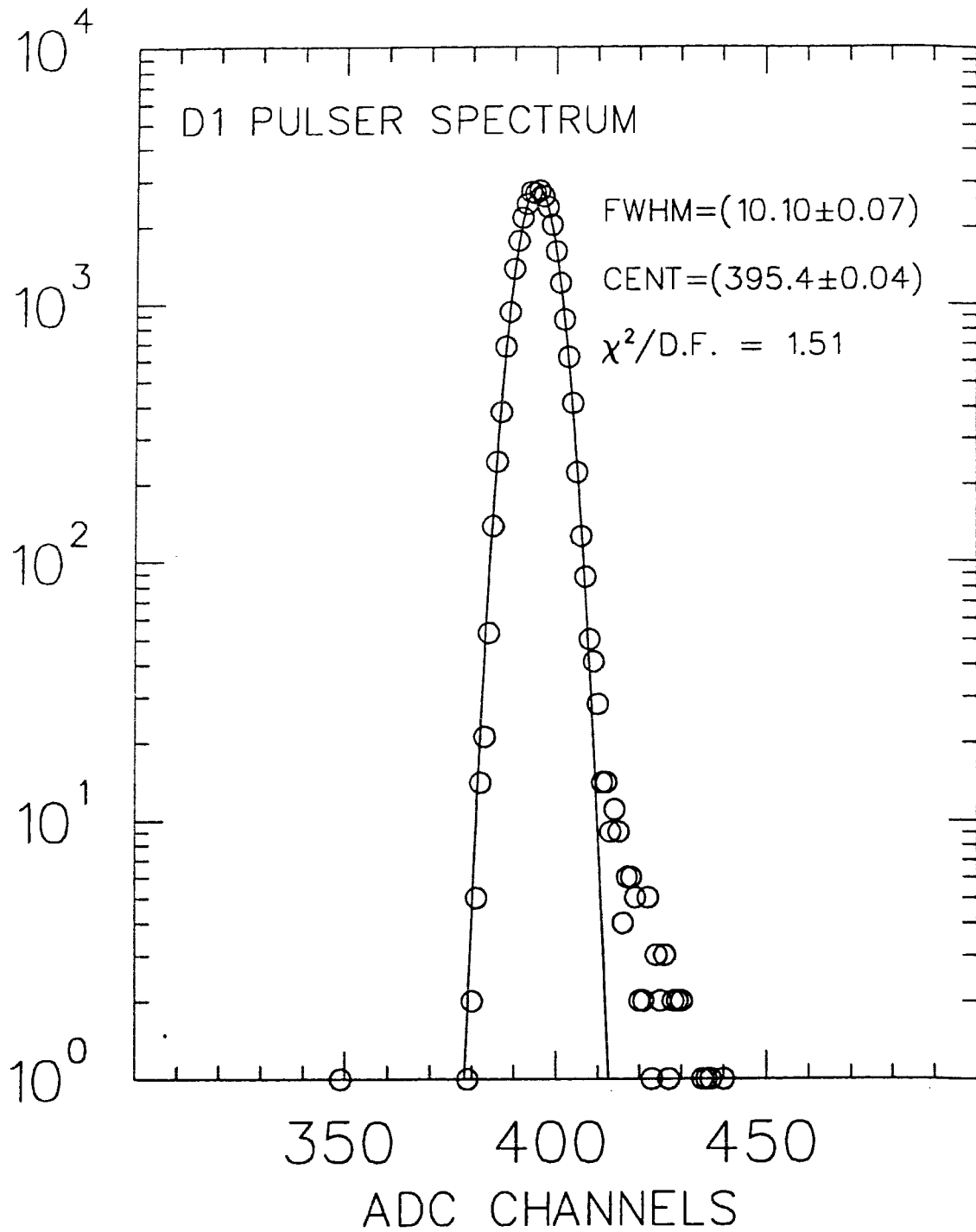


Figure 3.7: Detector D1 response to precision pulser signals

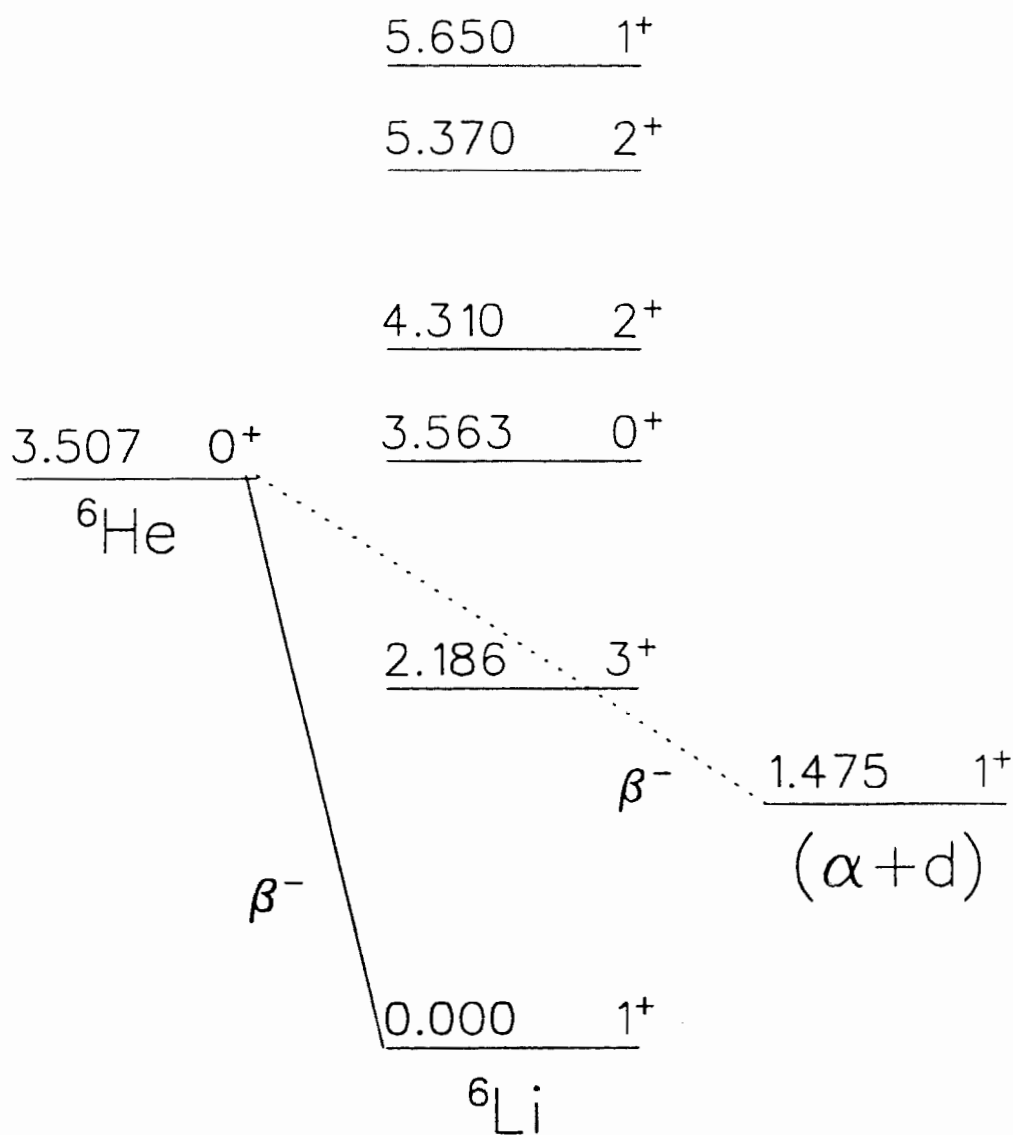


Figure 3.8: Two known branches of the ${}^6\text{He}$ decay

salient feature of this spectrum is that the highest energy response of the detector to the beta field is at an ADC channel of 130 which is a converted deuteron energy of about 290 keV in the laboratory frame. Hence, it is with considerable reliability that events above this beta response limit detected during the decay of ${}^6\text{He}$ were due to alpha or deuteron events rather than transmitted betas.

The second experimental requirement to produce alpha and deuteron energy spectra is the ability to distinguish between alpha particle events and deuteron particle events. Previous experiments [7] [9] have shown that, due to the process through which the break-up occurs, the energy spectra of the emitted alphas and deuterons are broad and overlapping. As an unfortunate consequence of this energy spectrum overlap, it is impossible to distinguish between an alpha and deuteron event based on the response signals of one, lone. particle detector. For example, if an event in D1 was registered at an energy of 500 keV, and if the alpha and deuteron energy spectra were to overlap in this energy region, it would not be clear whether this event was due to a 500 keV alpha or a 500 keV deuteron.

Fortunately, the law of conservation of momentum can be used to facilitate particle identification for this ${}^6\text{He}$ species. Since the ${}^6\text{He}$ nucleus is stopped within the Carbon foil when it decays, the law of conservation of momentum dictates that the product alpha and deuteron must be emitted with momenta equal in magnitude and opposite in direction (neglecting beta/neutrino recoil effects). For the momenta to be equal in magnitude it can be shown that the magnitude of the deuteron's kinetic energy must be twice the magnitude of the alpha's kinetic energy for any ($\alpha + d$) pair. In simplest terms, when the ${}^6\text{He}$ nucleus breaks up, the alpha and deuteron are emitted back-to-back and the ratio of the deuteron kinetic energy to the alpha kinetic energy is two to one.

Knowing these decay characteristics, the particle detector/ ${}^6\text{He}$ source geometry was designed such that the ${}^6\text{He}$ activity was stationed immediately between the particle detectors D1 and D2. By so doing, it was possible to set a coincidence requirement between the two particle detectors to take advantage of the back-to-back nature of the decay. With this geometry, an event in D1 was considered a real ${}^6\text{He} \rightarrow (\alpha + d)$ event if and only if a coincident event was recorded in detector D2. Furthermore, a D1

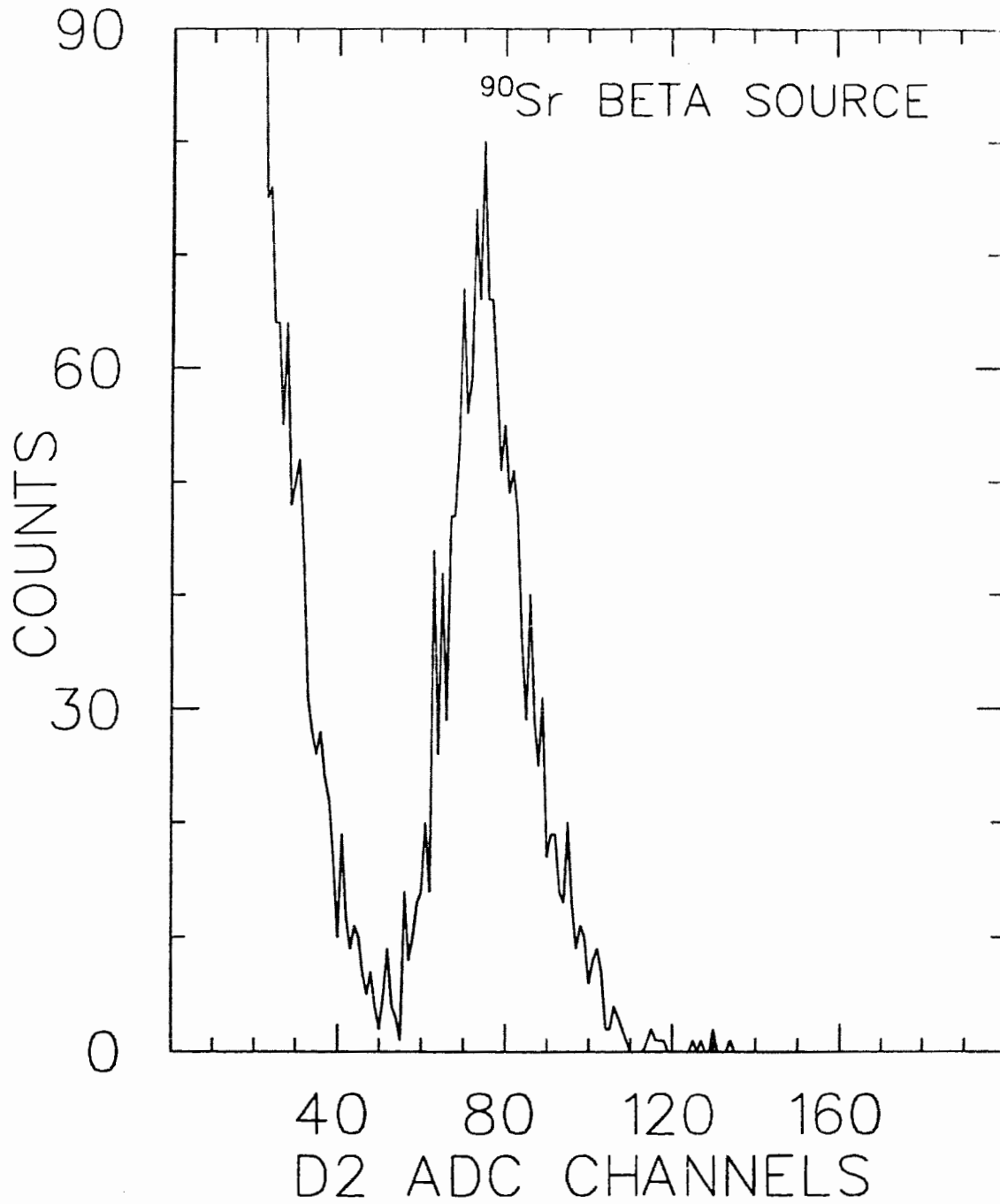


Figure 3.9: Particle detector response to transmitted betas

event was labelled as a *deuteron* event if and only if there was a coincident event in D2 and the energy of the D1 event was approximately twice the energy of the coincident D2 event.

Therefore, even though the absolute energy of either the alpha or deuteron can not be predicted for any one given decay, the law of conservation of momentum, coupled with an appropriate source/detector geometry, facilitates conclusive separation of alpha and deuteron particle events.

3.6 Particle Identification (Experimental)

In this experiment the data acquisition system recorded the timing and energy information for particle events on an event-by-event basis. From the timing information a coincidence window was set to extract alpha and deuteron events from the high beta field. Figure 3.10 shows a two-dimensional spectrum of the coincidence data recorded by the (D1, D2) particle detector pair.

The important feature of this graph is the existence of two, prominent diagonal bands within the plot. The interpretation of these bands is as follows: the band with the larger slope corresponds to D2 deuterons detected in coincidence with D1 alphas; while the band with the lesser slope corresponds to deuterons detected in D1 coincident with alphas detected in D2.

Figure 3.11 shows a slightly different representation of the coincidence data from in figure 3.10. In this plot, the y-axis is the D2/D1 ADC pulse height ratio – which is roughly equivalent to the ratio of the D2 event energy to the D1 event energy. This spectrum is limited to display only those events for which the D2/D1 pulse height ratio is in excess of (1.2). This effectively limits the displayed data to deuteron events in D2 in coincidence with alphas in D1 (or the higher slope band shown in figure 3.10).

Pulse height ratio cuts were made with reference to this figure with the idea of isolating true ($\alpha + d$) events and filtering out contributions made by coincidences involving beta particles and noise. Typically, the low end ratio cut was set at a pulse height ratio of about (1.5) and the high end ratio cut was set at a pulse height ratio

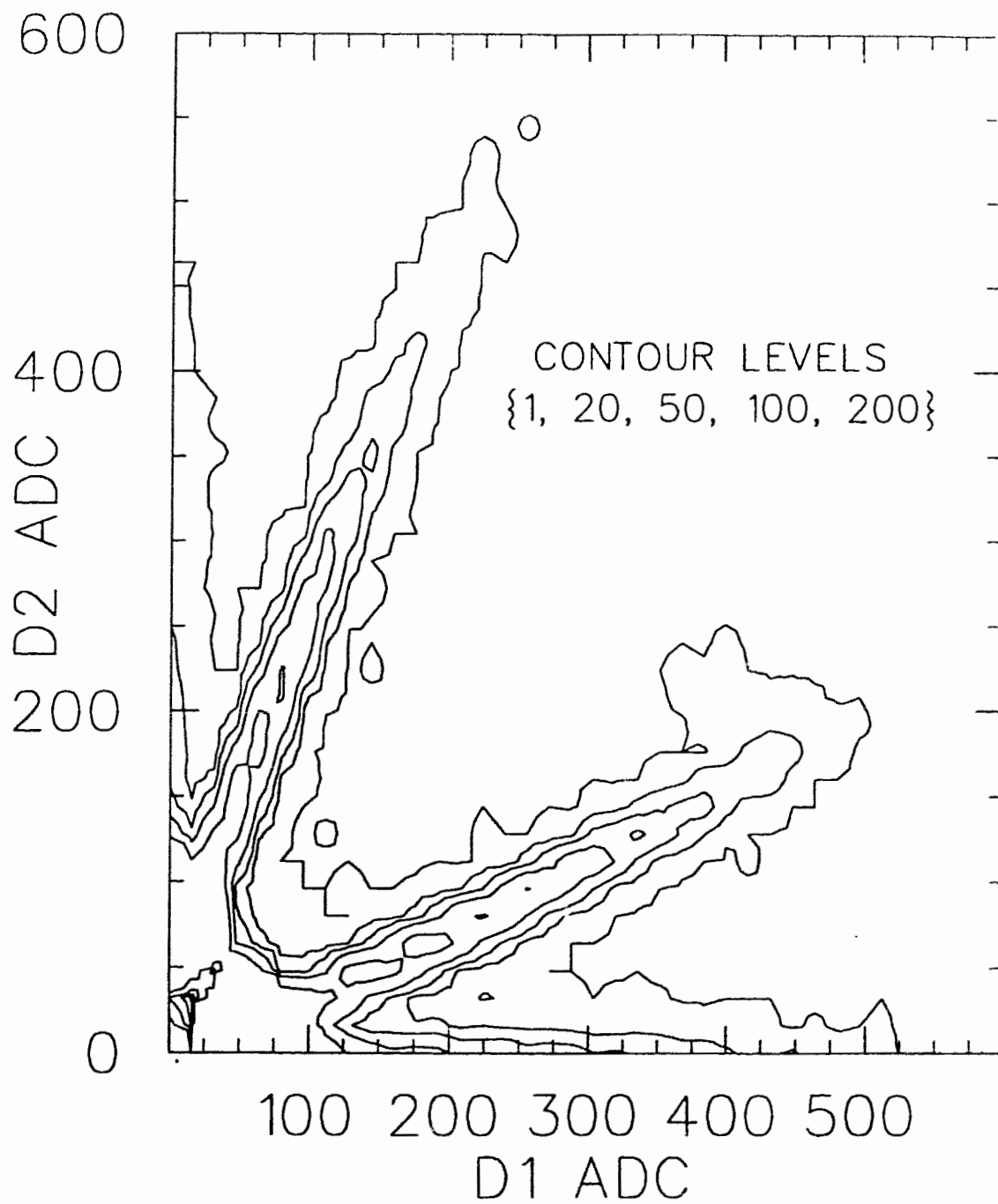


Figure 3.10: Two-dimensional spectrum of coincidence data recorded at detector station (1)

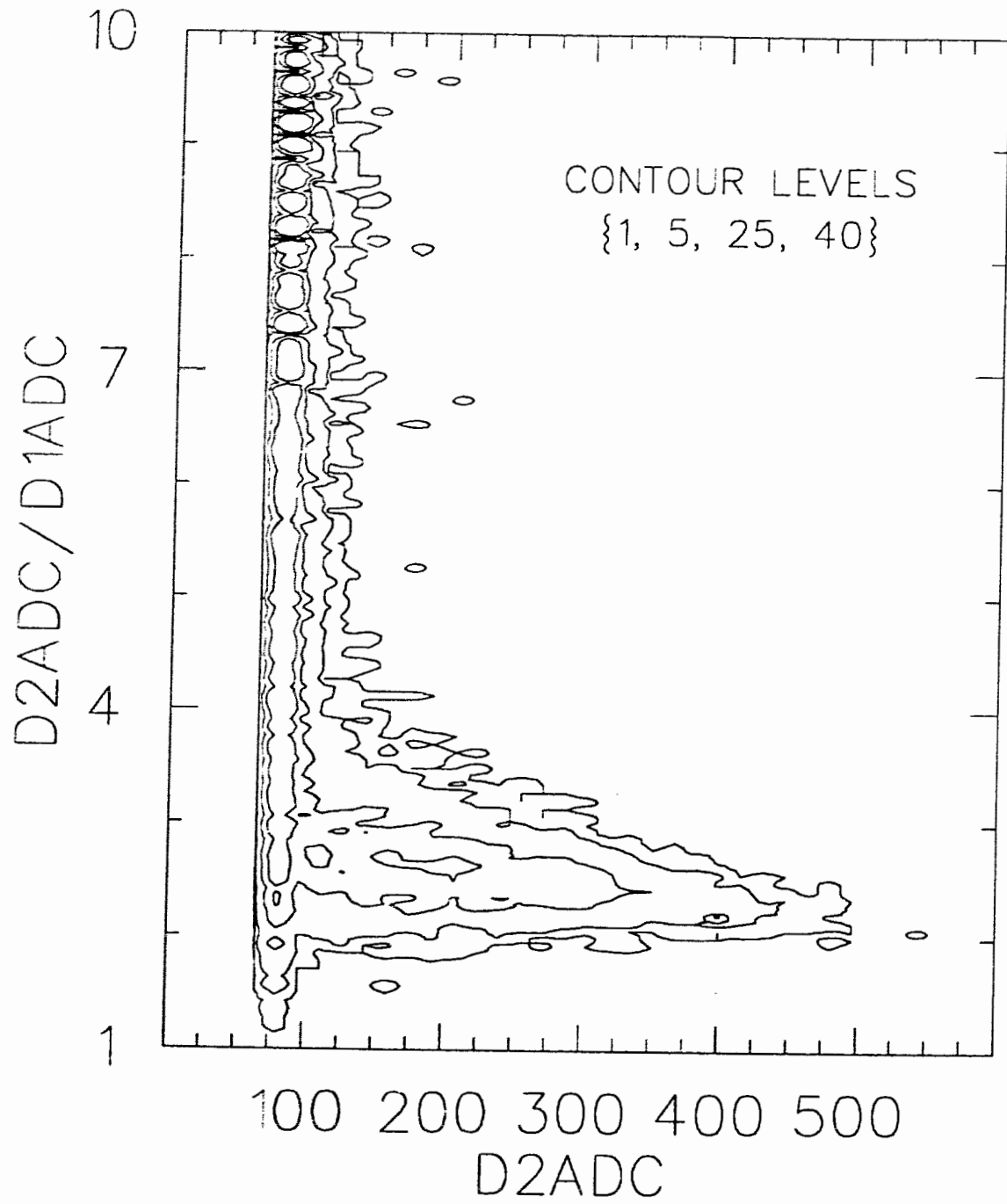


Figure 3.11: Pulse height ratio spectrum collected at detector station (1)

of about (4.7). The actual cuts varied depending on the detector pair involved.

The window defined by the ratio cuts, referred to as the acceptance region, was imposed on the coincidence data for all runs. Events in D2 falling within this window were defined as true D2 deuteron events while the coincident particle was defined as a true D1 alpha event. Figure 3.12 shows the acceptance region for D2 superimposed onto the ratio plot shown in figure 3.11.

The deuteron spectrum compiled in D2 over the twelve ${}^6\text{He}$ runs is shown in figure 3.13. At low energies, the deuteron spectrum is still contaminated by coincidence events involving beta particles.

To estimate the contribution made to the deuteron spectrum by beta and noise related coincidences, a second coincidence window was set in the data analysis software. The second window, referred to as the background region, is shown in figure 3.14. The background region was defined with a width equivalent to the width of the acceptance region and covered a pulse height ratio region where no true alpha/deuteron coincidences should be seen. The resultant background spectrum is plotted as a histogram superimposed on the D2 deuteron spectrum in figure 3.15.

To generate a final or net deuteron spectrum in D2, the lowest energy point in the background spectrum was scaled to equal the magnitude of the lowest energy point in the deuteron spectrum. Each point in the background spectrum was then multiplied by this scaling factor yielding a scaled background vector. The scaled background was then subtracted from the deuteron spectrum to produce the net D2 deuteron spectrum shown in figure 3.16. The statistical errors in the points as well as the error in the scaling procedure have been added in quadrature to produce the error bars of figure 3.16.

A similar procedure was followed to generate the total and net particle energy spectra for both D1 and D2. Figure 3.17 shows the four total event spectra while figure 3.18 shows the net spectra for alpha particles collected in D1 and D2.

Unfortunately, detector D1 was not sufficiently thick to stop the highest energy deuterons emitted by ${}^6\text{He}$. This is evidenced by the break through noted in figure 3.17. As a consequence of this, the shape of the D1 deuteron spectrum is distorted about the break through region and hence serves no practical purpose for the theoretical

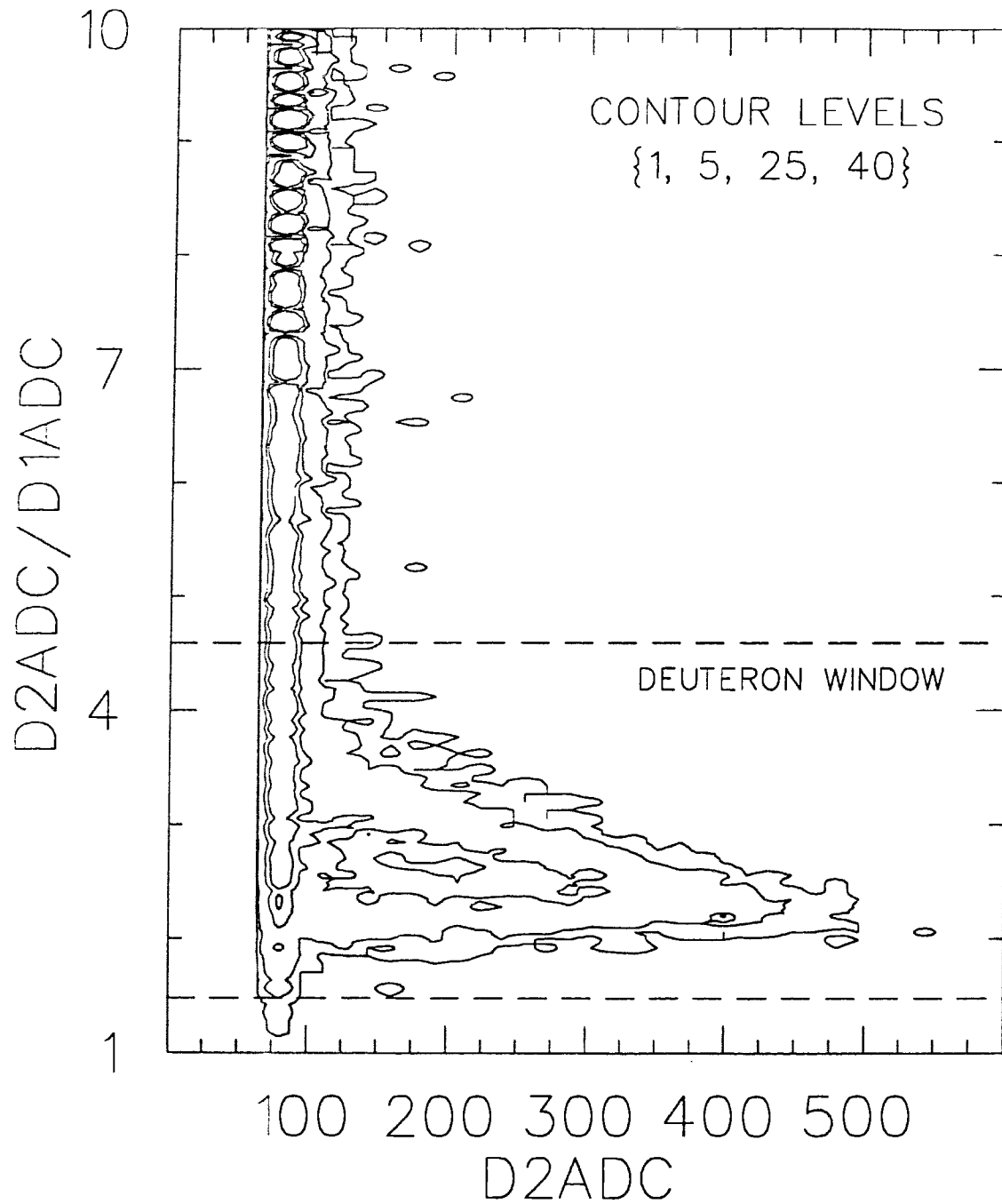


Figure 3.12: Pulse height ratio spectrum collected at detector station (1) with the deuteron or acceptance window displayed

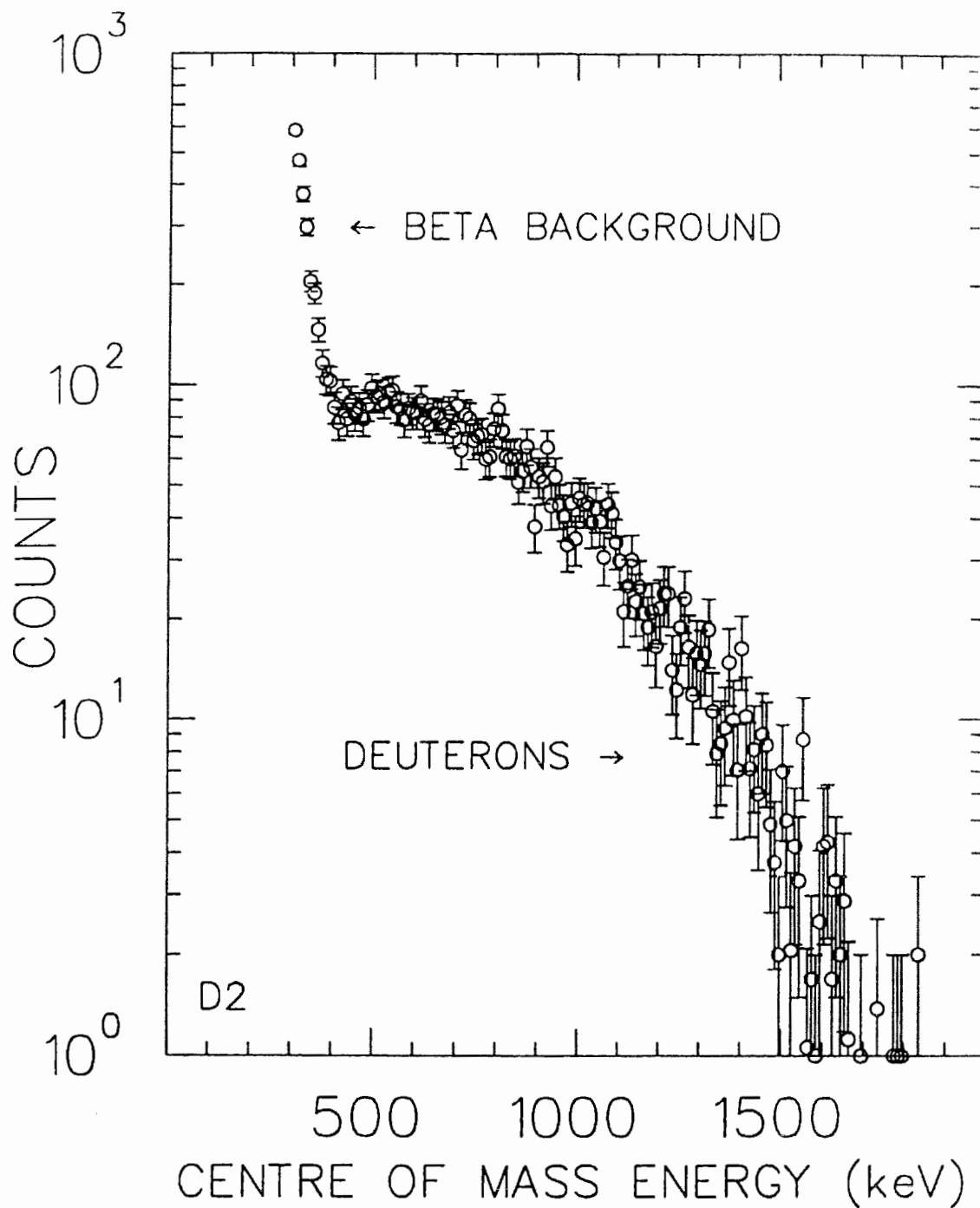


Figure 3.13: Raw deuteron spectrum collected in detector D2 with the acceptance window imposed on the data

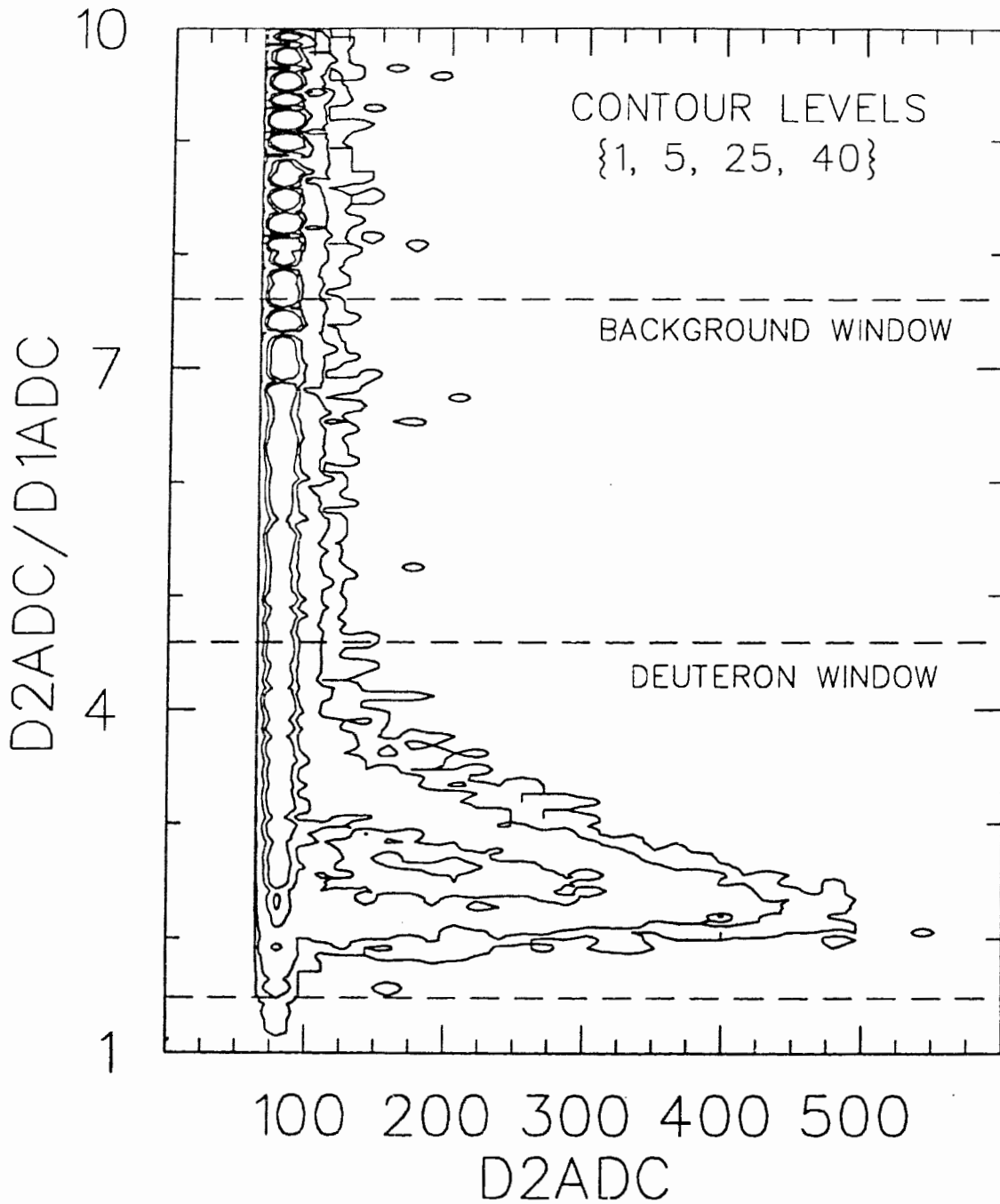


Figure 3.14: Pulse height ratio spectrum collected at detector station (1) with the acceptance window and background window displayed

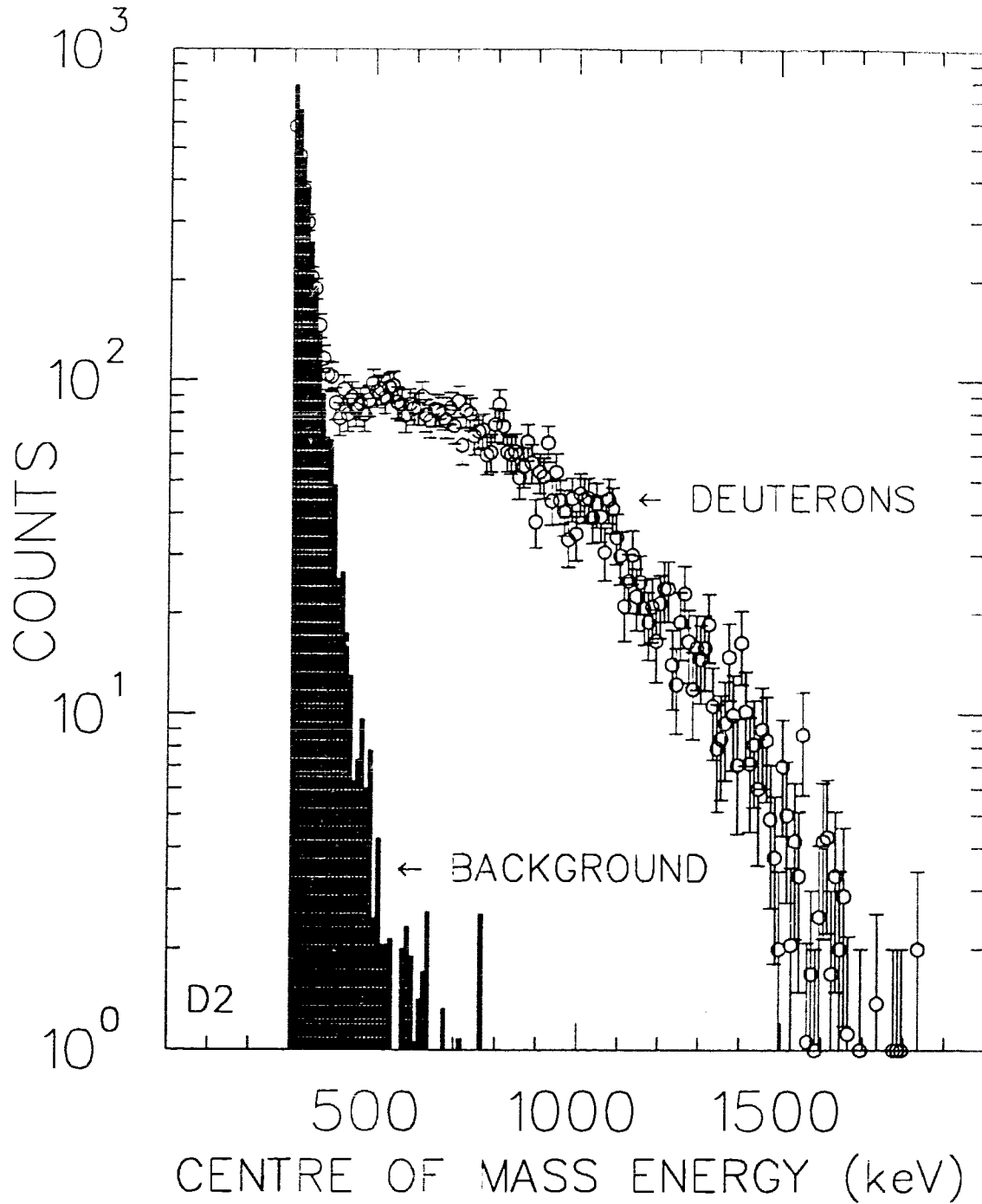


Figure 3.15: Raw deuteron spectrum in D2 overlaid by background spectrum collected in D2

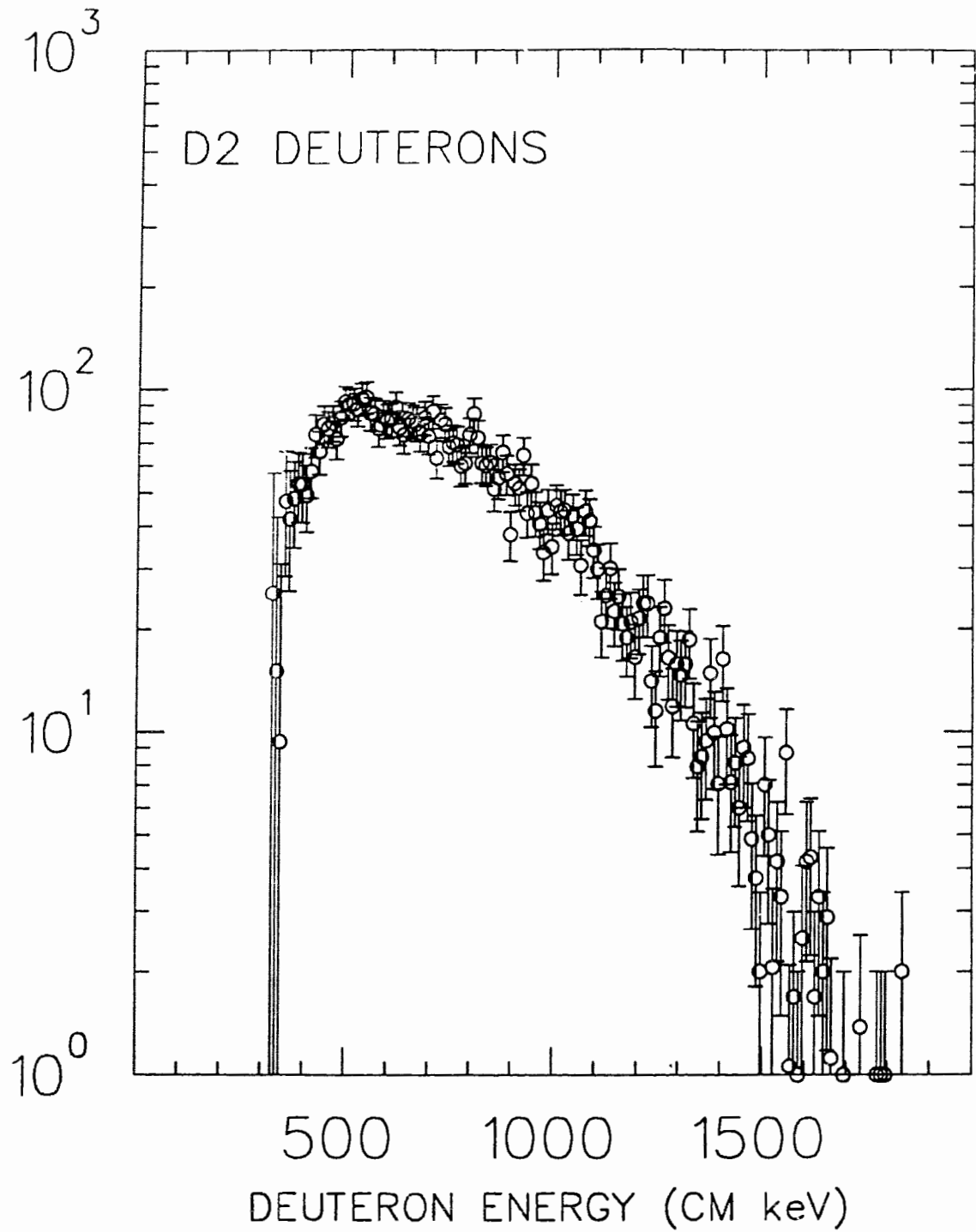


Figure 3.16: Net deuteron spectrum in D2 where the background spectrum has been scaled and subtracted from the raw deuteron spectrum

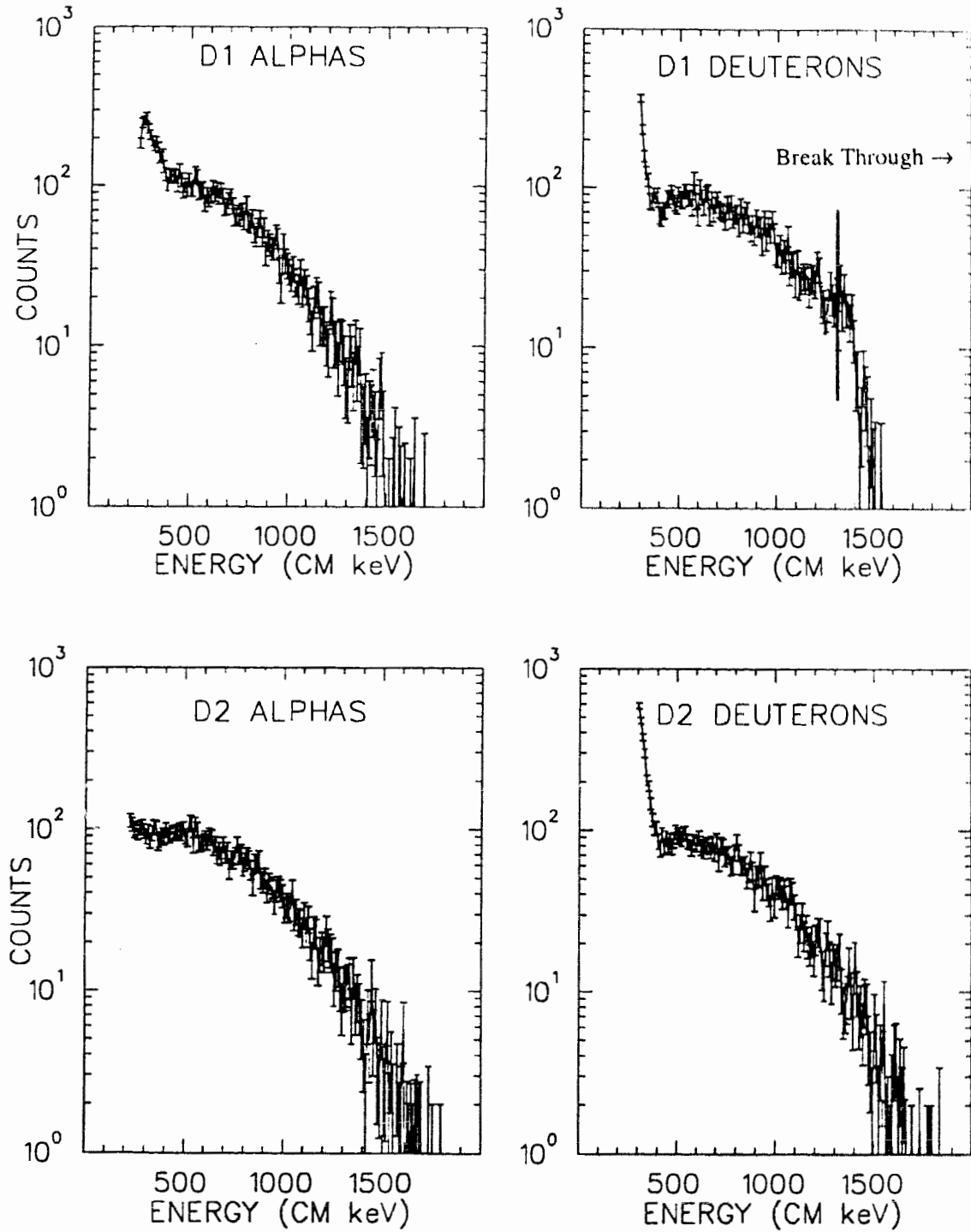


Figure 3.17: Four total or raw spectra collected at detector station (1)

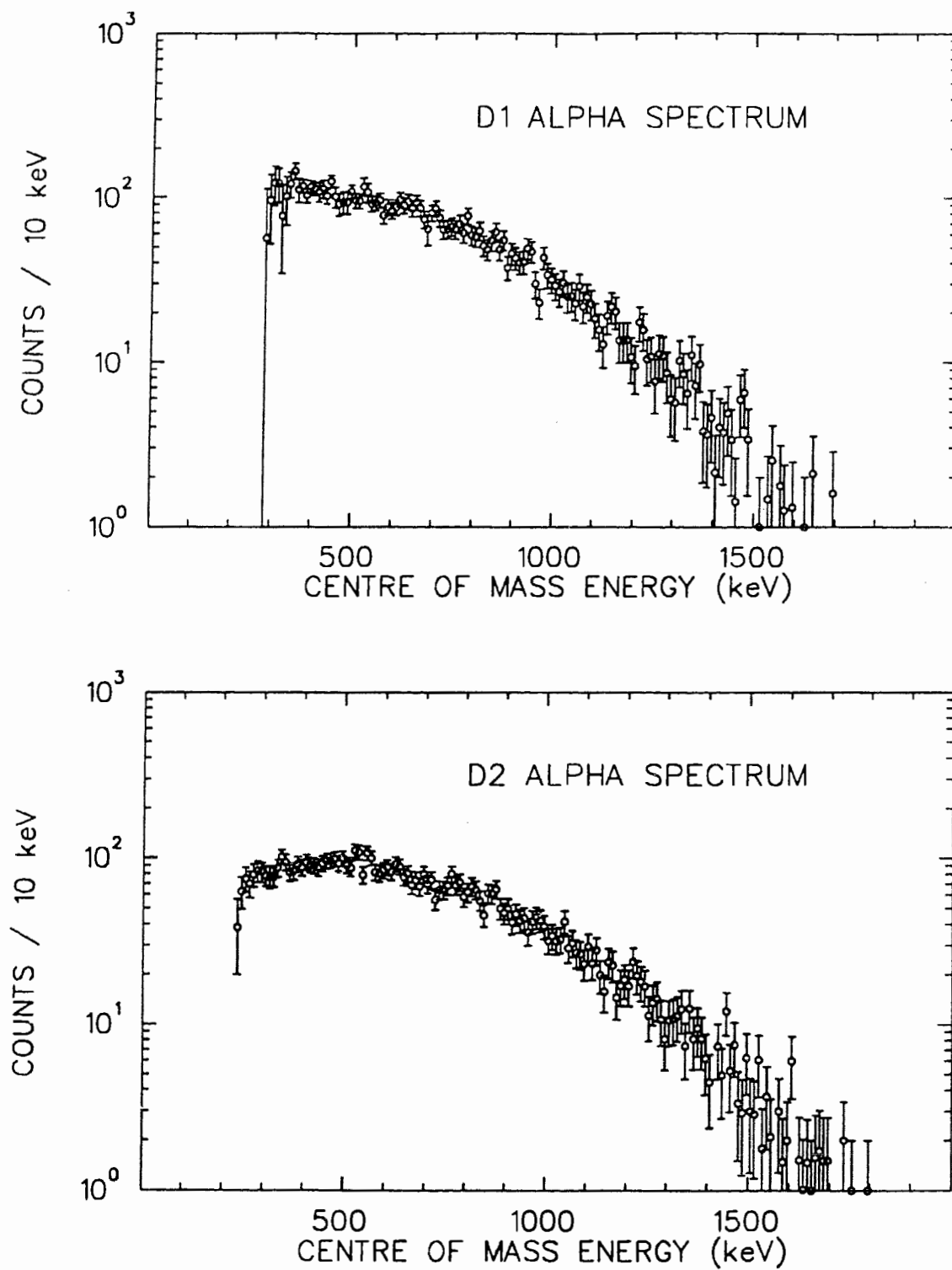


Figure 3.18: Alpha spectra collected in D1 and D2 where the background features have been scaled and subtracted from the raw spectra

interpretations discussed in chapter 5. Furthermore, the break through casts doubt on the reliability of the pulse height ratio selection for the identification of alpha particles in D2. It is not known how much of an impact this perturbation could have on the D2 alpha spectrum, therefore, even though the D2 alpha spectrum was included as a component in the theoretical interpretation of the spectrum shape, the analysis of the D2 alpha spectrum should be considered less reliable than the interpretation of the D2 deuteron spectrum. For this reason, also, a net spectrum for deuterons in D1 has not been included in this work.

3.7 Summary

The spectrum reported as the final energy spectrum is that for deuterons collected in D2. The reasons for this selection are that this spectrum is the most directly comparable with the previously published results of Riisager [7] and Borge [9] and has the most identifiable and clear beta background features.

The deuteron spectrum collected using this coincidence technique is superior to the spectra published by Riisager and Borge. The number of particle events reported by Riisager's group totalled 147 counts while the number of events reported by Borge's group totalled 362 counts. In this experiment, the number of deuteron events recorded above the 525 keV cut-off is greater than 4200 counts. This represents a statistical improvement of better than an order of magnitude, and should provide theorists with the ability to reliably test the constructs of their models.

One possible difficulty associated with the deuteron energy spectrum is its reliability at low energies. Above the 525 keV cut-off in the centre of mass, the deuteron spectrum is believed to be virtually background free. However, below this threshold, the coincidence technique may not be able to consistently detect a low energy alpha recoil nucleus. If this is true the collected spectrum will be artificially reduced below the deuteron kinetic energy for which the corresponding alpha particle is not reliably counted.

The determination of such a low energy coincidence failure is made particularly difficult by the presence of a significant beta background in the low energy region (see

section 4.4). From the beta response drop off it can be determined that the spectrum below about 300 keV in the centre of mass frame is wholly unreliable. However, it is not clear whether the region between 300 and 525 keV is reliable or not.

Chapter 4

Branching Ratio

4.1 Introduction

As previously indicated (section 1.3.1) the branching ratio of the ${}^6\text{He}$ decay to the $(\alpha + d)$ state is simply the probability that any ${}^6\text{He}$ nucleus will emit a deuteron. To generate an experimental branching ratio for this transition two quantities must be known; the total number of ${}^6\text{He}$ decays, and the number of $(\alpha + d)$ break-up transitions.

$$BR = \frac{N^{\circ} (\alpha + d)}{N^{\circ} {}^6\text{He}} \quad (4.1)$$

Since every ${}^6\text{He}$ decay, regardless of the branch through which it proceeds, emits a beta particle, the beta activity can be used as a measure of the total number of ${}^6\text{He}$ decays. The number of decays proceeding through the $(\alpha + d)$ exit channel can be found by recording the number of deuteron emissions from the ${}^6\text{He}$ sample. Therefore, the branching ratio can be written:

$$BR = \frac{N^{\circ} \text{deut}}{N^{\circ} \beta} \quad (4.2)$$

The detection system was designed with these quantities in mind. In the array at station (1), the two particle detectors, D1 and D2, facilitate the detection of alpha and deuteron particles while the ΔE -E beta telescope allows for the detection of beta events. Therefore, the detection system is capable of determining both the number of $(\alpha + d)$ decays and the total number of ${}^6\text{He}$ decays.

Because it is impractical to detect every beta and every deuteron emitted, the formula has to be modified such that the various efficiencies inherent to the experimental apparatus are taken into account. In this experiment, the working formula for the determination of the $(\alpha + d)$ branching ratio was of the form:

$$BR = \frac{N_d \epsilon_\beta}{N_\beta \beta_{con} \epsilon_d \epsilon_c} \quad (4.3)$$

where

N_d = the number of detected deuterons with energy in excess of 350 keV,

N_β = the number of detected beta particles within the telescope detector,

ϵ_d = the efficiency for deuteron detection,

ϵ_β = the efficiency for beta detection,

ϵ_c = the efficiency for coincidence detection,

β_{con} = the beta conversion factor,

Each of these quantities and the procedures for determining their values are discussed separately in the following sections.

4.2 Number of Detected Beta Particles N_β

The number of beta events N_β was determined from those events recorded in the beta telescope for each of the twelve ${}^6\text{He}$ experimental runs. The coincidence requirement set in the hardware effectively eliminated noise and background events that would otherwise have been present using a single beta detector. As a check, several background runs were performed in which no source was present in the detector array. The results of these runs indicated that the beta background in the telescope detector was negligible.

Furthermore, contributions to the beta spectrum made by decay events taking place at a detector station other than station (1) were estimated by inserting a beta source into detector station (2) and monitoring the telescope's response. Once again, the intensity of beta events recorded in the telescope with a beta source at station (2) was found to be orders of magnitude less than the intensity recorded with the same source in position at the first detector station.

Table 4.1: Number of detected beta particles

RUN	$N_{\beta} (*10^{-7})$
58	2.258 ± 0.005
59	2.643 ± 0.005
60	3.601 ± 0.006
64	1.550 ± 0.004
66	1.103 ± 0.003
67	2.007 ± 0.005
68	2.817 ± 0.005
69	2.349 ± 0.005
70	1.811 ± 0.004
71	3.371 ± 0.006
72	2.315 ± 0.005
73	3.048 ± 0.006

It should be noted that over the course of the ${}^6\text{He}$ experiment a prescale factor was set on the beta telescope to reduce the high computer dead time that would have occurred due to the high beta particle flux. This means that the number of beta events in the telescope spectrum must be multiplied by a factor of 100 to be a true measure of the total number of ${}^6\text{He}$ decays. The number of events detected in the beta telescope (multiplied by the prescale factor of 100) are listed in table 4.1 by ${}^6\text{He}$ run number.

4.3 Beta Conversion Factor β_{con}

For a beta particle to be counted in the beta telescope the energy of the beta must be above an energy cut-off determined by the E detector threshold and the magnitude of the energy losses incurred on passing through the ΔE detector. From the hardware cut-off in the germanium, E, detector and an estimate of the energy loss in the ΔE detector, the value of the energy threshold has been calculated to be (810 ± 100) keV.

Therefore, betas emitted with energy less than about 800 keV will be invisible to the beta detection system. To correct for this shortfall, a beta conversion factor, β_{con} ,

has been included in the formula for the determination of the branching ratio.

The value of β_{con} for ${}^6\text{He}$ was determined by constructing a theoretical beta spectrum for the dominant beta transition based on the formalism outlined in references [24], [27], and [37]. The theoretical spectrum was then integrated over the full energy range and over the range visible to the beta telescope (i.e., energies in excess of 810 keV). The value of β_{con} was then equal to the total integrated area divided by the integrated spectrum above 810 keV.

The result indicated that the value of β_{con} for ${}^6\text{He}$ was equal to (2.02 ± 0.32) . This suggests, then, that about half of the emitted beta particles were not visible to the telescope detector.

4.4 Coincidence Efficiency ϵ_c

In order to distinguish between the alphas and deuterons emitted in the decay of ${}^6\text{He}$ it was necessary to set a coincidence condition for events in detectors D1 and D2. Except for the ideal case, the coincidence solid angle subtended by each of the particle detectors is less than the solid angle subtended by the detectors for singles detection. Figure 4.1 demonstrates the relationship between the singles solid angle and the coincidence solid angle for the best, worst and middle case scenarios.

As a consequence of the solid angle or efficiency reduction caused by imposing the coincidence condition, it is necessary to include a coincidence efficiency term (ϵ_c) in the branching ratio formula.

The coincidence efficiency term effectively scales the number of events detected within the coincidence geometry up to the number of events that would have been detected had the counting system been ideal. Equivalently, the coincidence efficiency scales the coincidence solid angle up to the singles solid angle for each of the detectors.

Fortunately, it is possible to determine the coincidence efficiency for each of the particle detectors in each of the ${}^6\text{He}$ runs. This is accomplished by examining the number of coincident events recorded by a detector and the number of singles events recorded in the same device. The coincidence efficiency for detector (i) is then simply the ratio of the number of coincidences recorded in detector (i) to the number

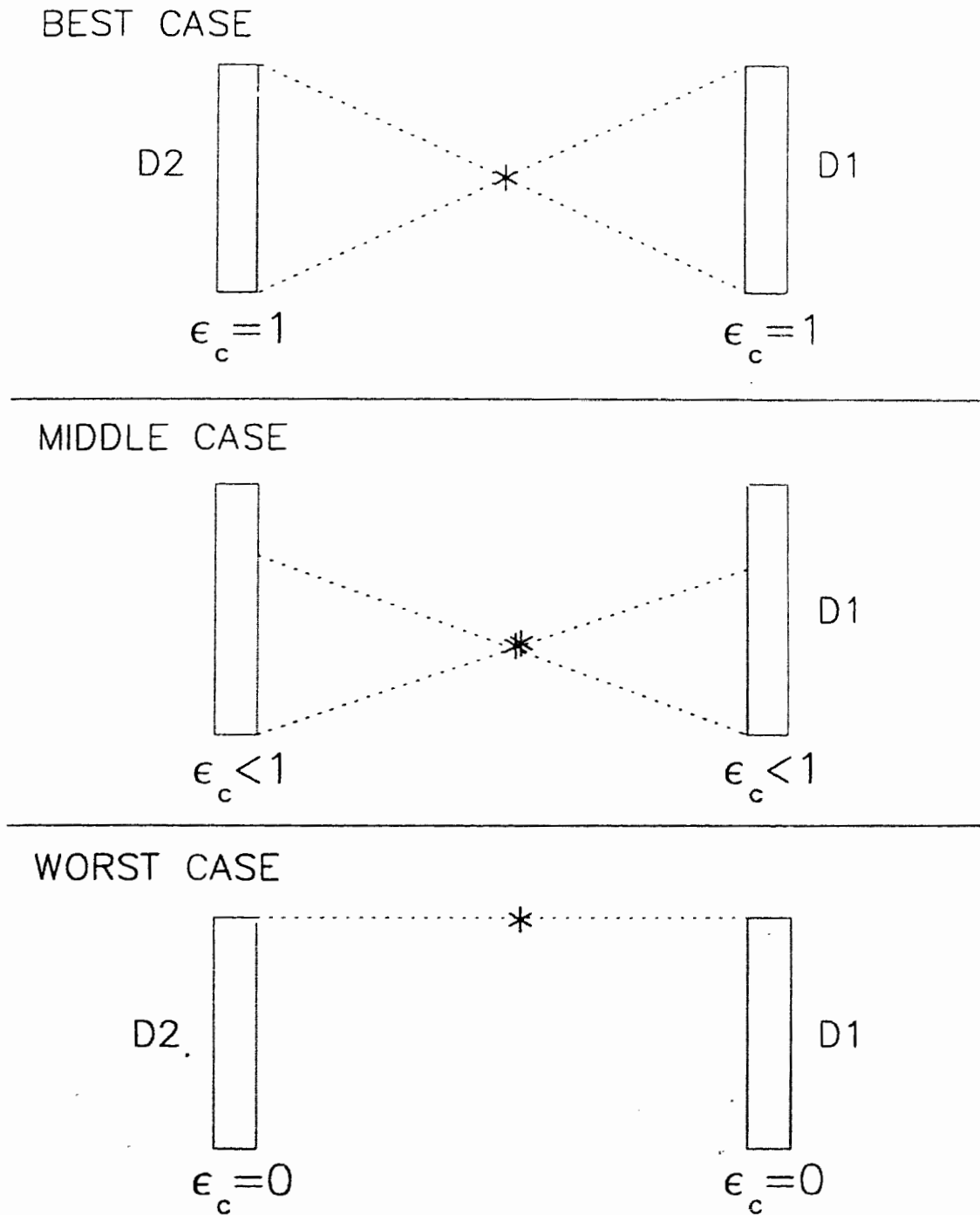


Figure 4.1: The coincidence efficiencies and their dependence on the source/detector geometry

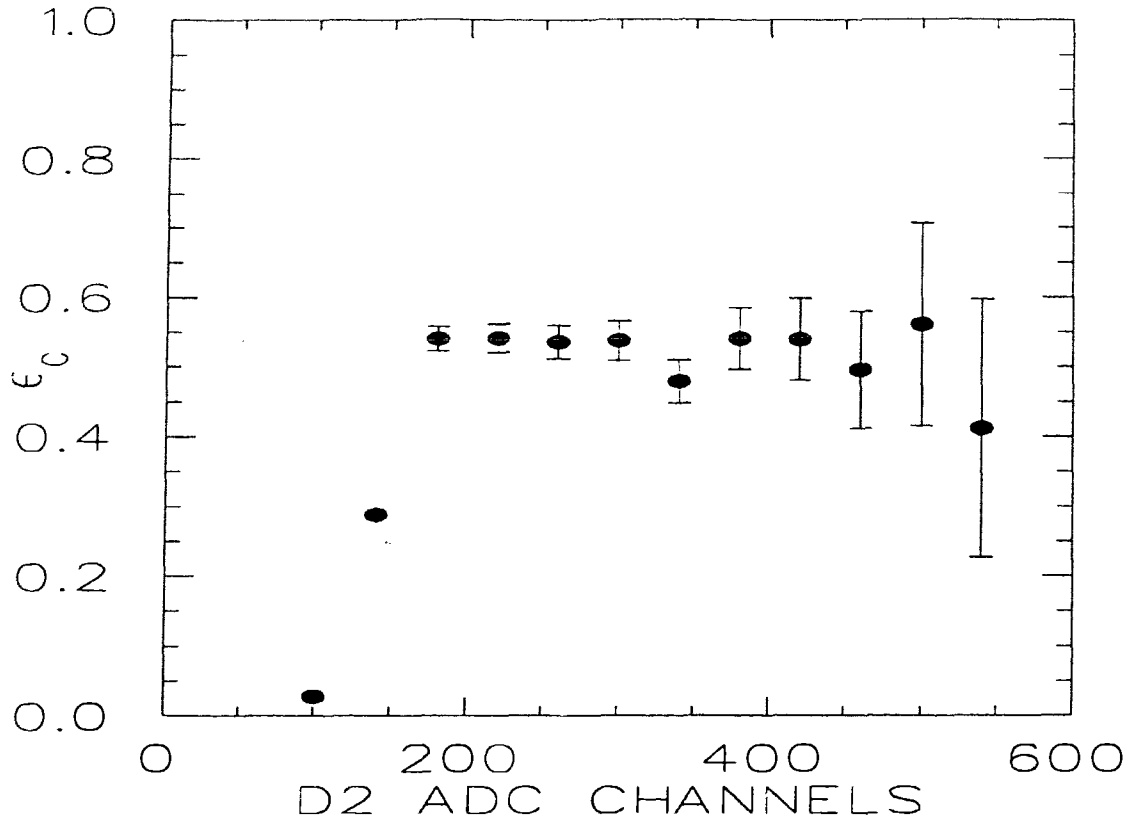


Figure 4.2: The coincidence efficiency of Detector D2 as a function of ADC channel of singles recorded in detector (i). In mathematical form this may be expressed as:

$$\epsilon_c = N_{coin}/N_{sing} \quad (4.4)$$

Where N_{sing} is the number of singles events and N_{coin} is the number of coincidence events recorded.

The determination of the coincidence efficiencies appears to be trivial. However, it is also important to establish if the calculated coincidence efficiency is valid over the entire energy range of the particle energy spectrum. To observe the coincidence efficiency as a function of energy, the singles and coincidence spectra were partitioned into bins with bin width equal to forty ADC channels. A coincidence efficiency was then calculated for each of the ADC bins using equation 4.4. The calculated coincidence efficiency was plotted as a function of ADC channel and is shown in figure 4.2.

Table 4.2: Coincidence efficiency for Detectors D1 and D2 as a function of ${}^6\text{He}$ run number

RUN	D1 ϵ_c	Error	D2 ϵ_c	Error
58	0.478	0.022	0.648	0.033
59	0.369	0.018	0.523	0.027
60	0.251	0.012	0.382	0.020
64	0.379	0.024	0.464	0.033
66	0.357	0.027	0.462	0.039
67	0.315	0.018	0.423	0.027
68	0.314	0.016	0.414	0.023
69	0.226	0.014	0.261	0.020
70	0.248	0.016	0.311	0.025
71	0.484	0.018	0.602	0.025
72	0.518	0.023	0.655	0.033
73	0.527	0.020	0.649	0.027

Apart from minor statistical variations, the ϵ_c term is found to be consistent down to about 160 ADC channels. At lower energies, however, the coincidence efficiency drops off in a dramatic fashion. The interpretation of this effect is that the ϵ_c drop-off below 160 channels is due to a sharp rise in the number of singles events recorded below this threshold. The increase in detected singles is caused by the detector responding to, and registering as an event, transmitted beta particles.

As a direct consequence of the coincidence efficiency catastrophe at low energies, the branching ratio determination is limited to the energy region in which the coincidence efficiency is uniform. Converting ADC channels to energy for both detectors D1 and D2, it was found that the low energy cut-off occurred at a deuteron energy of about 350 keV in the laboratory frame. Therefore, the coincidence efficiencies are only reliable above this threshold and thus the branching ratio quoted in this experiment is for deuteron events above 350 keV.

Table 4.2 lists the calculated coincidence efficiency in the region of uniformity for both detectors D1 and D2 for each of the ${}^6\text{He}$ data collection runs.

Table 4.3: Number of deuterons detected in D1 and D2 as a function of ${}^6\text{He}$ run number

RUN	D1 N_d	Error	D2 N_d	Error
58	443	21	455	21
59	406	20	387	20
60	334	18	365	19
64	200	14	227	15
66	146	12	146	12
67	242	16	254	16
68	356	19	342	19
69	210	15	159	13
70	181	14	150	12
71	726	30	643	25
72	502	22	474	22
73	722	27	714	27

4.5 Number of Detected Deuterons N_d

For each ${}^6\text{He}$ run, deuteron events were separated from alpha events by the coincidence method outlined in section 3.6. For the purposes of the branching ratio calculation, only deuteron events above the low energy cut-off imposed by the coincidence efficiency were counted. Therefore, the number of detected deuterons (N_d) for each detector was determined by summing the deuteron energy spectrum above the threshold energy of 350 keV in the lab frame. Table 4.3 lists the value of N_d for detectors D1 and D2 by ${}^6\text{He}$ run number.

4.6 Ratio of Detection Efficiencies $\epsilon_\beta/\epsilon_d$

The ratio of the beta detection efficiency to the particle detection efficiency was calculated using three independent methods. The first method was to determine the efficiency ratio based on the geometry of the detection system, the second method utilized sources with known decay characteristics to solve for the effective efficiency

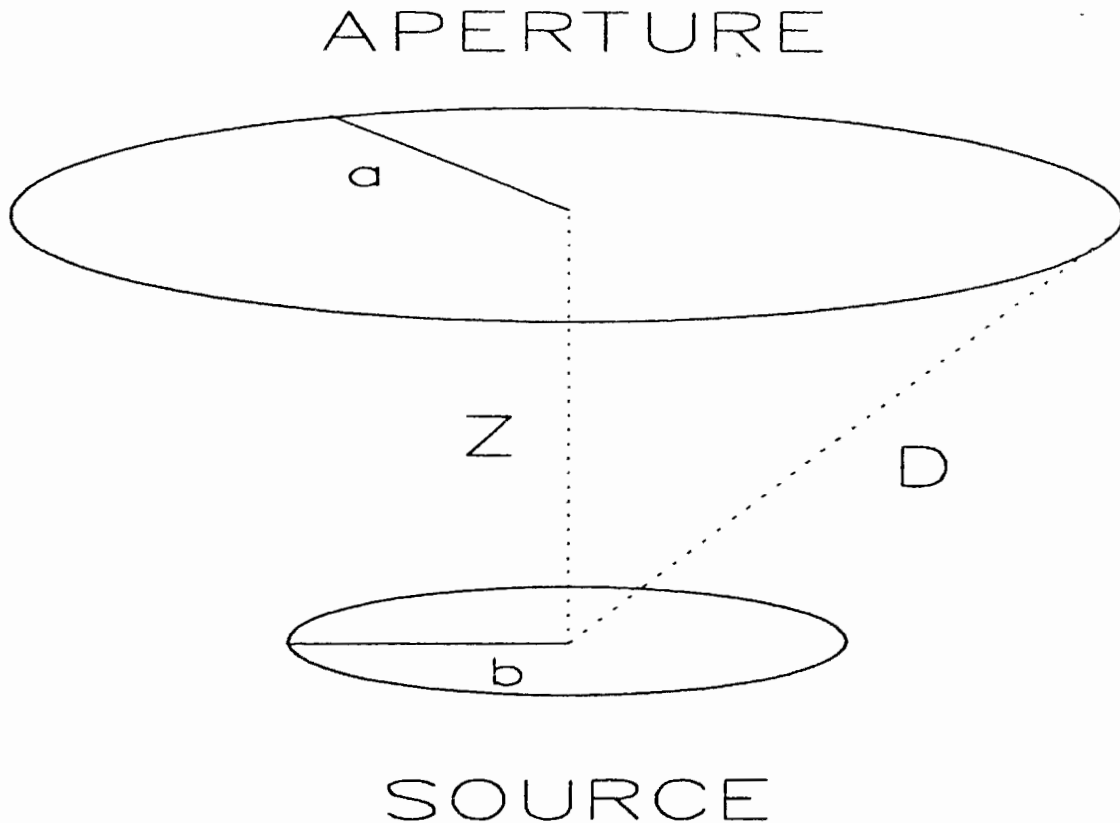


Figure 4.3: General case diagram for relative source/detector geometry

ratio, while the third method relied on the observed values of the coincidence efficiencies (ϵ_c) to elucidate the efficiency ratio ($\epsilon_\beta/\epsilon_d$). Each method is discussed separately in the following sections.

4.6.1 Geometric Method

Ideally, the detection efficiency of a collection device such as a charged particle detector is equal to the fraction of 4π subtended by the device. Therefore, the individual beta and particle detection efficiencies may be calculated from the known source/detector geometry and the area of the detector's aperture. Figure 4.3 shows a general case diagram of the geometry involving a radioactive source coaxial with the surface face of a circular detection device. Here, a is the radius of the detector face, b is the radius of the source, Z is the source-to-detector separation and D is a

parameter defined as:

$$D = (a^2 + Z^2)^{1/2} \quad (4.5)$$

In the simplest case, where the activity is confined to a point source ($b = 0$), the fraction of 4π subtended by the detector aperture may be found from the equation:

$$G_p = 1/2(1 - Z/D) \quad (4.6)$$

For a uniformly spread radioactive source with finite radius, b , the fraction of 4π subtended by the detector is then estimated from the equation:

$$G_p' = G_p - (3/16)b^2a^2Z/D^5 \quad (4.7)$$

For the branching ratio calculation, D1 and D2 were used as particle detectors while the telescope consisting of ΔE and E components was used as a Beta counter. The active areas and radii for each of these detectors were taken from the specification sheets of the manufacturer and measurements of the source to detector distances, Z , were made at various times over the course of the ${}^6\text{He}$ experiment.

Prior to implantation within the Carbon foil, the ${}^6\text{He}$ beam passed through a collimator with diameter equal to 8mm. The source radius, b , for the system was assumed to be about 4mm. Further discussions centered around beam optics have indicated that the actual implantation radius could be as low as 3mm and as high as 5mm. The 5mm maximum is absolute due to the fact that above a 5mm offset distance the activity would be implanted in the Aluminum card rather than the Carbon foil. This would eliminate the possibility of coincidence counting.

Table 4.4 summarizes the values of the parameters necessary to calculate the Beta and Particle detection efficiencies.

The large error in the D1 Z value is due to the fact that for some measurements of the system geometry, the outer edge of the detector casing was seen to overlap the edge of the Aluminum sleeve while for other measurements this was not observed. The possible variation of the source to D1 separation distance manifests itself as a large uncertainty in this Z parameter. Similar variation in the position of detector D2

Table 4.4: Parameter values necessary to determine the Geometric efficiency of the various charged particle detectors at station(1)

Particle Detector	Detector Radius (a) (mm)	Source Radius (b) (mm)	Seperation Distance (Z) (mm)
D1	4.0 ± 0.15	4 ± 1	5.54 ± 0.90
D2	4.0 ± 0.15	4 ± 1	5.35 ± 0.22
ΔE	4.0 ± 0.15	4 ± 1	14.48 ± 0.30
E	8.0 ± 0.15	4 ± 1	42.20 ± 1.1

Table 4.5: Geometric solid angle for the various charged particle detectors at station (1)

Particle Detector	Point Source G_p	Uniform Source G_p'
D1	0.095 ± 0.023	0.079 ± 0.031
D2	0.100 ± 0.009	0.082 ± 0.015
ΔE	0.018 ± 0.0005	0.017 ± 0.0016
E	0.0087 ± 0.0003	0.0087 ± 0.0006

was not observed, and, hence, for this calibration technique, the geometric detection efficiency of D2 is considered more reliable than that for D1.

From these values, the fraction of 4π subtended by the various detectors was calculated using equations 4.6 and 4.7. The results of the solid angle calculations are shown in table 4.5. These data indicate that for the beta telescope the solid angle or efficiency is controlled by the E component rather than the ΔE component of the detector. Using the E efficiency as the beta counting efficiency, the ratio of beta to particle detection efficiency ($\epsilon_\beta/\epsilon_d$) for detectors D1 and D2 are (0.11 ± 0.05) and (0.11 ± 0.02) , respectively.

4.6.2 Sources Method

The formula used to calculate the experimentally determined branching ratio of ${}^6\text{He}$ decaying to the $(\alpha + d)$ state was:

$$BR = \frac{N_d \epsilon_\beta}{N_\beta \beta_{con} \epsilon_d \epsilon_c} \quad (4.8)$$

Using sources with known decay properties, that is, nuclides with known beta delayed branching ratios, equation 4.8 can be rearranged to solve for the ratio of detection efficiencies $\epsilon_\beta/\epsilon_d$.

$$\frac{\epsilon_\beta}{\epsilon_d} = \frac{BR * N_\beta \beta_{con} \epsilon_c}{N_d} \quad (4.9)$$

Where all terms have been previously defined and are determined by methods identical to those for the ${}^6\text{He}$ runs.

Two sources were used for this method of determining the ratio of detection efficiencies. One was ${}^{16}\text{N}$ and the other was ${}^8\text{Li}$. These are discussed separately in the following sections.

The ${}^{16}\text{N}$ Decay

A radioactive ion beam of ${}^{16}\text{N}$ nuclei was produced at TISOL by bombarding a Zeolite target with energetic protons. The ${}^{16}\text{N}$ decay properties were observed under conditions identical to those of the ${}^6\text{He}$ runs. A total of two hours of experimental beam time was devoted to monitoring the decay shortly after the ${}^6\text{He}$ data runs.

The transition of interest in the ${}^{16}\text{N}$ decay is the beta delayed break-up to the $(\alpha + {}^{12}\text{C})$ state. The branching ratio for this well-known decay has been previously measured to be $(1.2 \pm 0.05) * 10^{-5}$ [22]. Substituting this value into equation 4.9 gives

$$\frac{\epsilon_\beta}{\epsilon_d} = (1.2 * 10^{-5}) \frac{N_\beta \beta_{con} \epsilon_c}{N_d} \quad (4.10)$$

The value of the beta conversion factor, β_{con} , for the nitrogen source was determined by a method completely analogous with that outlined in section 4.3 for the ${}^6\text{He}$ runs. In this case, however, there are two significant beta branches in the decay scheme. A theoretical beta spectrum was constructed for both transitions and conversion factors generated for each beta exit channel. The overall conversion factor for ${}^{16}\text{N}$

was determined by weighting the two individual transitions based on the branching ratio or probability of that transition occurring. The result for the value of β_{con} for ^{16}N was (1.33 ± 0.18) .

The values of N_β and N_d were obtained from the number of responses in the beta telescope and number of alpha particles detected in the particle detectors. The values of these parameters were found to be, $(8.88 \pm 0.03) * 10^6$ for N_β , (468 ± 22) for N_d in D1, and, (459 ± 22) for N_d in D2. The coincidence efficiencies for D1 and D2 were calculated to be (0.229 ± 0.12) and (0.316 ± 0.017) , respectively. Substituting these values into equation 4.10 and adding the errors in quadrature, the ratio of beta to particle detection efficiency $\epsilon_\beta/\epsilon_d$ for D1 and D2 were found to be (0.069 ± 0.011) and (0.098 ± 0.016) , respectively.

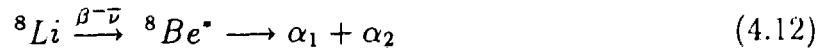
The ^8Li Decay

A radioactive beam of ^8He was produced at the TISOL facility from the same graphite target used to produce ^6He . ^8He decays to ^8Li with a half-life of (0.119) [8] seconds according to the equation:



The short half-life of ^8He relative to the beam collection and wheel move time ensured that most of the activity observed at the detector stations was due to ^8Li rather than ^8He . In total, four ^8Li runs were conducted; two immediately before, and two immediately after the ^6He runs. The total beam time devoted to ^8Li was about nine hours.

The transition of interest in the decay of ^8Li is the beta delayed break-up to the $(\alpha + \alpha)$ state. In this process, ^8Li emits a beta particle to form an excited state of ^8Be that promptly breaks apart into a pair of alpha particles. The overall reaction may be written:



Once again the equation used to solve for the ratio of beta to particle detection efficiencies is

$$\frac{\epsilon_\beta}{\epsilon_d} = \frac{BR * N_\beta \beta_{con} \epsilon_c}{N_d} \quad (4.13)$$

When ${}^8\text{Li}$ beta decays to the excited state of ${}^8\text{Be}$ the excited ${}^8\text{Be}$ nuclide breaks apart into two alpha particles 100% of the time. Therefore, the branching ratio for this reaction is equal to unity. The calculation of the efficiency ratio is then simplified to:

$$\frac{\epsilon_\beta}{\epsilon_d} = \frac{N_\beta \beta_{con} \epsilon_c}{N_d} \quad (4.14)$$

It must be remembered, however, that all of the detected betas N_β are not necessarily due to the decay of ${}^8\text{Li}$. It is possible that some of the original ${}^8\text{He}$ activity survives long enough to be observed in the beta telescope. The N_β term, then, must be corrected for these extraneous events. Therefore a correction term f_{Li} must be incorporated into the efficiency ratio formula where f_{Li} is equal to the fraction of N_β due to the decay of ${}^8\text{Li}$.

$$\frac{\epsilon_\beta}{\epsilon_d} = \frac{(N_\beta f_{Li}) \beta_{con} \epsilon_c}{N_d} \quad (4.15)$$

Furthermore, since the break-up species of ${}^8\text{Be}$ are identical (i.e., both products in the break-up are alpha particles) it is impossible to distinguish between α_1 and α_2 by experimental means. As a consequence, the number of detected particles N_d must be adjusted to reflect this experimental ambiguity.

Since the $(\alpha + \alpha)$ channel was determined by a coincidence technique, an event is counted only when both alphas are seen. In any given particle detector, there is a 0.5 probability that the event was due to α_1 and a 0.5 probability that the event was due to α_2 . Therefore, the number of detected particles must be corrected by a factor of 0.5 to ensure that only one of the two alpha particles is taken as the particle of interest.

$$\frac{\epsilon_\beta}{\epsilon_d} = \frac{(N_\beta f_{Li}) \beta_{con} \epsilon_c}{N_d * 0.5} \quad (4.16)$$

This was the final equation used to determine the ratio of detection efficiencies $\epsilon_\beta/\epsilon_d$ through the observation of the decay properties of ${}^8\text{Li}$.

The determination of the fraction of betas due to the ${}^8\text{Li}$ decay, f_{Li} , was based on the beta half-life spectrum recorded in the beta telescope. The decay sequence at mass ($A=8$) is a mother-daughter decay of the form:

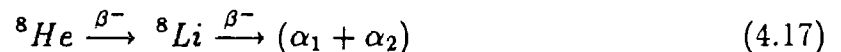


Table 4.6: Half-life fits to beta spectra collected during the ^8Li calibration runs

Calibration Run	^8He Initial Activity (A)	^8Li Initial Activity (B)
53	38.4 ± 5.3	102.5 ± 1.5
54	56.8 ± 5.2	86.6 ± 1.3
78	38.7 ± 4.8	70.5 ± 1.2
80	26.3 ± 4.5	66.2 ± 1.1

with the ^8He and ^8Li beta decay half-lives equal to (119.0) and (840.3) milliseconds, respectively [8]. The function used to fit the half-life spectrum consisted of three terms. The first term accounted for beta activity due to the residual ^8He activity present in the foil during the beta recording period at detector station (1). The second term accounted for beta events recorded in the telescope due to the ^8Li activity already present in the foil at the instant the foil was exposed to the detector station, and the third term accounted for ^8Li activity generated as a consequence of the initial ^8He sample decaying to a quantity of ^8Li during the data collection period. The overall equation used to fit the beta half-life spectrum as a function of time was of the form [24]:

$$A * e^{(-\lambda_{\text{He}}t)} + B * e^{(-\lambda_{\text{Li}}t)} + A * \frac{\lambda_{\text{Li}}}{(\lambda_{\text{Li}} - \lambda_{\text{He}})} * [e^{(-\lambda_{\text{He}}t)} - e^{(-\lambda_{\text{Li}}t)}] \quad (4.18)$$

where the λ_i are the known decay constants of ^8Li and ^8He , and the parameters A and B , which were allowed to vary, represent the initial activity of ^8He and ^8Li , respectively.

In the fit, the points in the spectrum were weighted as an inverse function of their variance while A and B were varied until the calculated chi squared value reached a minimum. As an example, figure 4.4 shows the half-life spectrum collected in the beta telescope for one of the ^8Li runs and the results of the half-life fit to the spectrum as outlined above. This procedure was repeated for each of the ^8Li experimental runs with table 4.6 listing the results of the fits by ^8Li run number. Knowing the initial activity of ^8He present in the Carbon foil and the overall time frame of the half-life

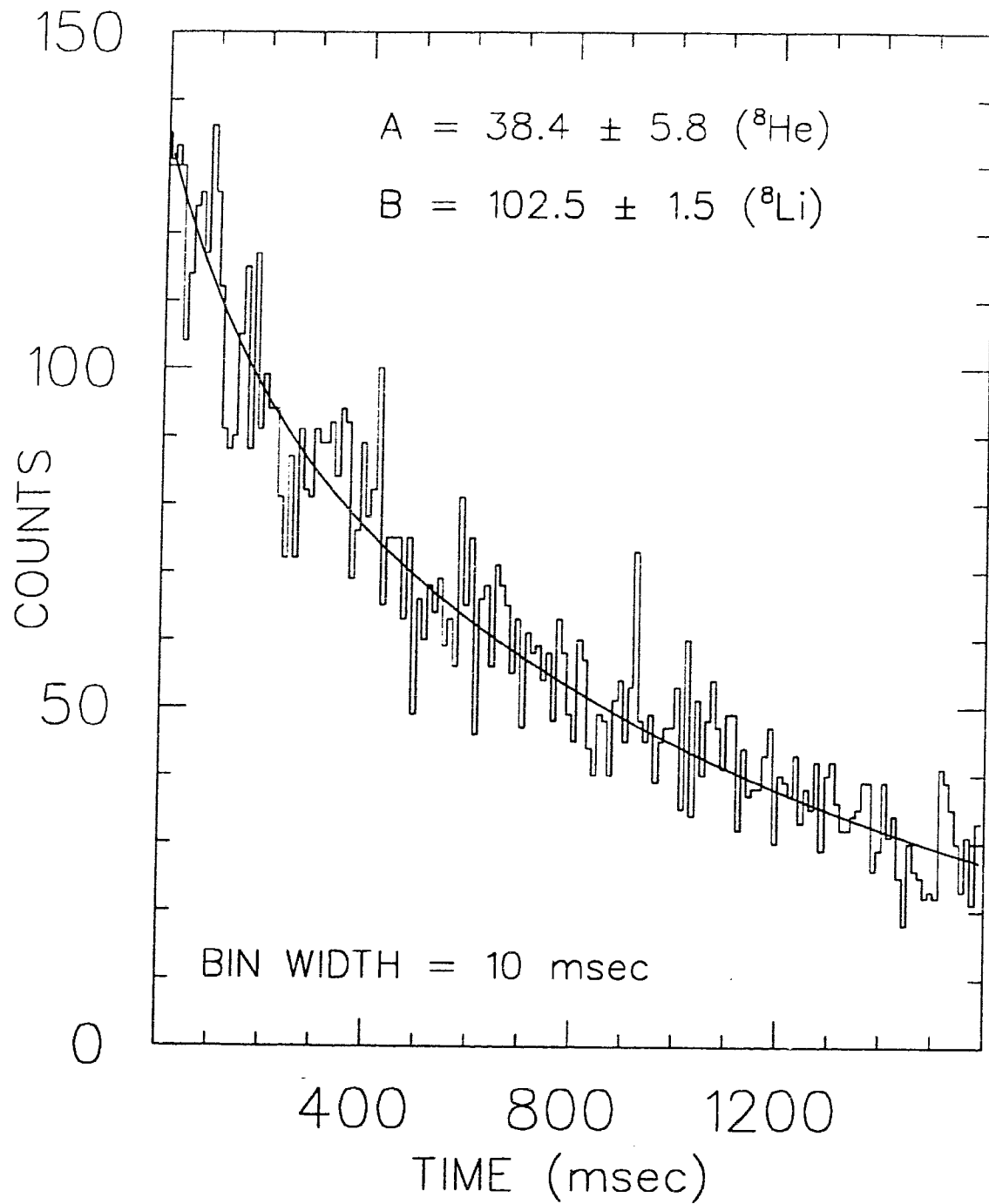
Figure 4.4: Fit to beta Half-life spectrum assuming contributions from ${}^8\text{He}$ and ${}^8\text{Li}$

Table 4.7: Fraction of Beta events due to the decay of ^8Li

Calibration Run	Beta Fraction f_{Li}
53	0.932 ± 0.025
54	0.887 ± 0.023
78	0.904 ± 0.028
80	0.929 ± 0.029

curve, the total contribution made by ^8He to the beta spectrum can be calculated. The number of beta events due to ^8He is found from the equation:

$$\Delta N = \frac{A^{\circ}_{He}}{\lambda_{He}} * (1 - \exp(-\lambda_{He}T)) \quad (4.19)$$

where A° is the initial ^8He activity and λ_{He} is the decay constant of ^8He , T is the total time span of the half-life spectrum and ΔN is the total number of beta events that are due to ^8He decays.

The number of beta events due to ^8Li then is simply equal to the total number of events minus the number of events due to ^8He . Knowing the number of beta events due to ^8Li and the total number of beta events recorded in the half-life spectrum, it is possible to calculate the fraction of beta events due to ^8Li , (f_{Li}). Table 4.7 lists the value of f_{Li} calculated for each of the four runs on mass ($A=8$). In all cases, the error includes the error in the fit and the statistical errors added in quadrature.

Knowing f_{Li} , and determining N_{β} , β_{con} , N_d and ϵ_c in a manner analogous to the method outlined for the ^6He runs, it is possible to calculate the ratio of detection efficiencies, $\epsilon_{\beta}/\epsilon_d$, for each run from the formula:

$$\frac{\epsilon_{\beta}}{\epsilon_d} = \frac{N_{\beta} f_{Li} \beta_{con} \epsilon_c}{(N_d * 0.5)} \quad (4.20)$$

The value for β_{con} for ^8Li was calculated to be (1.04 ± 0.01) using the method outlined in section 4.3. The values of the other pertinent parameters are listed by run number in table 4.8.

The results of this calculation, and therefore the values of the ratio of detection efficiencies, are listed for detectors D1 and D2 in table 4.9.

Table 4.8: Values for parameters necessary to calculate the ratio of efficiencies, $\epsilon_\beta/\epsilon_d$, in the ${}^8\text{Li}$ calibration runs

Run	N_β	N_d (D1)	N_d (D2)
53	13478 ± 116	104228 ± 323	104227 ± 323
54	11314 ± 107	128262 ± 359	128264 ± 359
78	9079 ± 96	65172 ± 256	65169 ± 256
80	8433 ± 92	64795 ± 255	64792 ± 255
Run		ϵ_c (D1)	ϵ_c (D2)
53		0.429 ± 0.002	0.600 ± 0.003
54		0.445 ± 0.002	0.621 ± 0.003
78		0.362 ± 0.002	0.582 ± 0.003
80		0.386 ± 0.002	0.615 ± 0.003

Table 4.9: Ratio of detection efficiencies, $\epsilon_\beta/\epsilon_d$, for each particle detector and ${}^8\text{Li}$ calibration run

Calibration Run	$(\epsilon_\beta/\epsilon_d)$ D1	$(\epsilon_\beta/\epsilon_d)$ D2
53	0.108 ± 0.003	0.151 ± 0.005
54	0.072 ± 0.002	0.101 ± 0.003
78	0.095 ± 0.003	0.153 ± 0.006
80	0.097 ± 0.002	0.155 ± 0.006

Table 4.10: Summary of efficiency ratio calculation derived by the source calibration method

Run	Source	$\epsilon_\beta/\epsilon_d$ (D1)	$\epsilon_\beta/\epsilon_d$ (D2)
53	^8Li	(0.108 ± 0.006)	(0.151 ± 0.008)
54	^8Li	(0.072 ± 0.004)	(0.101 ± 0.005)
78	^8Li	(0.095 ± 0.005)	(0.153 ± 0.008)
80	^8Li	(0.097 ± 0.005)	(0.155 ± 0.008)
99	^{16}N	(0.078 ± 0.019)	(0.111 ± 0.028)
Weighted Mean		(0.088 ± 0.015)	(0.127 ± 0.026)
Arithmetic Mean		(0.088 ± 0.017)	(0.131 ± 0.029)

Sources Summary

Using the results of $\epsilon_\beta/\epsilon_d$ determined by ^{16}N and ^8Li , a weighted mean and standard deviation for the efficiency ratio by the sources method can be calculated for detectors D1 and D2. The result of this weighted average yields a detection efficiency ratio, $\epsilon_\beta/\epsilon_d$, of (0.088 ± 0.014) for detector D1 and a detection efficiency ratio, $\epsilon_\beta/\epsilon_d$, of (0.127 ± 0.026) for detector D2. The individual run results and weighted means for D1 and D2 are summarized in table 4.10.

4.6.3 Coincidence Efficiencies Method

The sources method of determining the efficiency ratio $\epsilon_\beta/\epsilon_d$ was established under experimental conditions equivalent to those of the ^6He runs. Because the conditions were the same, the values of $\epsilon_\beta/\epsilon_d$ by the sources method are considered more reliable than those calculated from the system geometry.

The large error and difference between the two values of $\epsilon_\beta/\epsilon_d$ as calculated by the geometric and sources methods for was the source of some concern. The uncertainty in the position of D1 with respect to the activity meant that the $\epsilon_\beta/\epsilon_d$ value for D1 calculated by the sources method was essentially unconfirmed. It was therefore desirable, if not quite critical, to calculate the $\epsilon_\beta/\epsilon_d$ for the detectors by some third,

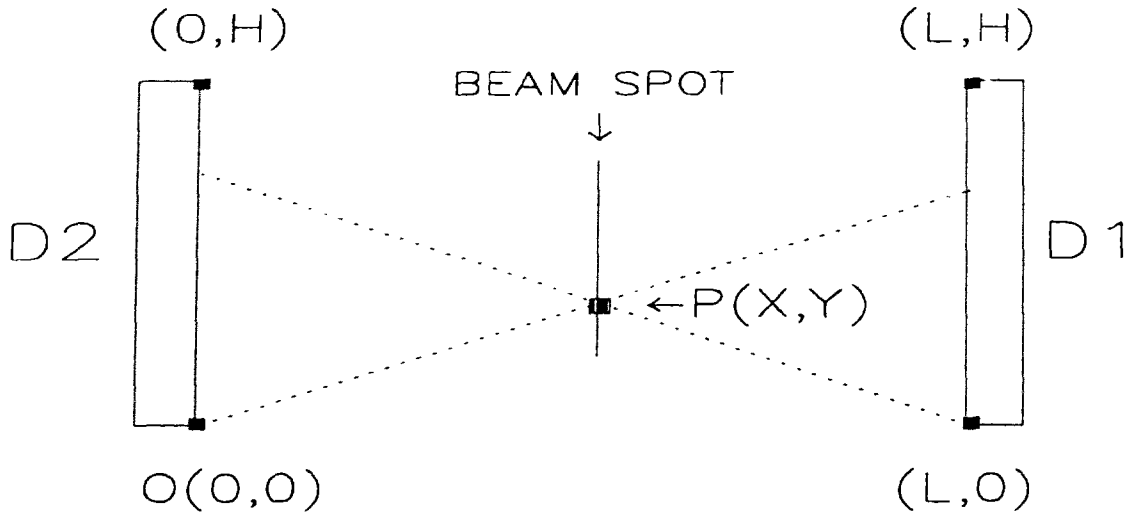


Figure 4.5: Singles and Coincidence geometries as a function of source and detector arrangement

independent method that did not rely on the measured geometric solid angle of D1.

The method chosen was to infer the detection efficiencies, ϵ_d , from the observed D1 and D2 coincidence efficiencies, ϵ_c . The coincidence efficiencies are run specific parameters that are dependent only on the experimental coincidence and singles geometries. The singles geometry is simply a function of the source and detector positions while the coincidence geometry is dependent on the relative positions of both particle detectors with respect to the source activity.

Figure 4.5 shows the local geometry pertinent to the singles and coincidence efficiencies of detectors D1 and D2.

On the surface, it appears that there are too many parameters (X, Y, L, H) within the overall geometric system to elucidate the value of ϵ_d for D1 and D2 based on the coincidence efficiencies alone. However, further inspection reveals that all of these parameters are either known or can be constrained within a finite range of possible values. Due to the fact that the $\epsilon_\beta/\epsilon_d$ values for D2 in the geometric and sources method are in close agreement, the value of parameter X can be set within a narrow range. The range itself is defined such that the detection or singles efficiency, ϵ_d for D2 spans the mean and error calculated using the geometric method.

Parameter H , which does not vary, is simply equivalent to the diameter of the

particle detectors D1 and D2. This parameter was set to the known detector diameters given in the specification sheet supplied by the manufacturer.

The parameter Y , which is related to the offset distance of the activity with respect to the axis of the detectors, can be set within a finite range defined by the dimensions of the collimator and the carbon foil. The maximum value for the offset distance for any single ${}^6\text{He}$ decay ($H/2-Y$) is equal to 4mm in this system.

The parameter with the largest uncertainty is the value of the inter detector distance, L . To be more accurate, the greatest uncertainty is the source to D1 distance, ($L-X$). This uncertainty is evidenced by the large error in the calculated value of the geometric solid angle in section 4.6.1. In fact, this parameter is the quantity of interest in this analysis.

Even with the high geometric uncertainty, a range of the possible values of L can be limited due to some of the fixed components of the detector set-up. From the known value of the separation distance between the two Aluminum sleeves housing D1 and D2, and the measured inset distance of the detector face from its casing, the value of L can be constrained to lie in the range ($9.5\text{mm} \leq L \leq 11.5\text{mm}$).

The most shaky assumption made within this analysis is to assume that the value of L is constant over all twelve data runs. If this is not true then the calculated value of the $(\alpha + d)$ branching ratio is worthless.

Having established that the relative position of D1 is not well known it may have been possible that the position of D1 shifted during the experiment. However, during this analysis it was discovered that, although the efficiencies were affected by the magnitude of the offset distance, Y , the *ratio* of the coincidence efficiencies ($\epsilon_c \text{ D2} / \epsilon_c \text{ D1}$) was largely *insensitive* to movement of the activity in this plane. As a result, the observed ratio of coincidence efficiencies can be utilized as a measure of the variation in L that took place as a function of time. Figure 4.6 shows a plot of the D2 coincidence efficiency against the D1 coincidence efficiency for all runs.

The line of best fit through these data has a slope of (1.3 ± 0.1) , which is, of course, equal to the mean $(\epsilon_c \text{ D2}) / (\epsilon_c \text{ D1})$ ratio. The fact that the data points fit well to a straight line indicates that the value of L over the course of the ${}^6\text{He}$ runs did not vary in a dramatic way. For example, if the detector separation distance, L , had

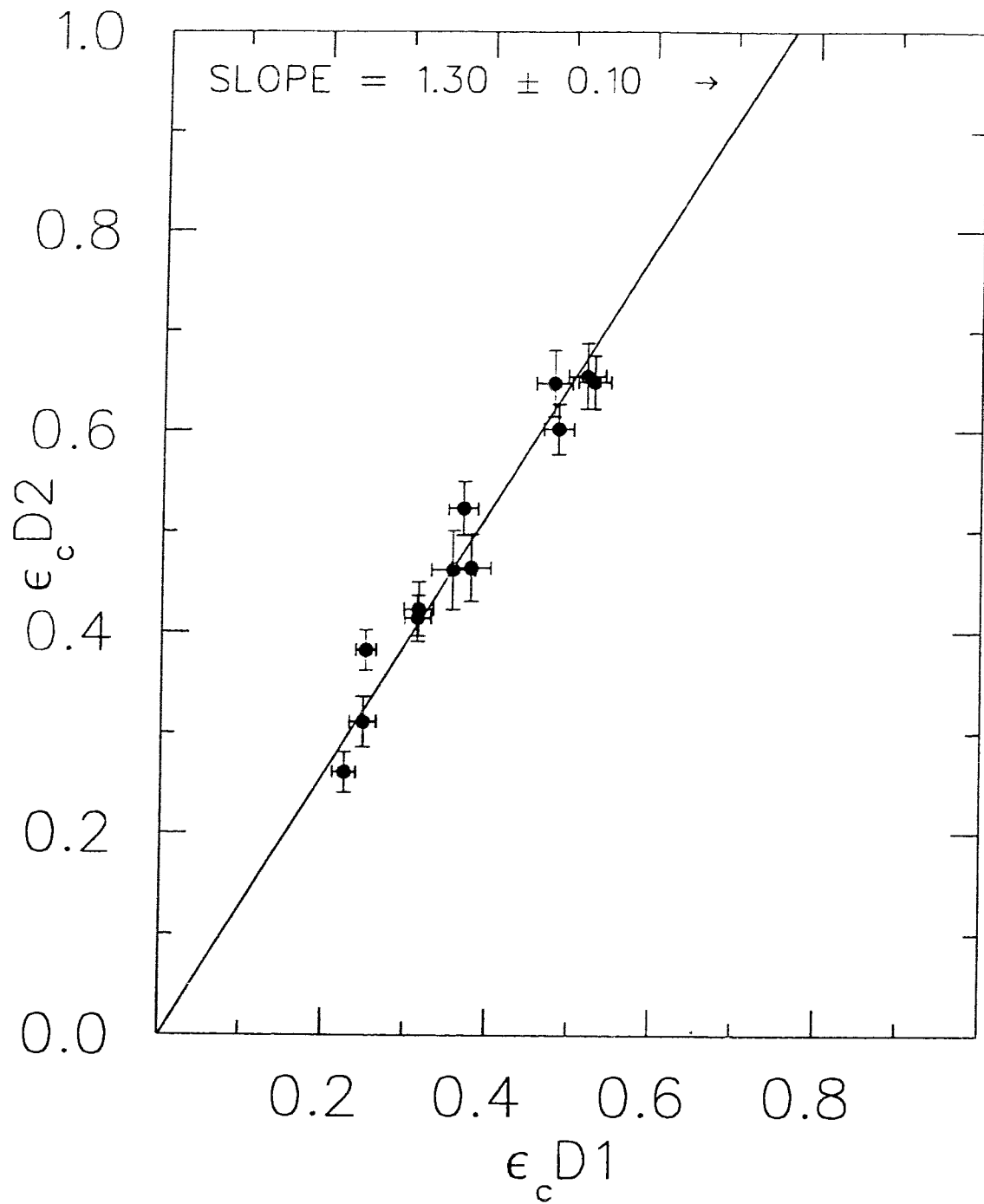


Figure 4.6: Observed relationship between the coincidence efficiencies of D1 and D2

varied by 1mm over time, the corresponding effect on the coincidence efficiency ratio at these close geometries would have been a change of over fifty percent. Since this is not observed, it would appear that the initial assumption of L being constant is a reasonable one. Furthermore, the variation in the coincidence efficiency ratio observed can be explained by variations in X and $(L-X)$ resulting from the uncertainty in the thickness of the Aluminum cards.

The first step, then was to allow L and X to vary until the calculated ϵ_c ratio agreed with experiment. Knowing L and X it is trivial to determine the source to D1 separation, $(L-X)$, and to calculate the detection efficiencies ϵ_d of D1 and D2 using equation 4.7.

However, figure 4.6 shows that the *individual* values of ϵ_c vary a great deal even though the *ratio* of the coincidence efficiencies is constant. To inspire confidence, the analytical method must also be able to reproduce the individual coincidence efficiencies within this geometry.

To do so it is important to remember two experimental details: first, that the source is not point like, and second, that the ion beam does not have a uniform cross section. The effect of the beam spot size is that for every run, ${}^6\text{He}$ decays take place at various points, Y , even though X and L are constant. To accommodate this, the singles and coincidence solid angles were calculated at various increments of Y for fixed L and X . Due to the non-uniformity of the radioactive beam, the activity within the beam spot as a function of Y is not constant. Therefore the various points in Y will not provide the same contribution to the singles and coincidence efficiencies of the overall system. To account for this, the efficiency values calculated at each point Y were weighted as a function of the activity. The functional form of the weighting of the points was assumed to be gaussian – that is, the activity at a point Y was decreased exponentially as a function of the linear distance away from the coaxial line of the detectors.

For fixed L and X , the singles and coincidence efficiencies calculated at the various Y increments were weighted as described above to determine the overall singles and coincidence efficiencies for each detector. By repeating this calculation and varying the position of the gaussian maximum within the allowed range of Y , it was possible

to reproduce the entire range of coincidence efficiencies observed for both detectors without affecting a change in L .

Having reproduced the individual coincidence efficiencies, the value for the ratio of detection efficiencies, $\epsilon_\beta/\epsilon_d$, determined from this method inspires more confidence. Taking the values of L and X that fit the observed coincidence efficiencies, the detection efficiencies, ϵ_d , were extracted for the system. The results indicated that the detection efficiencies for the particle detectors are (0.114 ± 0.018) for D1 and (0.085 ± 0.008) for D2.

The third independent method to determine the beta counting efficiency, ϵ_β , was to measure the relative number of beta/particle coincidence events to the number of singles particle events in detector D1 during one of the ${}^8\text{Li}$ runs. The ratio of the number of Germanium/D1 coincidences to the number of detected singles in D1 should be equal to the efficiency of the beta telescope. The result of this analysis indicated that the beta detection efficiency ϵ_β was equal to (0.0106 ± 0.001) .

Using the values of the particle detection efficiencies ϵ_d elucidated by the coincidence efficiency ratios and the beta detection efficiency ϵ_β as outlined above, the ratio of efficiencies, $\epsilon_\beta/\epsilon_d$, for detectors D1 and D2 are calculated to be (0.093 ± 0.017) and (0.125 ± 0.017) , respectively.

4.6.4 Efficiency Ratio Summary

The sources method for the determination of the ratio of efficiencies, $\epsilon_\beta/\epsilon_d$, is expected to be the most accurate and reliable due to the simple fact that this method is carried out under the experimental conditions used during the ${}^6\text{He}$ runs. This method, therefore, will incorporate all effects, including systematic, that might otherwise be transparent to the geometric and coincidence efficiency methods.

A significant difficulty within the sources method is that the $\epsilon_\beta/\epsilon_d$ values determined by the ${}^{16}\text{N}$ and ${}^8\text{Li}$ sources do not agree (see table 4.10). Analysis has demonstrated that the *range* of values for both the coincidence efficiency and the ratio of detection efficiencies can be explained by changes in the source/detector geometry due to variations in the position and dimensions of the activity distribution. However, the

analysis also shows that the sources with low coincidence efficiencies should have low particle detection efficiencies, ϵ_d . From this, one would predict that the sources with *low* coincidence efficiencies would have *high* values of the ratio of efficiencies, $\epsilon_\beta/\epsilon_d$.

Unfortunately, the calibration sources appear to invert this expected trend. The ^{16}N run, with the lowest observed coincidence efficiency would be expected to show the highest calculated value of $\epsilon_\beta/\epsilon_d$, however, the result is quite the opposite. Similarly, the ^8Li runs with high coincidence efficiencies lead to large values of $\epsilon_\beta/\epsilon_d$ when low values were expected.

Due to this ratio inversion, systematic differences between the calibration source runs and the ^6He runs were investigated. For ^{16}N , there were two notable changes from the ^6He experiments; first, a zeolite production target was used rather than graphite, and second, there was a gain change in the germanium, E, detector of the beta telescope.

The use of a different target material should not play a role in the data collection sequence unless contaminants in the beam were appreciable. Yield curves in this mass region recorded during TISOL development runs have shown that the ^{16}N beam is not heavily contaminated when a zeolite target is employed nor were beta backgrounds observed in the data analysis. What is more, even if the ^{16}N beam were contaminated, the effect would be to artificially increase the number of beta particles detected. A correction, if necessary, would result in the reduction of the calculated value of $\epsilon_\beta/\epsilon_d$ for this source. Thus, this effect can not explain the inversion of the expected results between the calibration sources.

The gain change in the germanium detector could alter the beta response ability of the beta telescope. This particular change made the germanium detector more sensitive to lower energy beta particle events. In light of this gain change, the value of β_{con} for ^{16}N was calculated on the basis of the energy cut-offs used in this run. Therefore, the increased sensitivity of the beta telescope should already have been accounted for in the $\epsilon_\beta/\epsilon_d$ calculation.

Another possible effect of the gain change could be to increase the number of false coincidences between the two components of the beta telescope due to a higher probability that noise would be registered in the Germanium detector. Once again, though,

the impact of such a perturbation would be to artificially increase the number of detected betas. This would suggest that the calculated value of $\epsilon_\beta/\epsilon_d$ is systematically too large. Therefore correcting for such an effect would, again, increase the disparity between the ^{16}N and ^8Li results for the ratio of detection efficiencies. This can not explain the discordant results.

The only systematic difference between the ^8Li and ^6He runs was that the prescaler used for beta particle counting in ^6He was removed for the ^8Li experiments. Investigation of the accuracy of the prescaler demonstrated that its value was equal to 100 to within one percent for all ^6He runs. It is therefore not believed that this change is at all responsible for the disparate results in the calculation of $\epsilon_\beta/\epsilon_d$.

Because there was no obvious reason to reject any of the calibration runs or either of the calibration sources, the branching ratio calculation was carried out using the average value of the observed efficiency ratio results [25].

4.7 Branching Ratio Results

Once again, the formula used to calculate the branching ratio of ^6He decaying to the unbound ($\alpha + d$) state is expressed as,

$$BR = \frac{N_d \epsilon_\beta}{N_\beta \beta_{con} \epsilon_d \epsilon_c} \quad (4.21)$$

The values of N_d , N_β , and ϵ_c are run dependent quantities and have been tabulated in the appropriate sections of this work. The values for the ratio of detection efficiencies $\epsilon_\beta/\epsilon_d$ utilized in the final calculation are those determined by the sources method of section 4.6.2. The results of the branching ratio calculation for the data collected in D1 and D2 are listed by run in table 4.11. For each particle detector, a weighted mean and standard deviation of the ($\alpha + d$) branching ratio was calculated. The individual run results were weighted as a function of their variance to determine the mean. The results of the weighted mean calculation for detectors D1 and D2 are shown graphically in figure 4.7 and figure 4.8, respectively.

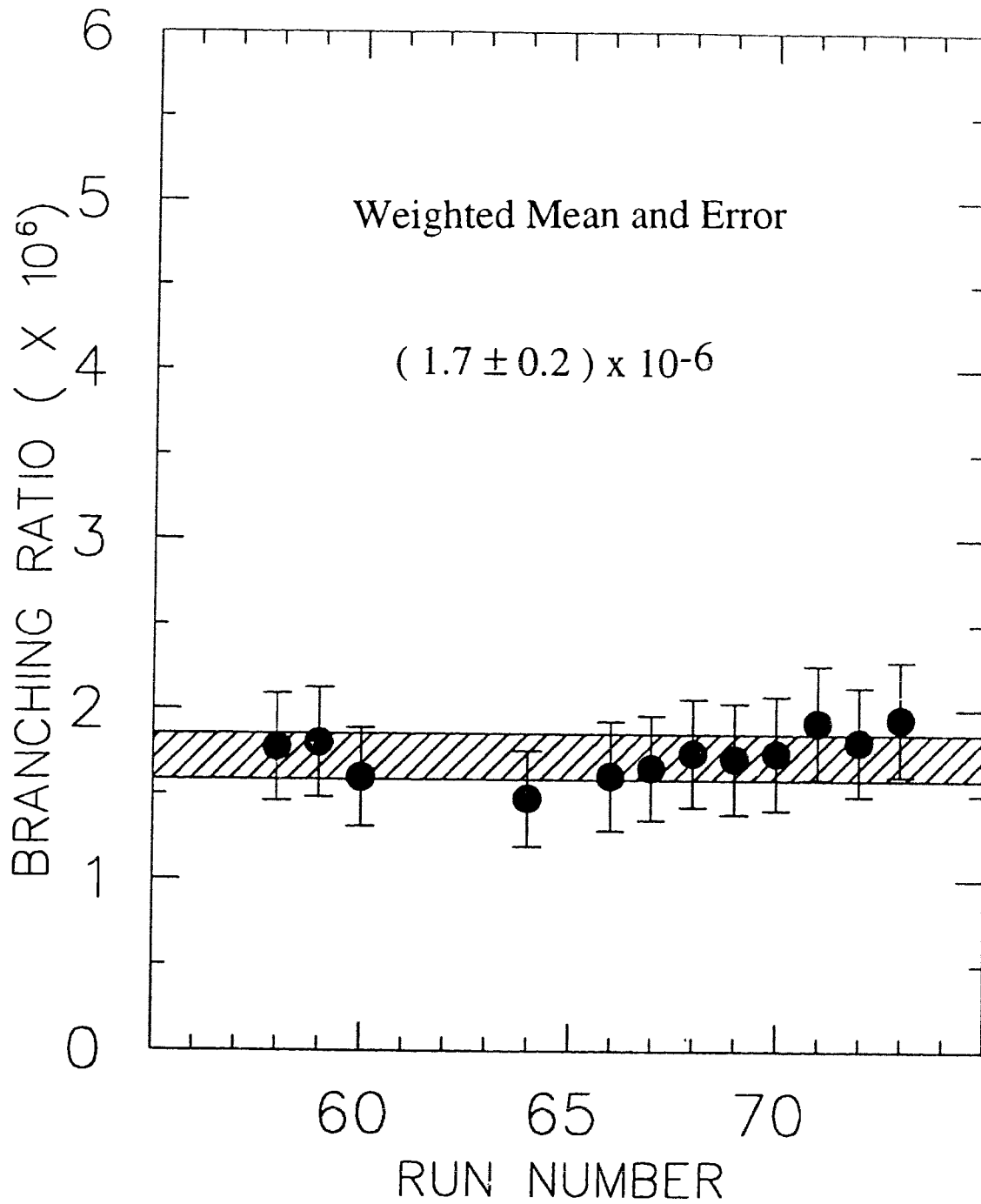


Figure 4.7: Branching Ratio results for the data collected in Detector D1

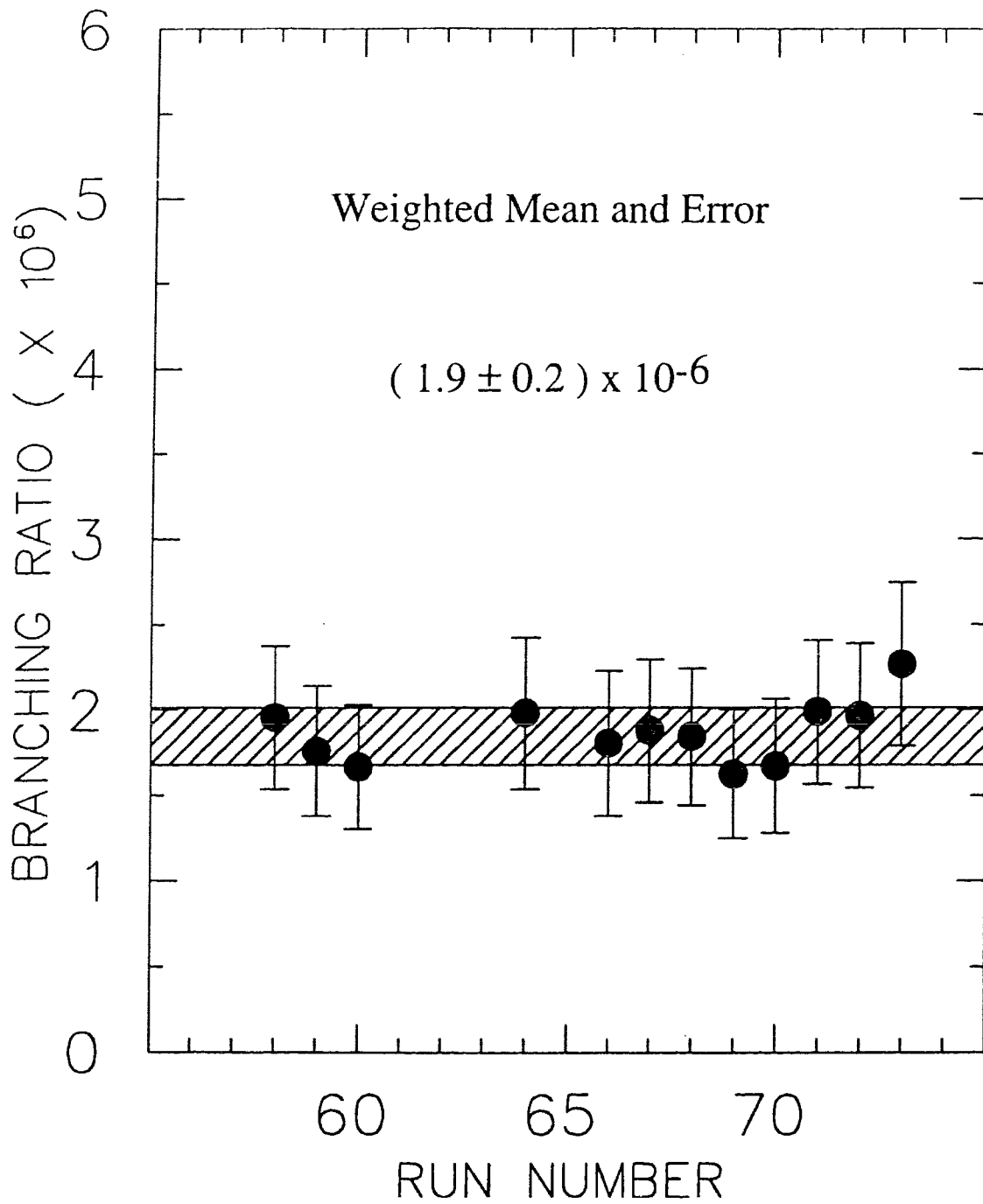


Figure 4.8: Branching Ratio results for the data collected in Detector D2

Table 4.11: Branching Ratio determinations for Detectors D1 and D2 as a function of ${}^6\text{He}$ run number

${}^6\text{He}$ Run	D1 Branching Ratio ($\times 10^6$)	D2 Branching Ratio ($\times 10^6$)
58	(1.8 ± 0.4)	(2.0 ± 0.5)
59	(1.8 ± 0.4)	(1.8 ± 0.4)
60	(1.6 ± 0.3)	(1.7 ± 0.4)
64	(1.5 ± 0.3)	(2.0 ± 0.5)
66	(1.6 ± 0.4)	(1.8 ± 0.5)
67	(1.7 ± 0.4)	(1.9 ± 0.5)
68	(1.8 ± 0.4)	(1.9 ± 0.5)
69	(1.7 ± 0.4)	(1.7 ± 0.4)
70	(1.8 ± 0.4)	(1.7 ± 0.4)
71	(1.9 ± 0.4)	(2.0 ± 0.5)
72	(1.8 ± 0.4)	(2.0 ± 0.5)
73	(2.0 ± 0.4)	(2.3 ± 0.5)

4.8 Systematic Errors

In addition to the counting or statistical errors in the branching ratio, there exist uncertainties in the result that are due to inherent errors of the experimental system. For this experiment, contributions to the systematic uncertainty are made by such items as the beta telescope energy cut-off, variations in the detection geometry, errors in detector calibrations and the possibility of random coincidences. Each of these are treated separately in the following sections.

4.8.1 Beta Cut-Off

The typical beta decay spectrum is a continuous curve beginning at zero energy and extending up to the full transition energy of the decay. Depending on the characteristics of the decay, the fraction of the overall spectrum that falls below a specific energy threshold will be different for different sources. In this experiment, a beta telescope was employed to detect the emitted beta particles. In order to register as

a true beta event, a signal had to be detected in both the ΔE and E components of the telescope. Low energy betas can not be detected in E and consequently were not counted as events. It was therefore necessary to estimate the fraction of beta particles not detected by the telescope for both the ${}^6\text{He}$ transition and the beta transitions of the calibration sources to determine the value of β_{con} .

These fractions were estimated by constructing theoretical beta decay spectra for the main decay branch in each of ${}^6\text{He}$ and the calibration sources. The variation between the shapes of the true beta spectra and the theoretical spectra as well as the error in the cut-off value due to uncertainties in the stopping power of the ΔE detector will be sources of some systematic error in the calculation of the branching ratio for deuteron emission.

Since the beta decays pertinent to this work were all either allowed or first forbidden, the theoretical spectra are not expected to be dramatically different from the true beta curves. Analysis of various beta sources revealed that the greatest variation from the predicted shapes occurs for forbidden transitions with large changes in angular momentum. Since these transitions, with one exception, do not exhibit large angular momentum changes, the error in the approximation is believed to be small.

A qualitative estimate of the maximum possible error due to the assumption that the theoretical and actual beta spectra are equivalent, combined with the error due to uncertainties in the energy cut-off, is about 18%. This then represents an uncertainty in the branching ratio of about $(\pm 0.4 * 10^{-6})$ for both detectors D1 and D2.

4.8.2 False Events

The approximate contribution of false or random coincidences to the number of detected deuterons, N_d , was estimated by monitoring coincidences occurring between one of D1 or D2 and detectors at stations (2) and (3). The geometry of the detector stations prohibits true coincidence events and is therefore a reasonable measure of the likelihood of random or false pairs. This analysis reveals that the the maximum level of random coincidences that could be expected was about three percent. Like the beta cut-off, this error works in only one direction. The impact of this uncertainty on

the calculated values of the branching ratio is about $(-0.1 * 10^{-6})$ for both D1 and D2.

4.8.3 Calibration Errors

The calculated uncertainty in the energy calibrations of detectors D1 and D2 lead to systematic errors in the branching ratio. The cut-off value for deuteron events was set at a laboratory energy of 350 keV. However, the true value of this cut-off is uncertain by approximately (35) keV for D1 and about (30) keV for D2.

Clearly, if the cut-off energy, assumed to be 350 from the calibration, is actually higher in energy, then the true $(\alpha + d)$ branching ratio is actually higher than what has been calculated. Similarly, if the 350 keV cut-off is actually lower in energy then the true branching ratio for deuteron events above 350 is lower than what has been measured.

Using the total deuteron spectra collected in D1 and D2, an estimate of the impact of this uncertainty on the branching ratio was made. The results indicate that the systematic error in the branching ratio due to the calibration error is about (8%) for D1 and about (7%) for D2. This leads to an uncertainty of about $(\pm 0.2 * 10^{-6})$ in the reported value.

4.8.4 Geometric Systematic Errors

A large contribution to the systematic error is made by potential variations in the source/detector geometry. An analysis similar to that outlined in section 4.6.3 which included varying such parameters as the detector to source separation, ion beam cross section, beam spot dimensions, beam spot position and coincidence geometry has indicated that these uncertainties contribute a systematic error to the calculated branching ratio of about 24% for D2 and about 28% for D1. Converting to break-up probability, this corresponds to an uncertainty of $(\pm 0.5 * 10^{-6})$ for D1 and D2.

Table 4.12: Summary of systematic effects leading to uncertainties in the $(\alpha + d)$ Branching Ratio

Source of Error	D1 ($\ast 10^6$)		D2 ($\ast 10^6$)	
	(+)	(-)	(+)	(-)
β cut-off	0.4	0.4	0.4	0.4
Randoms	0.0	0.1	0.0	0.1
Calibration	0.2	0.2	0.2	0.2
Geometry	0.5	0.5	0.5	0.5
Linearity	0.2	0.0	0.0	0.0

4.8.5 Detector Non-Linearity

In this experiment, particle detector D1 was an exceptionally thin silicon detector. The thickness of this device is reported by the manufacturer to be $10.6 \mu\text{m}$. Recent experimental evidence has indicated that the energy response of such a thin detector is not linear at low energies [28]. The data have shown that the calibrated energy response of a thin detector may underestimate the true particle energy by between 10 and 30 keV. The thicker D2 detector ($15.8 \mu\text{m}$) does not exhibit this non-linearity at low energies.

As a result of this linearity defect, the deuteron cut-off energy assumed to be 350 keV may actually be equivalent to 380 keV. Therefore, deuteron events with true energy between 350 and 380 keV are not included in the branching ratio calculation. An estimate of the magnitude of the systematic error caused by this uncertainty on the calculated value of the branching ratio has shown that the non-linearity could contribute an error of about (8%) percent. In terms of the branching ratio, an additional systematic uncertainty of $(+0.2 \ast 10^{-6})$ must be included but for detector D1 only.

4.8.6 Systematic Error Summary

The magnitude of the uncertainty in the $(\alpha + d)$ branching ratio made by each systematic effect may be found in table 4.12. From the individual contributions, an overall

Table 4.13: Final Branching Ratio results with statistical and systematic errors

Particle Detector	Branching Ratio	Statistical Error	Systematic		
			(+)	(-)	
D1	1.7	± 0.2	0.7	0.7	($\times 10^{-6}$)
D2	1.9	± 0.2	0.7	0.7	($\times 10^{-6}$)

systematic error for the branching ratio in D1 and D2 was calculated by adding the components in quadrature. The final values for the branching ratio of ${}^6\text{He}$ decaying through the $(\alpha + d)$ exit channel for each of detectors D1 and D2 are listed in table 4.13 with the statistical and systematic errors listed separately.

4.9 Branching Ratio Summary

The use of a telescope design for the detection of beta events has been the source of many difficulties in the determination of the ${}^6\text{He}$ branching ratio for deuteron emission. These difficulties have been compounded by the existence of a hardware coincidence between the two components of the device. The hardware coincidence makes it impossible to analyse for systematic effects such as backscattering and multiple scattering due to the fact that the ΔE and E responses can not be separated and analysed on an individual basis.

The telescope design itself results in the elimination of low energy beta events from the counting system due to the stopping power and beta energy loss governed by the ΔE component of the detector. To account for this effect, the β_{con} term was included in the branching ratio calculation. However, the value of β_{con} is extremely sensitive to the magnitude of the energy cut-off used, particularly for the ${}^6\text{He}$ beta spectrum. From the beta responses recorded in the ΔE detector, the magnitude of the mean beta particle energy loss was calculated and compared with that predicted by the theoretical approaches of Vavilov and Symon [26]. The two values were found not to be in close agreement although the recorded shape of the beta particles was consistent with that predicted by the above mentioned approximations. However, the

theory is probably not completely applicable in this instance. The requirements of the theoretical approaches are that the absorber thickness be very small (typically gaseous) and that the mean energy of the emitted beta particles be much larger than the stopping power of the absorber. In this case, the absorber (ΔE) is fairly thick ($500\mu\text{m}$) and certainly not gaseous. Furthermore, the mean emission energy of the ${}^6\text{He}$ and ${}^{16}\text{N}$ beta particles may not be sufficiently large to satisfy the second requirement. For these reasons, the beta energy loss value used for the calculation of β_{con} was taken as that observed in the ΔE detector rather than that predicted by theory.

The use of the germanium detector for the E component of the beta telescope becomes important with respect to backscattering. Electrons interacting with an absorber can be scattered such that the electron is reflected back out of the detector or deflected into the walls of the device. In either case, the full energy of the beta particle is not recorded by the detector and hence may not register as an event. The probability of such backscattering occurring is a function of the nuclear charge of the absorbing material. Germanium, having a fairly large Z value might be expected to scatter incoming electrons to a high degree. However, the probability of scattering also decreases exponentially with the kinetic energy of the electron [26]. In this case, then, the germanium detector threshold is helpful as low energy electrons are removed from the system. Because of this, differences between the scattering effects for the calibration sources and the ${}^6\text{He}$ runs are believed to be minimized.

In this work, corrections for backscattering effects have not been made nor has a systematic error been approximated along the lines of those reported in section 4.8. The reason being that such calculations are neither straightforward nor reliable. Furthermore, even if such a calculation were made, it would not be clear how to resolve the value of β_{con} with the backscattered correction. One would be in danger of 'double counting' (or in this case, doubly subtracting) beta particles as the two corrections are most sensitive to betas of low kinetic energy. However, the reader should be cognizant of the fact that the reported branching ratio may be sensitive to systematic effects not explicitly accounted for within the analysis.

In the experimental design, detector D8 was used to facilitate beta counting independent of the telescope device. Unfortunately, numerous notations in the experimental run book coupled with obviously inconsistent results upon analysis have demonstrated that the detector designated D8 was functionally useless. The loss of this beta recording device means that the only source of beta timing and energy information is the beta telescope.

The only other possible measures of the beta activity were the scalers which provided a count of events detected in the ΔE and E components of the telescope. There is no energy or timing information associated with these events and hence the scalers can not be software analysed for cut-offs or other systematic effects. Even under the limited conditions of scaler counting, several difficulties have been encountered. The CAMAC system read and cleared the scalers every five seconds during the experimental runs. During the experiments, the data recording computer was disabled from time to time when the cyclotron was down or when changes were made to the on-line analysis program. From a plot of the scaler values as a function of time, it became clear that though the scalers were not *read* when the data acquisition system was disabled they were still being *incremented* with time. When the computer was restarted, the cumulative value of the scaler was read after the first cycle – thereby including in the total, events occurring while the system was off.

A second difficulty with using the scalers as a measure of the beta activity is that, for the ${}^8\text{Li}$ runs, a significant fraction of alpha particles break through detector D1. Those that break through can be detected as events by the ΔE detector and hence some of the scaler count in ΔE will not be due to beta particles at all but to alphas. This would obscure the determination of the counting efficiencies by the sources method and render the approach inherently unreliable. Because of these problems, an analysis of the branching ratio based on scaler responses as a method for beta counting was not seriously pursued.

The results generated in this chapter for the probability of deuteron emission from ${}^6\text{He}$ are the most reliable values that can be determined from the data collected in this experiment. Due to the energy non-linearity of detector D1, the final Branching Ratio is reported as that determined using detector D2. The final Branching Ratio is

then $(1.9 \pm 0.2 \pm 0.7) * 10^{-6}$.

Comparing this result to the previously published experimental determinations, the new value for the branching ratio is not in agreement with the Borge result of $(7.6 \pm 0.6) * 10^{-6}$ which is the current accepted value for this decay probability. However, on comparison with the original publication of Riisager's group, the two values agree, within error, when differences in the experimental cut-off energy are taken into account.

Chapter 5

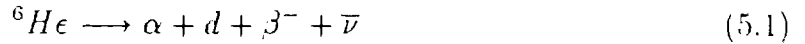
K-Matrix Analysis

5.1 General

One major shortfall of the experimental data is that the particle energy spectra do not span the entire energy range open to the reaction channel. The deuteron and alpha spectra are contaminated at low energies by beta noise and are further held hostage by the inherent limitations of the detection devices below a certain energy threshold. However, since the high energy regions of the spectra generated by experiment are basically background free and of reasonably high statistics, it is possible to generate a theoretical spectrum over the entire energy range. This is accomplished by fitting the observed particle spectra with a theoretical form and extending the theoretical spectrum down to zero energy.

The energy spectra of the emitted alphas and deuterons were fit using what is known as K-Matrix reaction theory [29] [30] [28]. In broad terms, K-Matrix theory allows for a nuclear reaction to be separated into two regions; an external region that is generally well known and an internal region that is largely unknown. The principal strength of K-Matrix theory is that the unknown internal region can be expressed in terms of an array of reaction parameters. Each of these parameters plays a role in defining the observable quantities of the external region. Therefore, since the external region is well known, the parameters may be selected and varied as necessary to match the observables in the external region.

Before broaching the K-Matrix theory formalism, it would be useful to revisit the mass ($A=6$) level structure and attempt to understand the overall decay process,

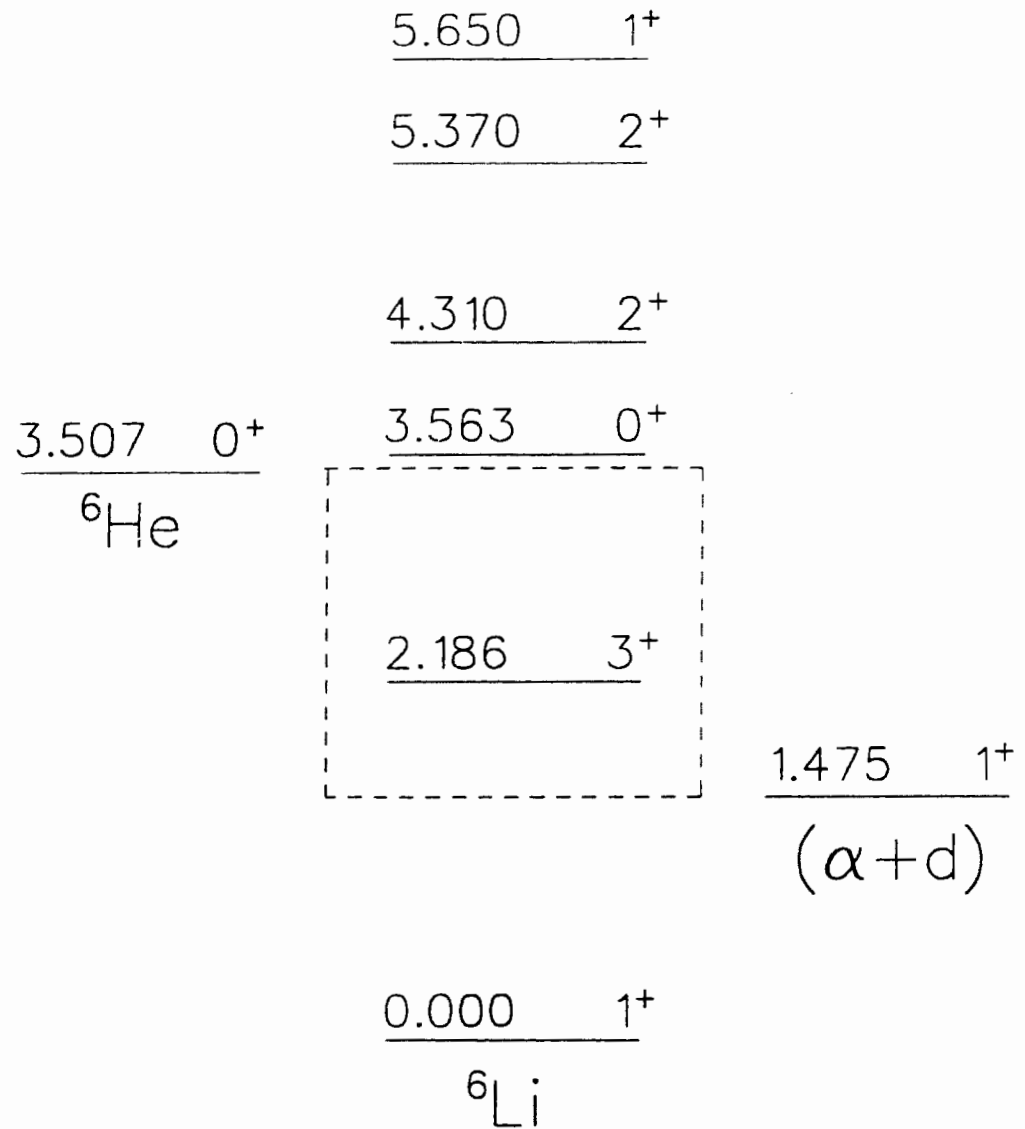


In order to achieve the $(\alpha + d)$ final state, the initial beta decay must pass through one of the ${}^6\text{Li}$ levels. Clearly, the initial beta decay must populate a well defined and finite energy region within the ${}^6\text{Li}$ nucleus in order for the unbound $(\alpha + d)$ state to be accessible. Beta decay to a point in the ${}^6\text{Li}$ nucleus below the 1.475 MeV $(\alpha + d)$ level can not result in the subsequent break-up. Furthermore, beta decay from the ${}^6\text{He}$ nuclide can not populate a point in the ${}^6\text{Li}$ nucleus that is higher in energy than the ${}^6\text{He}$ ground state. The energy region open to the initial ${}^6\text{He}$ beta decay that might lead to an $(\alpha + d)$ break-up is shown in figure 5.1.

To emit a deuteron with kinetic energy, E , in the centre of mass, the initial beta decay of ${}^6\text{He}$ must populate a point in the ${}^6\text{Li}$ level scheme at an energy, E , above the $(\alpha + d)$ state. The probability of so populating the point, E , via beta decay is controlled by the so-called fermi integral, $F(W, Z)$. The fermi integral is a function of the transition energy, W (measured in electron masses), and the atomic number of the beta decay daughter. Because every $(\alpha + d)$ break-up is initiated by a beta transition it is expected that any reasonable theoretical description of the overall ${}^6\text{He}$ decay process will include a fermi integral in its formalism.

Once the point, E , in ${}^6\text{Li}$ has been fed by the weak force moderated beta decay, the probability of the final $(\alpha + d)$ state being populated is related to the likelihood that the virtual alpha and deuteron will break-up via the strong force. The probability of such a break-up will be a function of the deuteron's ability to penetrate the coulomb barrier of ${}^6\text{Li}$ forming the unbound $(\alpha + d)$ state. It is therefore expected that a theoretical approximation of this exotic decay will include a term involving the deuteron and alpha penetrabilities as a function of decay energy, E .

It is noteworthy that these two probabilities, the fermi probability and the penetration probability, will work in opposition to one another. It is expected that in order for a deuteron (or alpha) to have a high penetration probability, the magnitude of the excitation energy, E , above the $(\alpha + d)$ state must be large. However, a high value of

Figure 5.1: Energy region available for $(\alpha + d)$ break-up

E means that the available beta decay energy to this point will be low. Hence, the fermi probability of a beta transition populating a point at this energy will be small. Conversely, a large fermi probability would populate an energy point E very close to the $(\alpha + d)$ threshold, rendering the probability of the alpha or deuteron penetrating the coulomb barrier to be small.

It is also noteworthy that, based on the energy level diagram of figure 5.1, there is only one state in ${}^6\text{Li}$, the $3+$ state at (2.186) MeV, within the energy region open to deuteron emission. The properties of this state are well known with the published deuteron width of this state being about 24 keV [8]. However, the experimental results have shown that the widths of the alpha and deuteron spectra are well over 1 MeV. These two facts are not compatible, at least superficially. It should therefore also be expected that some component or term in the theoretical approach will resolve the apparent incompatibility of the level widths and the energy span of the emitted alphas and deuterons.

5.2 K-Matrix Theory

Consider the existence of the intermediate compound nucleus ${}^8\text{Be}^*$. This species may be produced via a multitude of entrance channels including $({}^7\text{Li} + p)$, and $({}^6\text{Li} + d)$. It can decay via many exit channels including $({}^4\text{He} + {}^4\text{He})$ and $({}^7\text{Be} + n)$ [8]. The probability of a particular exit channel being utilized as a function of entrance channel and interaction energy can usually be measured by experiment. These probabilities are termed reaction cross sections labelled as:

$$\sigma_{i \rightarrow f}(E) \tag{5.2}$$

where i is the initial or entrance channel, f is the final or exit channel, and E signifies that the reaction cross section is dependent on the interaction energy of the reactants. Though it is important to know the reaction cross sections as a function of energy, these probabilities do not illuminate the nuclear reaction mechanism. It is at this point where nuclear reaction theories such as K-Matrix theory become useful.

The principal idea behind the nuclear reaction models is that the observed reaction

cross sections must depend on the properties of the initial, final, and intermediate states involved in the overall reaction process. The central goal of the models is to establish a set of nuclear parameters that describe and are consistent with the observed experimental results.

The main feature of the reaction theories is the so-called transition matrix, \mathbf{T} . The transition matrix is related to the cross section by the equation:

$$\sigma_{c \rightarrow d}(E) \propto T_{dc}^2(E) \quad (5.3)$$

where T_{dc} is an element of the transition matrix \mathbf{T} . The element $T_{dc}(E)$ defines the amplitude of the outgoing waves in exit channel, d , as a function of the incoming waves of entrance channel, c , and interaction energy, E . Of course, this still doesn't illuminate any of the properties of the intermediate, initial, or final states. However, the transition matrix, \mathbf{T} , can be rewritten as

$$\mathbf{T} = 2i\mathbf{p}\mathbf{K}(\mathbf{1} + i\mathbf{u}\mathbf{K})^{-1}\mathbf{p} \quad (5.4)$$

where \mathbf{p} and \mathbf{u} are diagonal matrices, $\mathbf{1}$ is the unit matrix and \mathbf{K} is the so-called generalized, symmetric collision matrix, or K-Matrix. Here, the elements of \mathbf{p} , \mathbf{u} and \mathbf{K} depend explicitly on the properties of the initial, final and intermediate states involved in the reaction.

The beauty of the theory is that the values of the nuclear parameters within \mathbf{p} , \mathbf{u} , and \mathbf{K} can either be calculated from first principles or be inferred from the experimentally observed cross sections. Once known, these parameters provide an extremely powerful tool to estimate reaction cross sections at energies not feasible in the laboratory. Such calculations are of primary importance in the discipline of nuclear astrophysics where reactions occurring at stellar energies involving species of limited stability can not be replicated experimentally.

For the purposes of this study, it turned out that the interaction cross section as a function of energy was not particularly important. What was of interest though were the shapes of the deuteron and alpha particle energy spectra. Fortunately, within K-Matrix theory, it is possible to generate a theoretical approximation of the total deuteron and alpha spectra. This was accomplished by selecting the components of

K-Matrix theory pertinent to spectrum shapes and fitting the high energy part of the observed spectra to the theoretical form.

5.2.1 Theoretical Fitting Terms

It is important to understand what the experimentally determined particle energy spectra really are. They show the number of deuteron or alpha events emitted by ${}^6\text{He}$ as a function of energy over a given time period. Since the time frame for each energy bin was the same, the spectra are essentially measurements of the deuteron or alpha emission probability as a function of energy.

Within K-Matrix theory it is possible to determine the probability of emitting an alpha or a deuteron with kinetic energy, E , from the matrix elements of the \mathbf{K} and \mathbf{p} matrices. The elements, p_c of matrix p are defined by the equation,

$$p_c = \epsilon_\ell k_c^{\ell+1/2} \quad (5.5)$$

where k_c is the wave number of the transition given by:

$$k_c = (2\mu E)^{1/2}/\hbar \quad (5.6)$$

with μ being the reduced mass of the $(\alpha + d)$ system, and E the energy of the emitted alpha or deuteron in the centre of mass.

The subscript ℓ refers to the angular momentum change between the entrance and exit channel of the transition, and the term ϵ_ℓ is defined by the equation:

$$\epsilon_\ell(\eta_c) = \eta_c^\ell U_\ell(\eta_c)^{1/2} C_o(\eta_c)/(\ell!) \quad (5.7)$$

where η_c is the Sommerfeld parameter given by,

$$\eta_c(E) = 0.1575 * Z_1 Z_2 \sqrt{\mu/E} \quad (5.8)$$

and the C_o term is found from,

$$C_o(\eta_c) = [2\pi\eta_c/e^{2\pi\eta_c} - 1]^{1/2} \quad (5.9)$$

and the term U_ℓ is defined recursively with,

$$U_0 = 1 \quad U_\ell = (1 + \ell^2 \eta_c^{-2})U_{\ell-1} \quad (5.10)$$

The elements p_c of matrix p have a finite value for each emission energy, E , and for each intermediate state populated by the fermi decay. These p_c terms are referred to as K-Matrix penetrabilities and are completely analogous with the penetrabilities discussed in section 5.1.

The elements of the matrix \mathbf{K} are found from the equation:

$$K_{\ell\lambda} = \sum_{\lambda=1}^{q\ell} \frac{g_{\ell\alpha\lambda}^2}{E_{\ell\lambda} - E} + D_{\ell\alpha} \quad (5.11)$$

where, once again, the ℓ subscript refers to the angular momentum change previously defined, the $E_{\ell\lambda}$ refer to the centre of mass energy of the intermediate state with respect to the $(\alpha + d)$ state, the E refers to the deuteron emission energy, the $g_{\ell\alpha\lambda}$ term is the reduced width of the intermediate state, and the $D_{\ell\alpha}$ term is simply a background term in the equation.

The summation indicates that the K-Matrix element for angular momentum change ℓ must be the sum of the contributions made by all possible intermediate states giving angular momentum change ℓ , regardless of their relative energies.

It is important to note that the term g , the reduced width, solves the problem mentioned in section 5.1 where the width of the $3+$ state in ${}^6\text{Li}$ did not agree with the observed width of the particle energy spectra. Even though the true width of a state may be narrow, the reduced or virtual width can be large. However, the fact that virtual widths may be large adds a complication to the ${}^6\text{Li}$ system. In the analysis it must be considered that with sufficiently large widths, states outside the available energy region of figure 5.1 may play a role in the ${}^6\text{He}$ decay. This is particularly important for the ${}^6\text{Li}$ ground state as this state is expected to be important for reasons that will be discussed later.

5.2.2 Theoretical Transition Probability

Knowing the functional form of the K-Matrix elements and the penetrabilities as a function of energy, the probability of emitting a deuteron or alpha with kinetic energy,

E , in the centre of mass can be calculated from the formula,

$$W_{\ell\alpha}(E) = f_{\beta}(E)p_{\ell\alpha}^2(E) * \frac{|\sum_{\lambda=1}^{q\ell} \frac{B_{\ell\lambda}g_{\ell\alpha\lambda}}{E_{\ell\lambda}-E} + D_{\ell\alpha}|^2}{1 + p_{\ell\alpha}^4 K_{\ell\alpha}^2} \quad (5.12)$$

In this equation the subscript α indicates that the overall transition of interest is the $(\alpha + d)$ break-up of ${}^6\text{He}$ and the subscript ℓ has the same significance as in equation 5.5. The subscript λ in the summation term signifies the λ^{th} state with angular momentum change ℓ included in the decay process. The f_{β} factor is the integrated fermi function

$$f_{\beta} = F(W_0, Z) \quad (5.13)$$

which is a measure of the phase space available to the beta particle and neutrino as a function of energy [28]. The W_0 parameter is measured in electron masses and can be solved from the equation,

$$W_0 = Q_{\beta} + m_e - E/m_e \quad (5.14)$$

where Q_{β} is the energy between the ${}^6\text{He}$ ground state and the unbound $(\alpha + d)$ state, m_e is the electron mass in MeV and E is the energy of the emitted particle in the centre of mass frame.

The $B_{\ell\lambda}$ term in equation 5.12 is the beta feeding factor. It is a measure of the likelihood that a beta decay will populate a certain intermediate state in ${}^6\text{Li}$ and, once again, the $D_{\ell\alpha}$ term is a background term to account for the contributions made to the process due to the low energy tails of the ${}^6\text{Li}$ continuum.

As a first order approximation, two assumptions were made: first, the background term in the equation was set to zero and, second, It was assumed that the only intermediate state involved was the virtual high-energy tail of the ${}^6\text{Li}$ ground state. The reason for the second assumption is that it has been shown that the ${}^6\text{Li}$ ground state wave function is more than ninety percent alpha/deuteron in character. This, coupled with the fact that a beta transition probability of feeding the ${}^6\text{Li}$ ground state is much greater than feeding the first excited $3+$ state suggests that the $1+$ ground state is much more likely to be involved in the decay mechanism than the higher energy states.

With these assumptions, the transition probability equation written in 5.12 can be simplified to:

$$W_{0\alpha}(E) = f_{\beta}(E)p_{0\alpha}^2(E) * \frac{\left|\frac{B_0 g_{0\alpha}}{E_{0\lambda} - E}\right|^2}{1 + p_{0\alpha}^4(E)K_{0\alpha}^2(E)} \quad (5.15)$$

Here, the value of E , the energy of the ground state ${}^6\text{Li}$ level relative to the $(\alpha + d)$ state is a constant known to be (-1.475 MeV). The f_{β} , p , and K terms can be calculated for each emission energy, E , in the centre of mass. The terms B_0 and g_0 are unknown constants, and, in fact, it is these two parameters that are of interest. These two terms will be two of the parameters allowed to vary freely in the overall fit to reproduce the spectra collected experimentally.

In section 3.6, two sets of spectra were generated for each of the alpha and deuteron spectra collected in detectors D1 and D2. The first set (figure 3.17) gives the event spectra with the beta background included while the second set (figures 3.16,3.18) give the event spectra with the functional form of the beta background subtracted off. For the K-Matrix fit, it was decided to complete the fit with the background features included. The reason for so doing was that there is a considerable degree of uncertainty in the subtraction approximations. Therefore, within the K-Matrix fit, a background term was embedded, with the functional form of the background being:

$$N_{\beta} = N_{\beta}^{\circ} \exp(-mE) \quad (5.16)$$

The terms N_{β}° and m were allowed to vary freely. By including the beta function in the fitting procedure, it was possible to monitor the dependence of the fit on the beta background contribution.

To summarize, the experimental deuteron and alpha spectra were fit (as a function of particle emission energy) by varying four parameters, B_0 , g_0 , N_{β}° , and m . The program MINUIT [31] was used to minimize the overall error in the fit – yielding a final set of fitted parameter values with their calculated uncertainties.

The quantity minimized by the MINUIT program is the overall χ^2 statistic. The χ^2 of the fit may be written [28],

$$\chi_{fit}^2 = \sum_{i=1}^{\infty} \chi_i^2 \quad (5.17)$$

Table 5.1: K-Matrix fit results to pertinent particle energy spectra

SPECTRUM	g_0	B_0	N_β^0	m
D2 Deuterons	0.0326 ± 0.0064	93 ± 18	$(7.7 \pm 0.8) * 10^7$	39 ± 2
D2 Alphas	0.0413 ± 0.0077	67 ± 12	74 ± 18	2.9 ± 0.4
D1 Alphas	0.488 ± 0.080	6 ± 1	$(1 \pm 0.5) * 10^4$	15 ± 2

where the summation is over the calculated χ^2 value of each floating parameter. For any set of parameters, the calculated value of χ^2 may be found from,

$$\chi_{fit}^2 = \sum_{i=1}^{\infty} \left(\frac{Y_i^{exp}(E_i) - Y_i^{calc}(E_i)}{\delta Y_i(E_i)} \right)^2 \quad (5.18)$$

where Y_i^{exp} and Y_i^{calc} are the experimental and calculated values, and δY_i is the experimental uncertainty in Y_i^{exp} .

MINUIT varies the selected parameters and recalculates Y_i^{calc} until the χ^2 statistic reaches a minimum. At this point the best fit to the experimental data has been achieved. By altering the initial values of the input parameters prior to running the MINUIT program it was possible to ensure that the true χ^2 minimum was reached rather than a local minimum.

5.3 K-Matrix Fit Results

K-matrix fits were performed on the alpha spectra in D1 and D2 and on the Deuteron spectrum of D2. The shape of the deuteron spectrum collected in D1 is not consistent with the true spectrum shape due to the fact that the thickness of D1 was not sufficient to stop high energy deuterons. As such, a K-Matrix fit to this spectrum would be meaningless.

The result of the K-Matrix fit to the D2 deuteron spectrum is shown in figure 5.2 while the fits to the alpha spectra in D2 and D1 are found in figure 5.3 and figure 5.4, respectively. Table 5.1 summarizes the best fit values calculated within the MINUIT routine for the four variable parameters outlined in section 5.2.2.

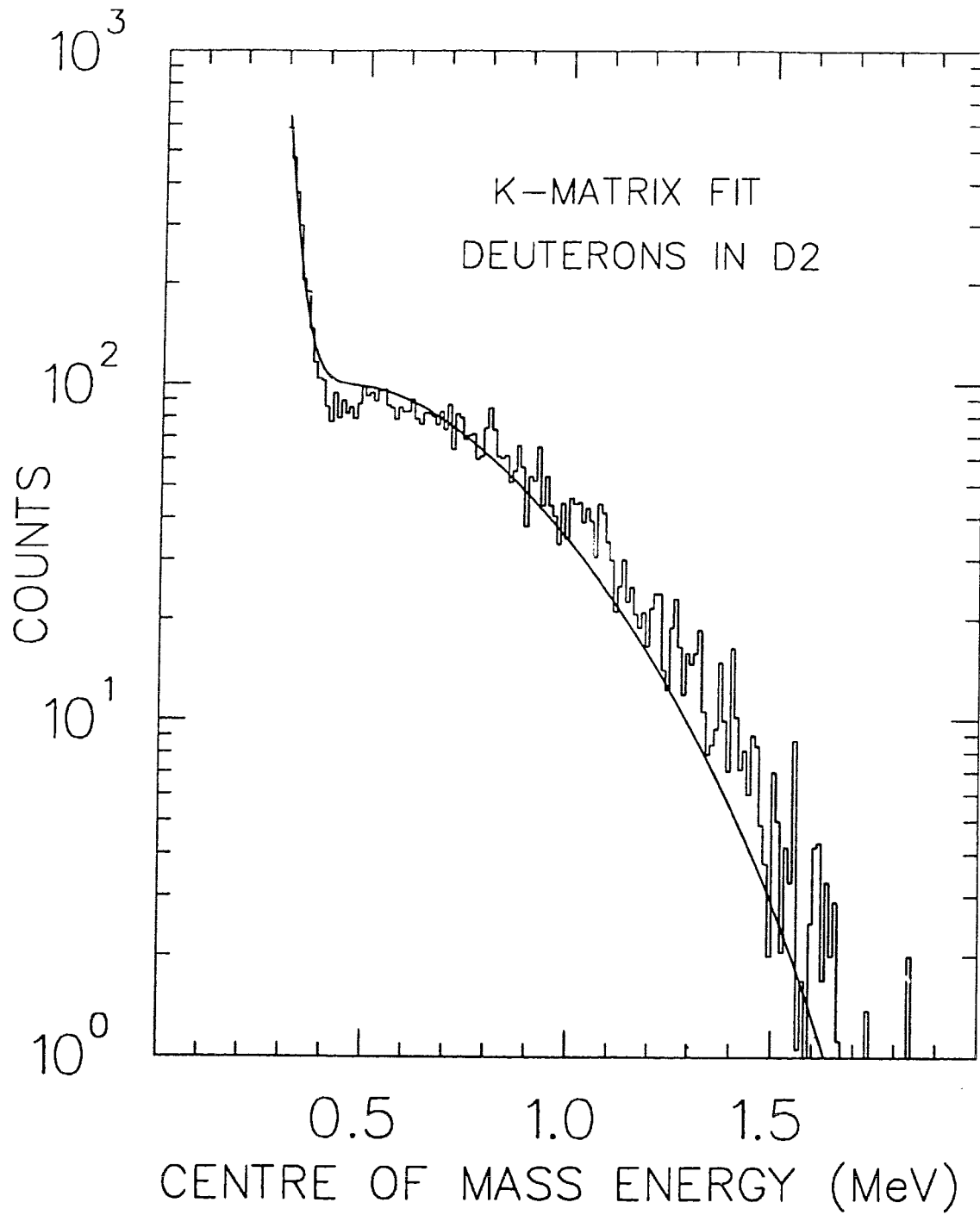


Figure 5.2: K-Matrix fit to deuteron spectrum collected in detector D2

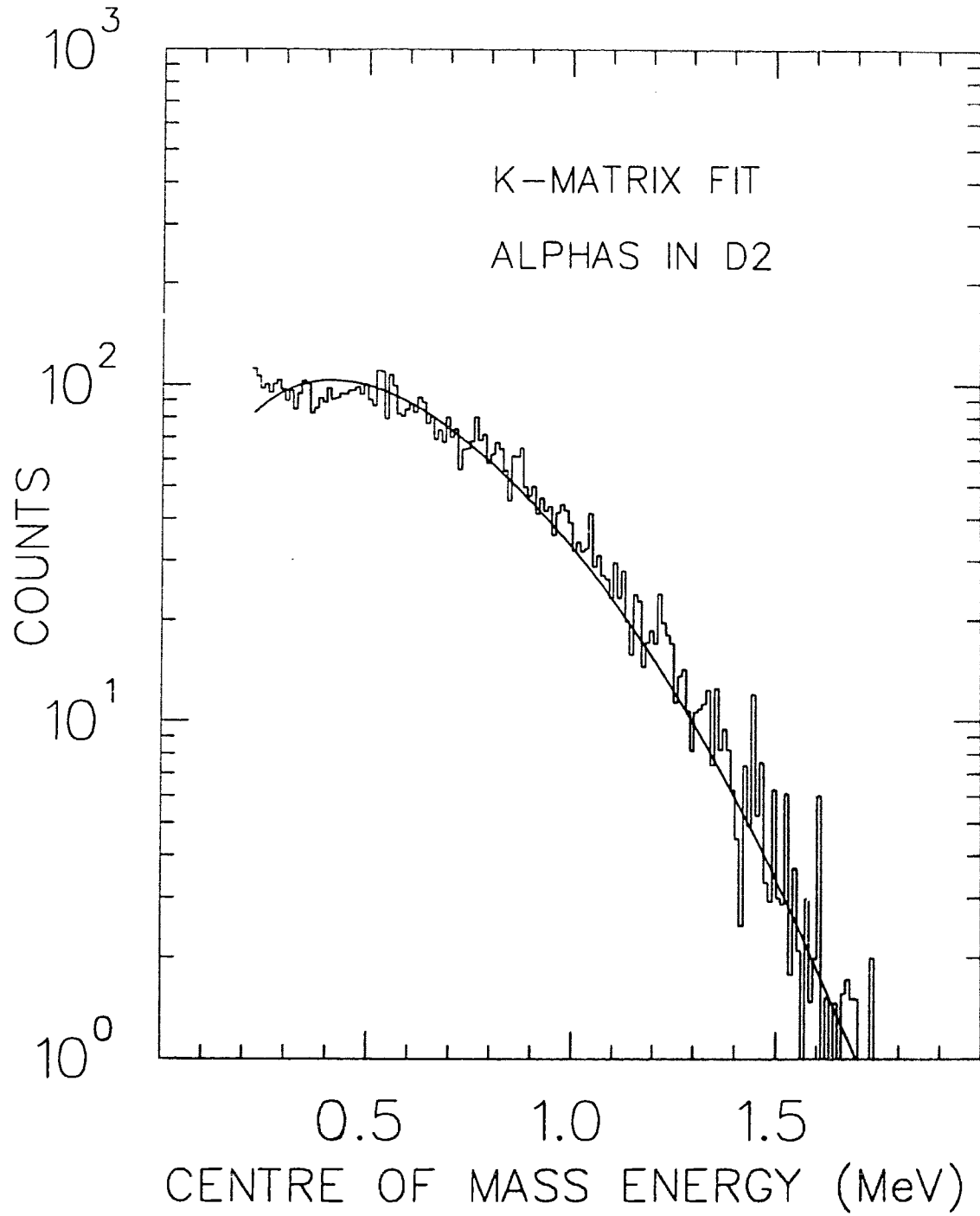


Figure 5.3: K-Matrix fit to alpha spectrum collected in detector D2

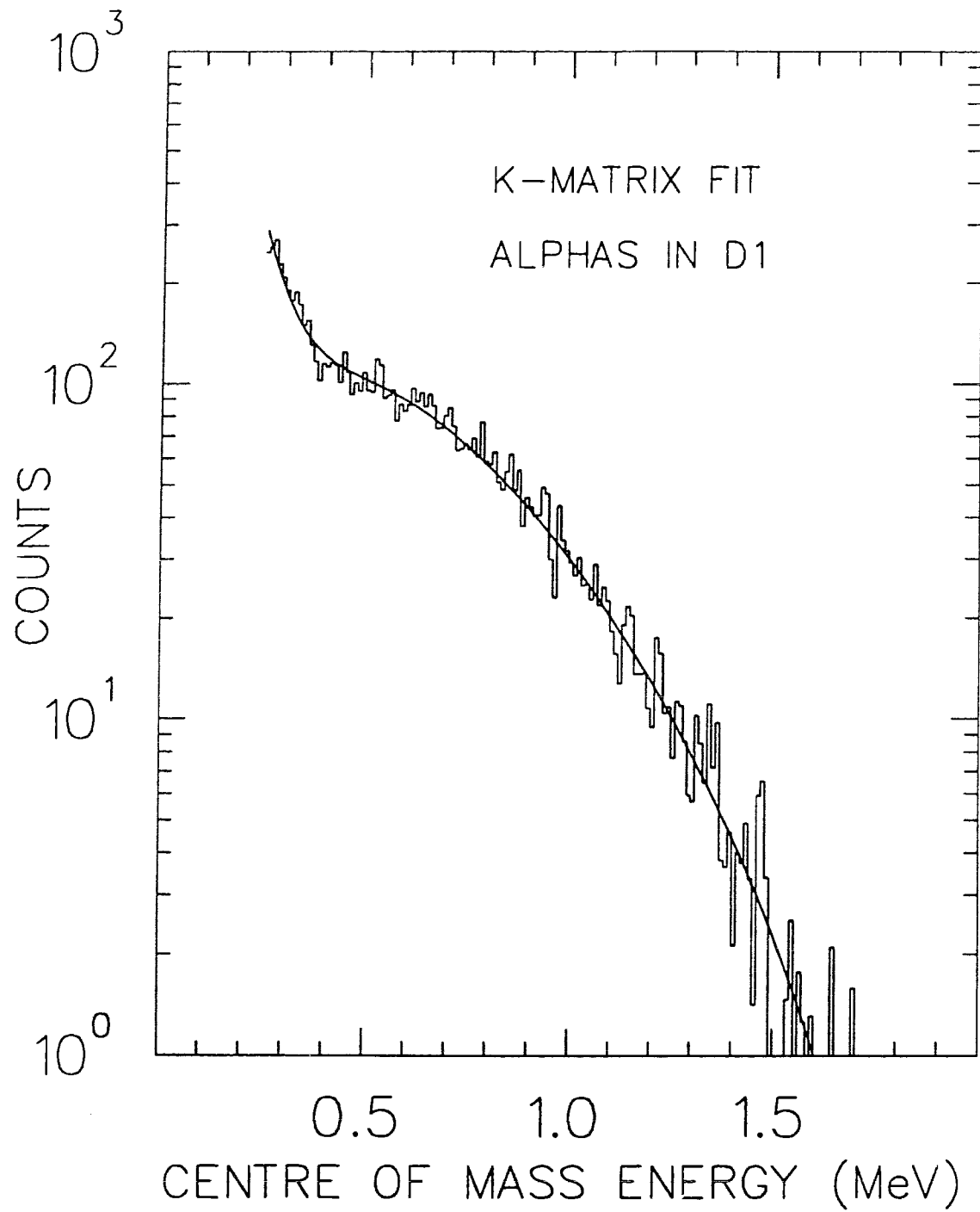


Figure 5.4: K-Matrix fit to alpha spectrum collected in detector D1

The best fit values of nuclear parameters B_0 and g_0 were found to agree within error for the alpha and deuteron spectra collected in D2. The discrepancy between the results for D1 and D2 is believed to be due to systematic difficulties evidenced in detector D1 – namely, that the energy calibration for D1 is highly uncertain at low energies due to the non-linearity of the detector's response in this region. Because of these systematic problems inherent to D1, the shapes of the spectra collected in D2 are considered to be of higher reliability.

5.4 Total Integrated ($\alpha + d$) Branching Ratio

The goal of the K-Matrix section of this work was to estimate the magnitude of the total ($\alpha + d$) decay probability. This has been accomplished by extracting the best fit values of the nuclear parameters B_0 and g_0 from the theoretical spectra and extending the calculated emission probability $W(E)$ down to zero energy.

The parameters B_0 and g_0 from MINUIT were fixed at their best fit values and inserted into equation 5.15. The fermi integral, penetrabilities and K-Matrix elements were then calculated for all emission energies, E , in the allowed interval (see figure 5.1) and incorporated into equation 5.15.

The beta background terms were ignored to produce theoretical spectra free of background. Using equation 5.15, transition probabilities, $W(E)$, were calculated and plotted as a function of emission energy. As an example, figure 5.5 shows the theoretical spectrum derived from the D2 deuteron K-Matrix fit where the background effects have been eliminated.

Knowing the overall spectrum shape it is possible to estimate the magnitude of the total ($\alpha + d$) branching ratio. The theoretical spectrum was integrated above the experimental cut-off and integrated over the full energy range. The relationship between the integrated spectrum and the branching ratio is simply:

$$\frac{S_{>525}}{S_{full}} = \frac{BR_{>525}}{BR_{full}} \quad (5.19)$$

where the term $S_{>525}$ is the integrated theoretical spectrum above the cut-off and S_{full} is the total integrated theoretical spectrum. Knowing the value of $BR_{>525}$ from

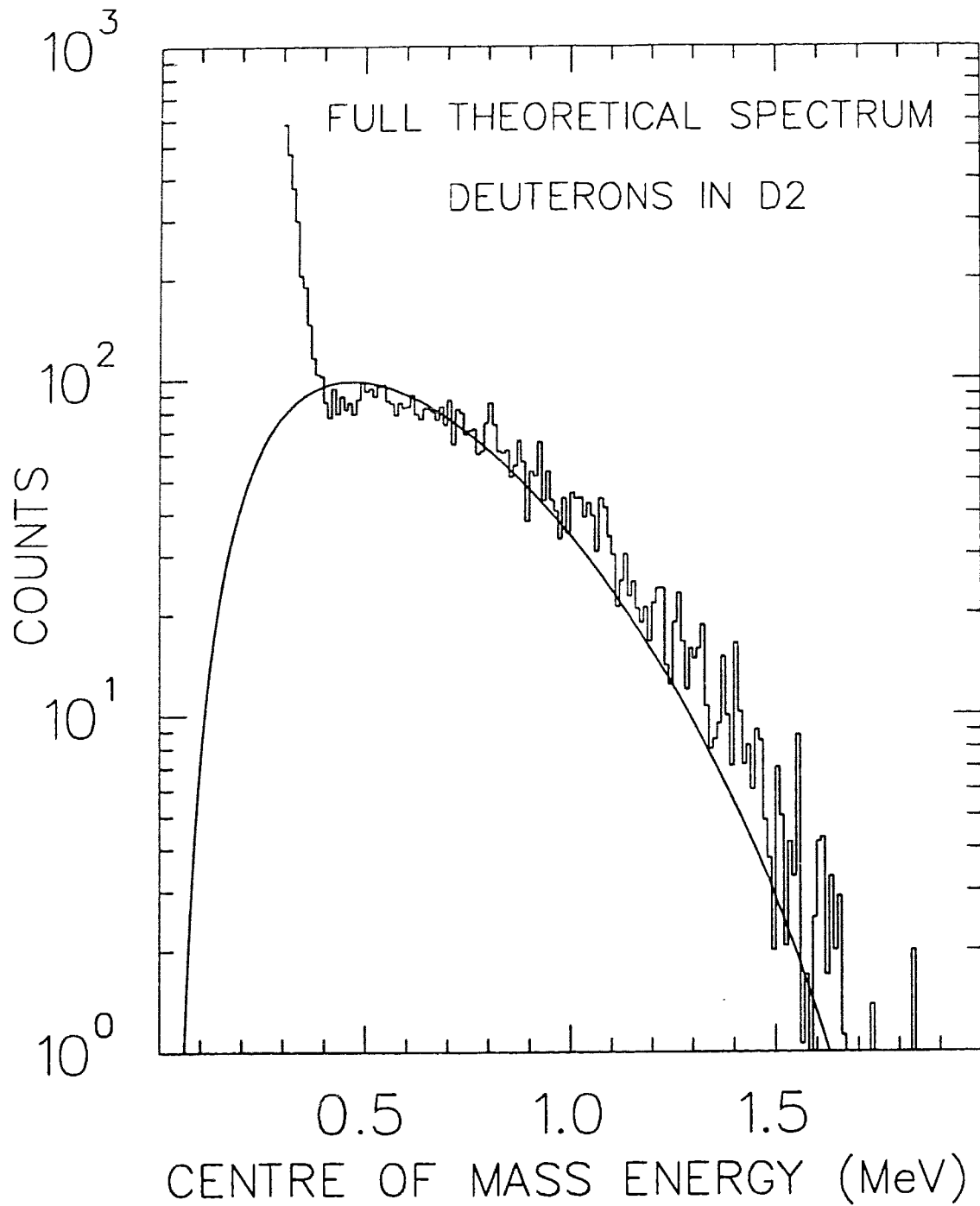


Figure 5.5: Full theoretical deuteron energy spectrum as derived from the best fit K-Matrix parameters

Table 5.2: Calculated value of the Integrated ($\alpha + d$) Branching Ratio

SPECTRUM	BR_{full}	Error
D2 Deuterons	$3.3 * 10^{-6}$	$1.0 * 10^{-6}$
D2 Alphas	$3.3 * 10^{-6}$	$1.0 * 10^{-6}$
D1 Alphas	$3.5 * 10^{-6}$	$1.1 * 10^{-6}$

section 4.7, the equation can be re-arranged to solve for the total ($\alpha + d$) emission probability.

$$BR_{full} = BR_{>525} S_{full}/S_{>525} \quad (5.20)$$

Following this procedure for the deuteron spectrum in D2, the calculated value of the total ($\alpha + d$) branching ratio was found to be $(3.3 \pm 1.0) * 10^{-6}$.

Here, the error in the integrated spectrum was approximated by varying B_0 and g_0 by their fitted uncertainties and re-calculating the ratio of the integrated partial and full spectra. The final error quoted is this uncertainty added in quadrature to the *systematic* error in the branching ratio. This procedure was repeated for each of the three fitted particle energy spectra and the results are listed in table 5.2.

Once again, due to the systematic problems in detector D1, the result for the total ($\alpha + d$) branching ratio derived from this fit is suspect. Furthermore, since the value of the branching ratio above 525 keV is taken from the deuteron measurement in D2, it seems appropriate to report the total ($\alpha + d$) branching ratio from the same spectrum. The reported value for the total ($\alpha + d$) branching ratio in the decay of ${}^6\text{He}$ is then $(3.3 \pm 1.0) * 10^{-6}$.

5.5 Published Theoretical Spectra

As discussed in section 1.4, the experimental deuteron spectrum provides an excellent testing ground for the suitability of theoretical models. By extracting the shape of the published theoretical spectra and overlaying them with the deuteron spectrum collected in this experiment, a first order check of the models' predictions can be ascertained.

Figure 5.6 shows the predicted shape of the deuteron emission spectrum as published by Varga [12]. Here, the magnitude of each energy point was scaled to obtain the best fit to the experimental spectrum. Although the shape is consistent with the experimental spectrum at high energy, the model overestimates the actual spectrum at low energies. In addition, the published branching ratio in this paper is lower than has been observed experimentally. It must therefore be concluded that the model suggested by Varga is not consistent with the observable quantities.

Figure 5.7 shows the theoretical spectrum published by Descouvemont as compared with experiment [10]. Again, the spectrum shape and predicted branching ratio do not reproduce those which have been experimentally determined.

Figure 5.8 shows a similar plot of the theoretically derived spectrum from a paper by Zhukov [11]. The absolute curve does not approximate the observed deuteron spectrum well, however, it appears that if the theoretical spectrum was shifted higher in energy that the fit would improve. It would be interesting to find out which parameters in Zhukov's model control the reference energy of the peak maximum and see if these parameters could be adjusted in a reasonable way to better reproduce the observed spectrum. However, the fact that the branching ratio predicted by Zhukov is much lower than that which is observed may still undermine the suitability of this particular theoretical approach.

Of the published theoretical models, two in particular showed great promise due to the fact that the predicted spectra shapes approximate the observed spectrum quite well. The first of the two was published by Borge *et al.* within their experimental study [9]. The shape of the theoretical spectrum in this paper is scaled and plotted with these new experimental results in figure 5.9.

The theoretical curve appears to underestimate the true spectrum at high energy, however, the similarity between the overall shapes and between the energy values of the peak maxima suggest that the model is at least on the right track. Specifically, the model assumes that the decay proceeds through two virtual states in ${}^6\text{Li}$; one being a virtually excited ${}^6\text{Li}$ ground state and the other being a virtual $(\alpha + 2n)$ state. Each of these states represents a different decay mechanism. The virtual ${}^6\text{Li}$ ground state accounts for a decay by which the beta decay occurs first, followed by

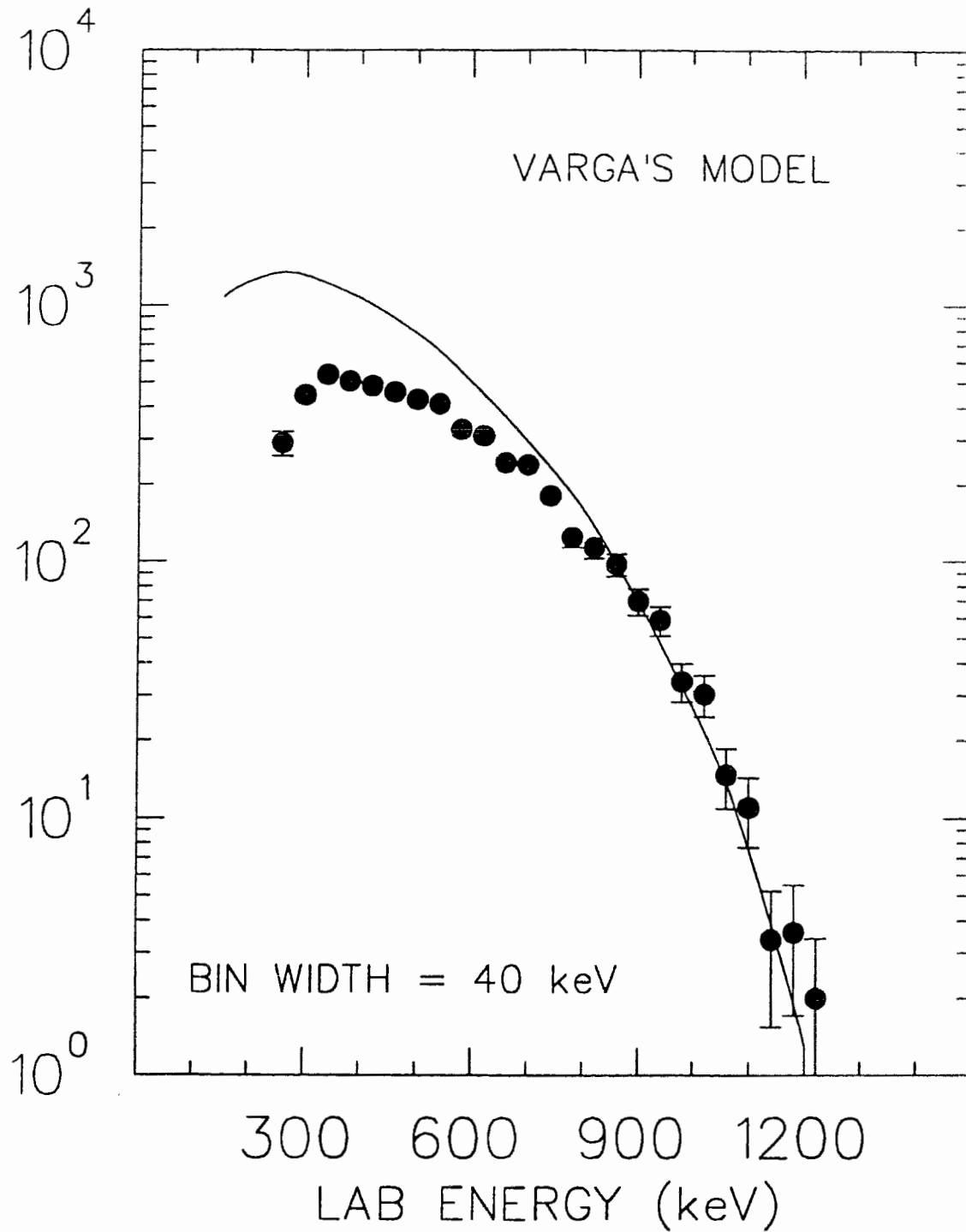


Figure 5.6: Comparison of Varga's theoretical deuteron energy spectrum with that collected experimentally

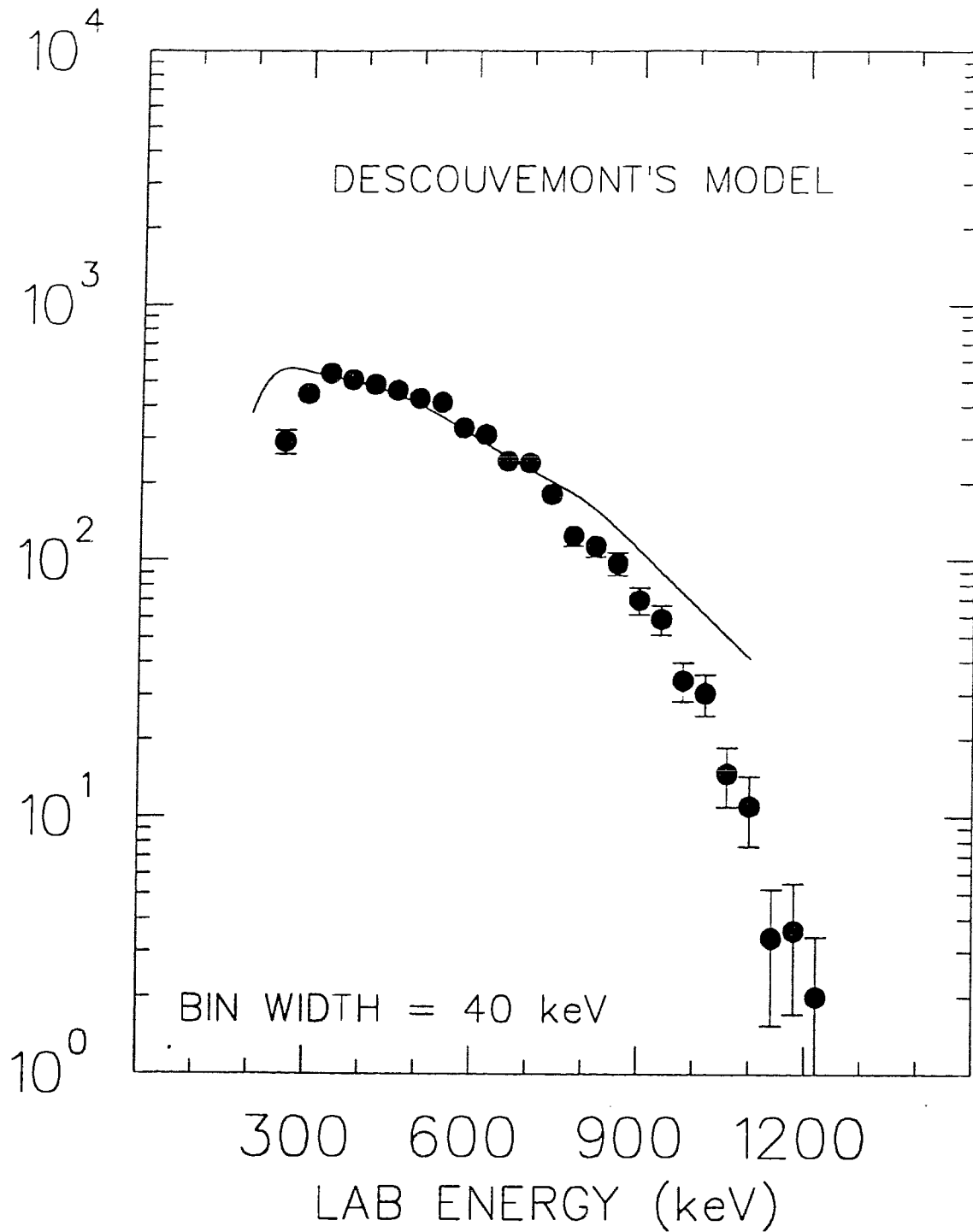


Figure 5.7: Comparison of Descouvemont's theoretical deuteron energy spectrum with that collected experimentally

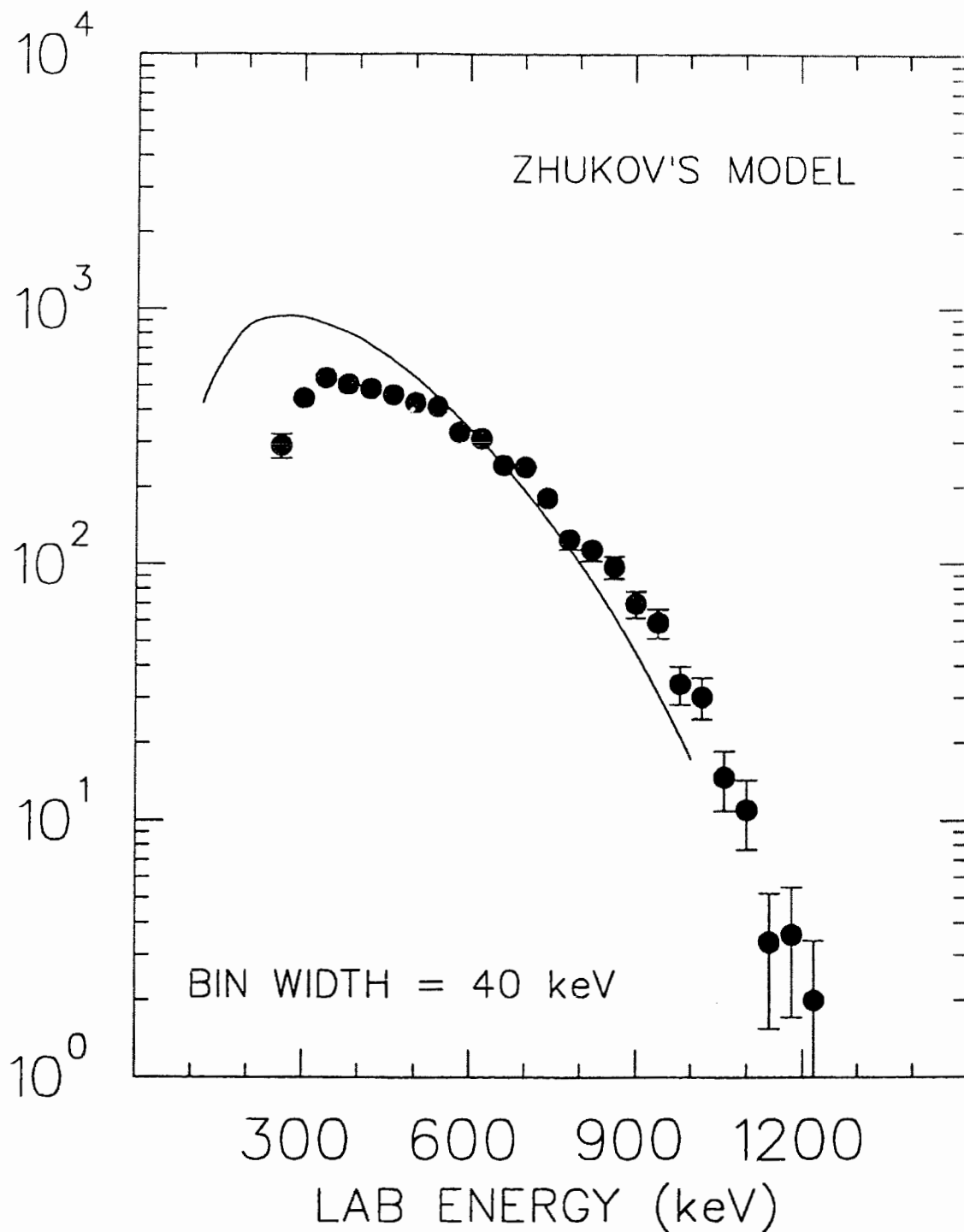


Figure 5.8: Comparison of Zhukov's theoretical deuteron energy spectrum with that collected experimentally

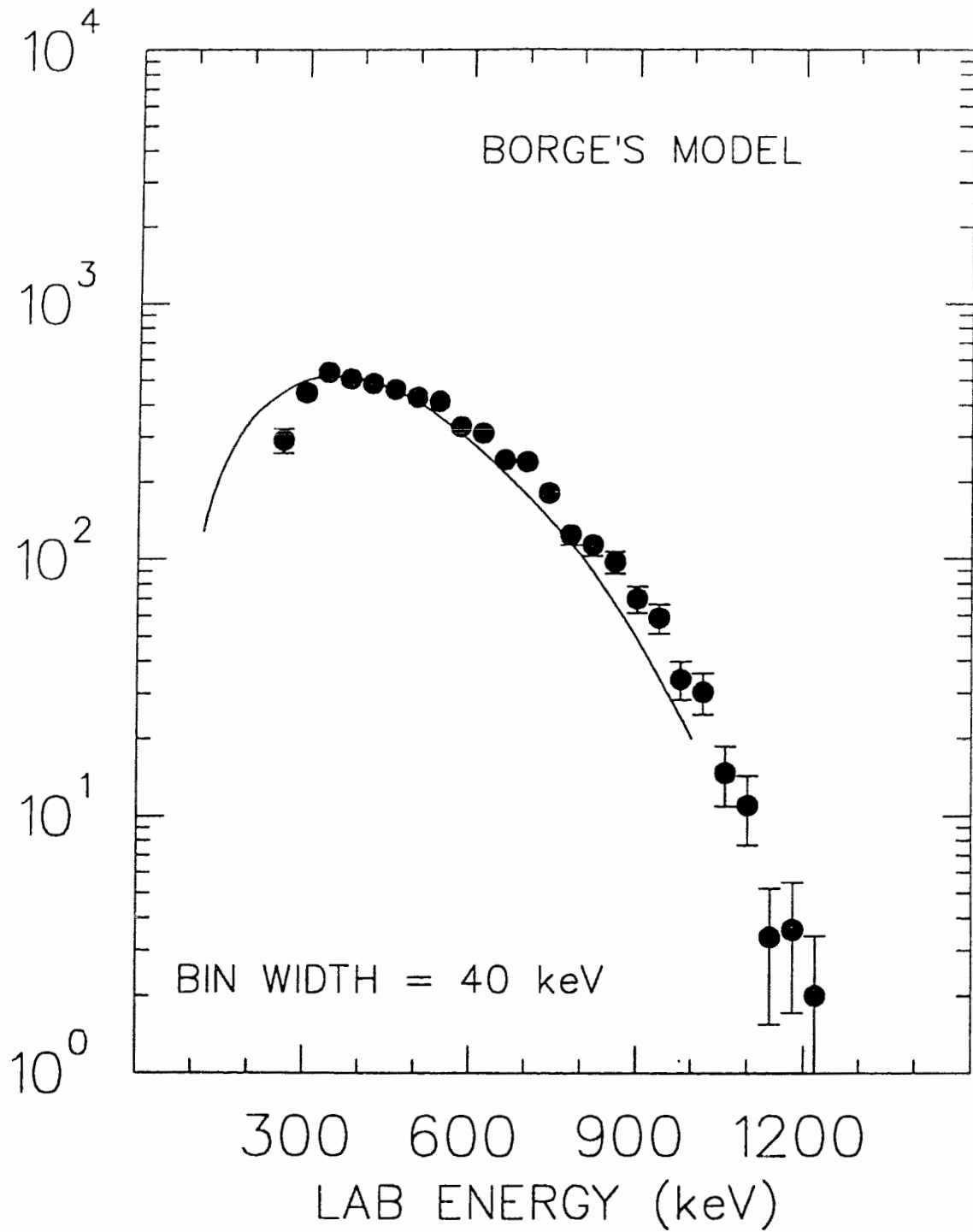


Figure 5.9: Comparison of Borge's theoretical deuteron energy spectrum with that collected experimentally

an $(\alpha + d)$ break-up while the $(\alpha + 2n)$ virtual state accounts for an initial separation of ${}^6\text{He}$ into an alpha plus dineutron followed by the dineutron beta decaying to the unbound state.

The unknown quantity in this theoretical approach was the matrix element (or outgoing amplitude) corresponding to the dineutron/alpha separation and subsequent beta decay, (ξ) . By adjusting the value of the parameter, (ξ) , the authors were able to obtain reasonable agreement with their published experimental spectrum. It would be interesting to investigate whether a magnitude for this parameter could be set such that their theoretical spectrum would better approximate the new deuteron data, and if the predicted branching ratio would be consistent with that observed here.

The second of the two most suitable theoretical spectra was published by Barker [32]. In this work, four possible spectrum shapes were given, each one corresponding to slightly different values for a series of nuclear parameters. Figure 5.10 shows the published spectrum that best approximates the new experimental data.

The parameter values of this theoretical curve correspond to a low channel radius. A low channel radius disagrees with the notion that ${}^6\text{He}$ exists as a neutron halo species. However, his original analysis was based on both the spectrum and branching ratio published by Borge in 1993. Without a direct analysis centred about the new results, it is difficult to draw any definite conclusion regarding the structure of ${}^6\text{He}$.

5.6 Summary

In summary, it is not clear that any conclusions regarding the structure and properties of ${}^6\text{He}$ can be drawn by simply comparing the shapes of the theoretical and experimental spectra. Perhaps the only well-founded observation that can be made on a case by case basis is whether or not the model is supported by the observable features of the ${}^6\text{He}$ break-up. Without an in depth understanding of R-Matrix and to a lesser extent K-Matrix theory, it is not possible to suggest modifications or refinements to the theoretical approaches that would improve the predictions. However, the fact remains that to inspire confidence, the theoretically generated spectra and decay probabilities must echo those which are observed. It is therefore believed that

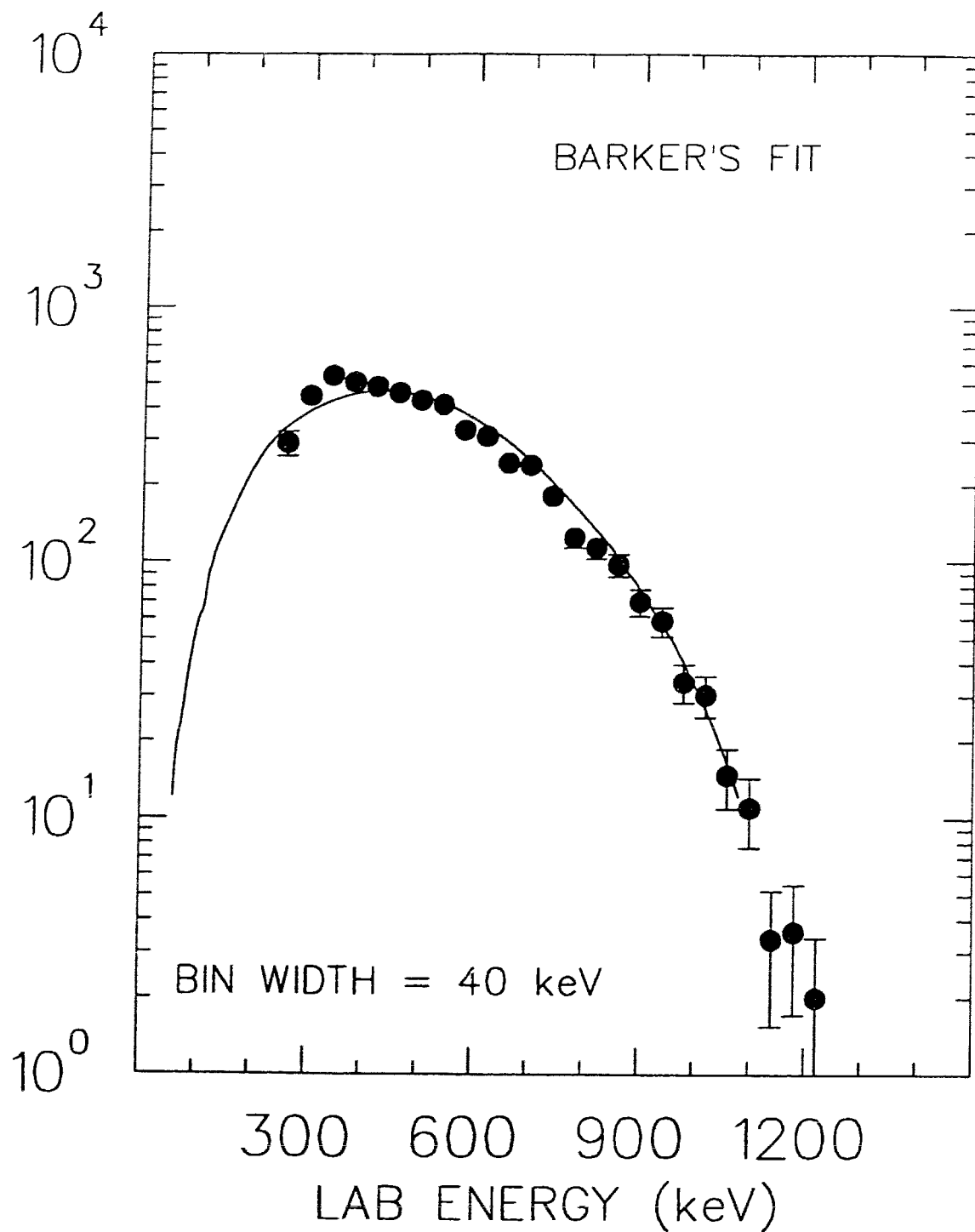


Figure 5.10: Comparison of Barker's theoretical deuteron energy spectrum with that collected experimentally

comparisons against the these new experimental spectra, not unlike those of the preceding section, will lead to a better and more comprehensive theoretical description of the exotic nuclear structure of ${}^6\text{He}$ and its decay properties.

5.7 R-Matrix Analysis

5.7.1 General

Previously published theoretical models were constructed on the basis of branching ratios and particle energy spectra reported by Riisager and Borge [7] [9]. As a consequence, direct comparison of the predictions made from these models and the new data are questionable. To infer any specific structural details with regard to the neutron halo or lack thereof on the basis of these comparisons would be dubious at best.

Because of these difficulties in comparison, the new data were forwarded to F. C. Barker for an R-Matrix analysis independent of the previous experimental measurements. The details of the analysis were identical to the analysis conducted using the Borge data [32] except that, in this case, those parameters that were originally based on the Borge results were exchanged for those reported in this study – namely, the particle energy spectrum and the $(\alpha + d)$ break up probability.

5.7.2 Analysis

The analysis performed by F. C. Barker was a one-level R-Matrix calculation with the ground state of ${}^6\text{Li}$ defined as the intermediate level. The feature of this technique was that the beta decay channel was allowed to contribute to the transition matrix element of the overall decay from the external region [32]. As such, two “cases” were tested in the analysis; the first, case (a), corresponds to the internal contribution dominating the matrix element, while the second, case (b), corresponds to the external contribution dominating the matrix element.

The important parameters in this model were:

$$(M_{if}, m_{if}, A, \theta_i, \theta_f, C_2, \xi)$$

where,

(M_{if}) is the matrix element for the transition between the initial ${}^6\text{He}$ ground state and the final ${}^6\text{Li}$ ground state,

(m_{if}) is the matrix element for the transition between an initial dineutron and final deuteron,

(A) is the channel radius measured in fermi which corresponds to the radial distance at which the polarizing interaction between the two particles is zero,

(θ_i) and (θ_f) are the reduced width amplitudes of the ${}^6\text{He}$ to ${}^6\text{Li}$ and dineutron to deuteron transitions,

(C_2) is a constant parameter given by,

$$C_2 = 2\theta_i\theta_f * m_{if}/M_{if} \quad (5.21)$$

and ξ is a parameter related to the matrix elements by the expression,

$$\xi = C_2/(2\theta_f^2) = \frac{\theta_i * m_{if}}{\theta_f * M_{if}} \quad (5.22)$$

A total of sixteen R-Matrix fits were performed by Dr. Barker, eight corresponding to case (a) and eight corresponding to case (b). On comparison with the experimental deuteron spectrum, a clear preference could be made for case (a). This in itself represents a significant improvement as no clear preference could be made based on the data supplied by Borge *et al* [32].

Of the eight case (a) theoretical forms, two in particular agreed well with the experimental spectrum. These two best fit curves are shown with the actual deuteron spectrum in figures 5.11 and 5.12. The values of the fitted parameters corresponding to each of these theoretical forms are listed in table 5.3.

5.7.3 Interpretation

The best fit values for the channel radius, ($A = 4.5, 4.6$ fm), are larger than predicted by theory. The expected channel radius is calculated from the equation,

$$A = r_o * (A_1^{1/3} + A_2^{1/3}) \quad (5.23)$$

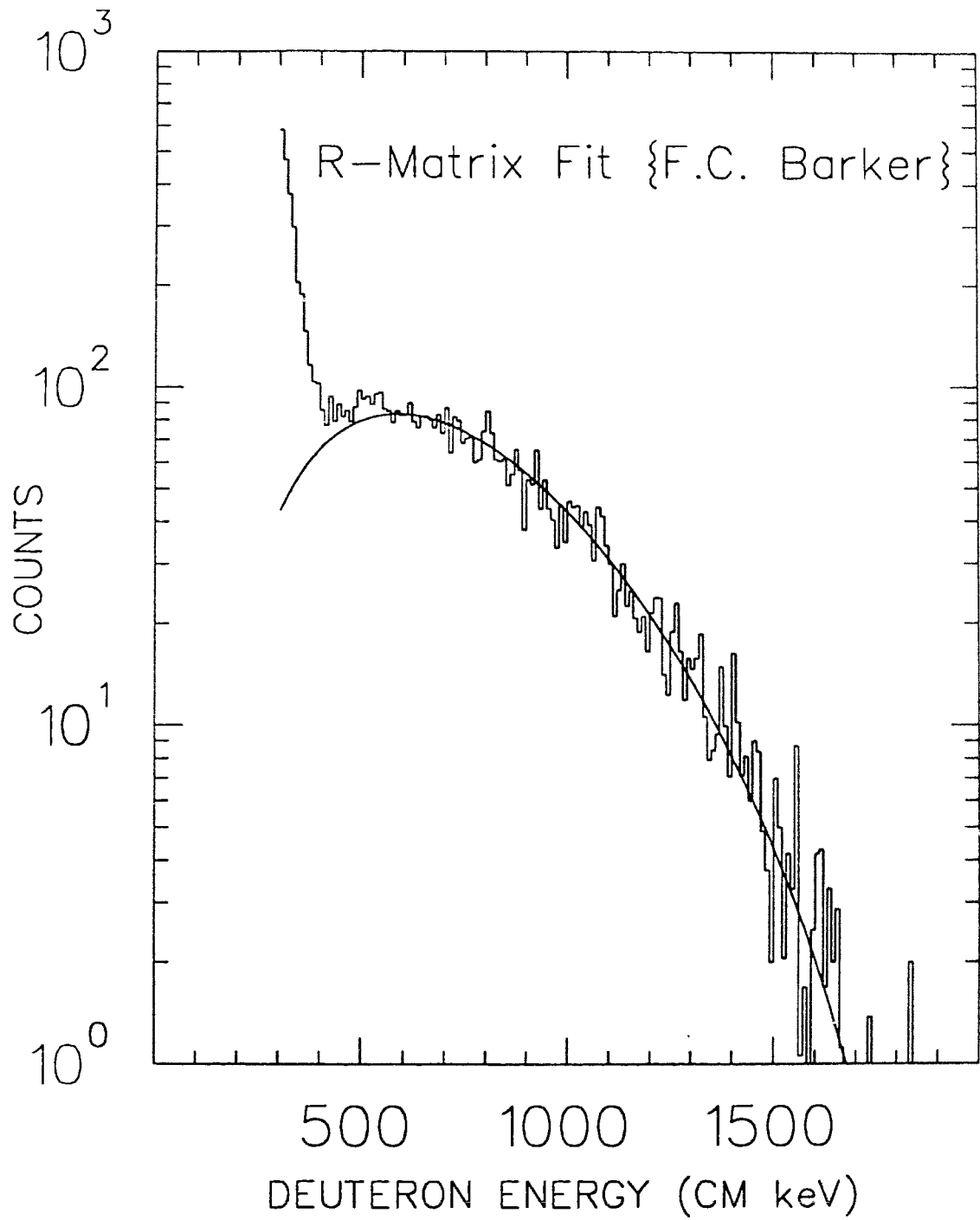


Figure 5.11: Theoretical spectrum corresponding to a channel radius of 4.5 fm

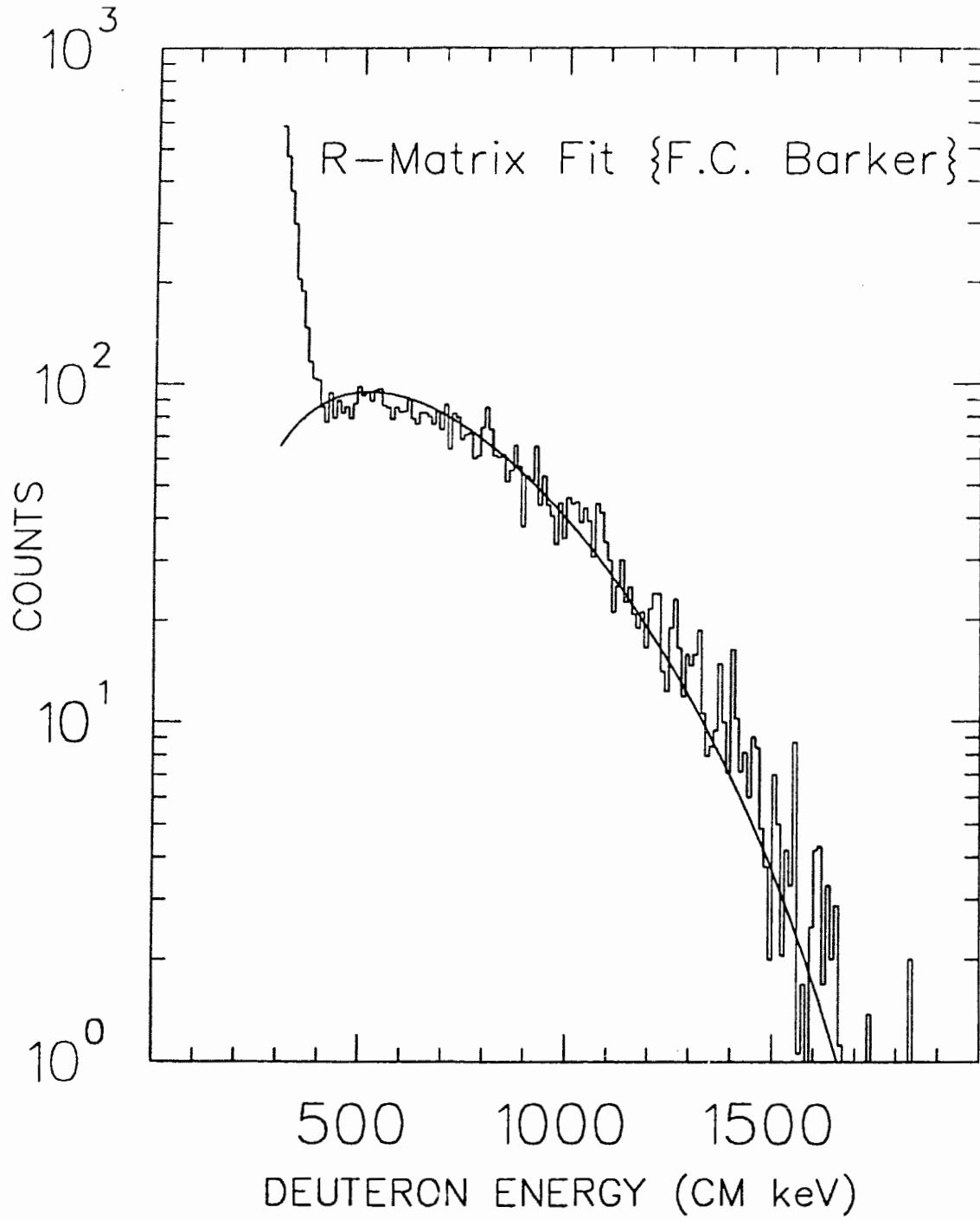


Figure 5.12: Theoretical spectrum corresponding to a channel radius of 4.6 fm

Table 5.3: Best fit parameter values for R-Matrix spectra

Parameter	First Fit (figure 5.11)	Second Fit (figure 5.12)
Case	(a)	(a)
A	4.5 fm	4.6 fm
C_2	0.125	0.069
θ_f^2	0.138	0.0812
ξ	0.45	0.43

where the A_i are the masses of the product alpha and deuteron and the constant of proportionality, r_0 is equal to 1.45 fm. From this equation, the value of the channel radius should be about 4.13 fm. The fact that the fitted values are about 10% larger may indicate that the dimensions of the ${}^6\text{He}$ nucleus are abnormally high, which would be consistent with the hypothesis of a neutron halo. However, the theoretical value of 4.13 fm for the channel radius is a calculated *minimum* [33]. As such it would be difficult to draw any broad conclusions based on the channel radius alone.

The log ft value for the beta transition between the ground states of ${}^6\text{He}$ and ${}^6\text{Li}$ is quoted as being (2.910 ± 0.002) [8]. The low value of log ft corresponds to a large value of the matrix element, M_{if} , for this decay. The large value of M_{if} suggests that the internal wave functions of ${}^6\text{He}$ and ${}^6\text{Li}$ have substantial overlap. Given that the internal wave functions are similar, it is reasonable to assume that the ${}^6\text{He}$ and ${}^6\text{Li}$ reduced width amplitudes are approximately equal [33].

$$\theta_i = \theta_f \quad (5.24)$$

If this is true, then equation 5.22 reduces to,

$$\xi = m_{if}/M_{if} \quad (5.25)$$

The interpretation of the magnitude of ξ is that a high value ($\xi = 1$) would correspond to $m_{if} = M_{if}$. If the matrix elements were about equal then it could be inferred that correlation between the two neutrons in ${}^6\text{He}$ is very similar to the correlation between the nucleons within the deuteron. Extending this idea, it could

be inferred that the outermost neutrons in ${}^6\text{He}$ are deuteron-like. This would suggest a strong coupling to the $(\alpha + d)$ state giving a large branching ratio for deuteron emission.

The other extreme corresponds to a ξ value close to zero. In this picture, the dineutron-to-deuteron matrix element, m_{if} , is much smaller than the overall transition matrix element, M_{if} . In such a case, it could be inferred that the degree of correlation between the outermost neutrons in ${}^6\text{He}$ is much different (less than) the correlation between the two nucleons in the deuteron. This case would support the uncorrelated neutron description of ${}^6\text{He}$ which would tend to support the neutron halo hypothesis and result in a substantially smaller branching ratio for deuteron emission.

The best fit values for ξ were found to be about (0.44). This suggests that the degree of correlation between the two neutrons in ${}^6\text{He}$ is moderately large, but not obviously deuteron or halo-like.

5.7.4 Summary

The R-Matrix analysis conducted by Barker does not conclusively identify ${}^6\text{He}$ as a neutron halo species. The results indicate that the structure of the ${}^6\text{He}$ nuclide is somewhere in between the conventional and halo descriptions. In fact, this is not inconsistent with what has been postulated previously. Of the nuclides that have been shown to have neutron distributions larger than predicted by the constant density approximation, some show higher degrees of neutron dispersal than others. Those with extremely large density distributions, such as ${}^{11}\text{Li}$, are more correctly described as 'neutron halo' isotopes, while others, such as ${}^6\text{He}$, with smaller neutron distributions, have become known as 'neutron skin' species [34]. The difference between the two being the extent of the neutron cloud, however the boundaries for the classification of a nuclide as belonging to one group or the other have not been clearly established.

From the theoretical R-Matrix forms that best fit the experimentally collected deuteron spectrum, the total branching ratio for deuteron emission has been estimated. Integration of the two best fit curves indicates that the overall branching ratio for deuteron emission from ${}^6\text{He}$ is about $(2.9 \pm 0.9) * 10^{-6}$.

Chapter 6

Summary and Conclusions

${}^6\text{He}$ is an exotic species that has been observed to exhibit an anomalous neutron density distribution and a unique decay mode through which a beta-delayed deuteron is emitted. Previous experimental measurements of the probability for deuteron emission are not self-consistent while the published particle energy spectra suffer from the fact that they are of poor statistical reliability [7] [9]. Although it is *always* desirable to have accurate measurements of these standard decay characteristics, it is particularly important that the ${}^6\text{He}$ nuclide have a believable branching ratio and consistent particle energy spectra due to the fact that these quantities may be sensitive probes of the so-called 'Neutron Halo' phenomenon.

An experiment was performed by the TISOL group at TRIUMF to re-measure the branching ratio for $(\alpha + d)$ break-up and to generate the particle energy spectra of the emitted species. The $(\alpha + d)$ break-up was monitored by a coincidence technique which enabled conclusive separation of alphas and deuterons down to low energies. The deuteron spectrum collected by this method is statistically better than the previously published spectra by more than an order of magnitude.

From the collected deuteron and beta particle data, the probability of ${}^6\text{He}$ emitting a deuteron with a laboratory energy in excess of 350 keV has been measured to be $(1.9 \pm 0.2 \pm 0.7) * 10^{-6}$. This result conflicts with the currently quoted branching ratio value of $(7.6 \pm 0.6) * 10^{-6}$ but is consistent with the original measurement of $(2.8 \pm 0.5) * 10^{-6}$ when the difference in the experimental energy cut-off is taken into

account.

Extracting the pertinent elements of K-Matrix reaction theory, the deuteron and alpha spectra were fit with theoretical forms and extended over the full energy range of the transition. From these theoretical spectra, the total ($\alpha + d$) branching ratio has been estimated to be $(3.3 \pm 1.0) * 10^{-6}$.

Using an R-Matrix analysis conducted by F. C. Barker, the experimental deuteron spectrum was fit to a number of theoretical forms and two specific theoretical 'cases'. The results of the analysis showed a clear preference for theoretical forms of case (a); a preference that could not be deduced on the basis of the previously published data. The two theoretical curves that best approximated the experimental data yield full ($\alpha + d$) branching ratios of approximately $(2.9 \pm 0.9) * 10^{-6}$ for the break-up transition in the decay of ${}^6\text{He}$.

If the systematic difficulties experienced during this experiment are a barrier to the publication of the branching ratio result, it may be deemed necessary to re-measure the deuteron emission probability at a later date. Should this come to pass, there are recommendations to be made with regard to the experimental set-up. First, rather than employing a telescope design for beta detection, individual beta counters, such as those of the silicon or scintillator variety, may be superior for this particular measurement. Second, it would be desirable to use more than one beta detector so that efficiency calculations may be compared and contrasted, based on their relative geometries, and investigated for systematic differences that may not otherwise be illuminated. Third, the use of hardware coincidences should be avoided due to the fact that it is not possible to repair in the software, potential problems set by the hardware. And, fourth, since yield was not a factor in the experiment, the relative source/detector geometry should be arranged such that variations in the dimensions and position of the source activity do not create such dramatic changes in the detection efficiencies. This could be accomplished by passing the ${}^6\text{He}$ ion beam through a very small collimator immediately prior to implantation within the carbon collection foil, and by using particle detectors D1 and D2 with larger surface areas located at greater distances from the source. With large enough detectors, the geometric efficiencies would not be reduced, but the error caused by source movement would be minimized.

It was hoped that the results of this experiment would conclusively demonstrate that the ${}^6\text{He}$ nuclide was or was not a neutron halo species. The results, however, indicate that the structure of the ${}^6\text{He}$ nuclide is neither halo-like nor conventional. It appears that the previous classification of ${}^6\text{He}$ as a 'neutron skin' isotope is not inconsistent with these latest data.

Bibliography

- [1] I. Tanihata, H. Hamagaki, O. Hashimoto, Y. Shida, N. Yoshikawa, K. Sugimoto, O. Yamakawa, T. Kobayashi, N. Takahashi, *Phys. Rev. Lett.* **55** 2676 (1985).
- [2] P. G. Hansen, B. Jonson, *Europhys. Lett. A.* **4** 409 (1987).
- [3] H. Sagawa, *Phys. Lett. B.* **286** 7 (1992).
- [4] M. V. Zhukov, B. V. Danilin, D. V. Fedorov, J. S. Vaagen, F. A. Gareev, J. Bang, *Phys. Lett. B.* **265** 9 (1991).
- [5] M. V. Zhukov, D. V. Fedorov, B. V. Danilin, J. S. Vaagen, J. M. Bang, I. J. Thompson, *Nucl. Phys. A.* **552** 353 (1993).
- [6] T. Kobayashi, O. Yamakawa, K. Omata, K. Sugimoto, T. Shimoda, N. Takahashi, I. Tanihata, *Phys. Rev. Lett.* **60** 2599 (1988).
- [7] K. Riisager, M. Borge, H. Gabelmann, P. Hansen, L. Johannsen, B. Jonson, W. Kircewicz, G. Nyman, A. Richter, O. Tengblad, K. Wilhelmsen, *Phys. Lett. B.* **235** 30 (1990).
- [8] F. Ajzenberg-Selove, *Nucl. Phys. A.* **490** 1 (1988).
- [9] M. Borge, L. Johannsen, B. Jonson, T. Nilsson, G. Nyman, K. Riisager, O. Tengblad, K. Wilhelmsen Rolander, *Nucl. Phys. A.* **560** 664 (1993).
- [10] P. Descouvemont, C. Leclercq-Willain, *J. Phys. G: Nucl. Part. Phys.* **18** L99 (1992).

- [11] M. Zhukov, B. Danilin, L. Grigorenko, N. Shul'gina, *Phys. Rev. C.* **47** 2937 (1993).
- [12] K. Varga, Y. Suzuki, Y. Ohbayashi, *Phys. Rev. C.* **50** 189 (1994).
- [13] A. Csoto, D. Baye, *Phys. Rev. C.* **49** 818 (1994).
- [14] M. Dombisky, L. Buchmann, J. M. D'Auria, P. McNeely, G. Roy, H. Sprenger, J. Vincent, *Nucl. Instr. Meth. B.* **70** 125 (1992).
- [15] L. Buchmann, J. Vincent, H. Sprenger, M. Dombisky, J. M. D'Auria, P. McNeely, G. Roy, *Nucl. Instr. Meth. B.* **62** 521 (1991).
- [16] P. McNeely, G. Roy, J. Soukup, J. M. D'Auria, L. Buchmann, M. McDonald, P. W. Schmor, J. Vincent, *Rev. Sci. Inst.* **61** 273 (1990).
- [17] M. Dombisky, J. M. D'Auria, L. Buchmann, H. Sprenger, J. Vincent, P. McNeely, G. Roy, *Nucl. Instr. Meth. A.* **295** 291 (1990).
- [18] L. Buchmann, R. E. Azuma, C. A. Barnes, J. M. D'Auria, M. Dombisky, U. Giesen, K. P. Jackson, J. D. King, R. Korteling, P. McNeely, J. Powell, G. Roy, J. Vincent, S. S. M. Wong, P. R. Wrean, *Nucl. Instr. Meth. B.* **79** 330 (1993).
- [19] P. W. Green, TRIUMF/University of Alberta files: TRI-DNA-91-1, "Introduction to the NOVA Data Analysis System", TRI-DNA-91-2, "Summary of NOVA Commands"; TRI-DNA-91-3, "The NOVA Operation Sequence (opseq)" (unpublished).
- [20] J. L. Chuma, TRIUMF files: TRI-CD-87-03b, "PLOTDATA Command Reference Manual"; (unpublished).
- [21] Z. Zhao, M. Gai, B. J. Lund, S. L. Rugari, D. Mikolas, B. A. Brown, J. A. Nolan, Jr., M. Samuel, *Phys. Rev. C.* **29** 39 (1985).
- [22] D. R. Tilley, H. R. Weller, C. M. Cheves, *Nucl. Phys. A.* **564** 1 (1993).

- [23] J. F. Ziegler, J. P. Biersack, "The Stopping Power and Range of Ions in Solids", Pergamon Press, (1990).
- [24] K. Krane, "Introductory Nuclear Physics"; John Wiley and Sons, (1988).
- [25] J. D'Auria, J. King, U. Giesen, (private communication).
- [26] W. R. Leo, "Techniques for Nuclear and Particle Physics Experiments" Springer-Verlag Heidelberg (1992).
- [27] K. Siegbahn, "Alpha- Beta- and Gamma- Ray Spectroscopy", North-Holland Publishing Company (1974).
- [28] J. D. Powell, *Ph.D. Thesis*; Department of Physics, University of Toronto, (1995).
- [29] B. W. Filipone, J. Humblet, K. Langanke, *Phys. Rev. C.* **40** 515 (1989).
- [30] J. Humblet, *Phys. Rev. C.* **42** 1582 (1990).
- [31] "MINUIT, Function Minimization and Error Analysis", CERN Program Library Entry D506 (unpublished).
- [32] F. Barker, *Phys. Lett. B.* **322** 17 (1994).
- [33] F. C. Barker, private communication
- [34] K. Riisager, *Rev. Mod. Phys.* **66** 1105 (1994).
- [35] R. Boyd, *Int. Jour. Mod. Phys. E.* **3** 249 (1994).
- [36] I. Tanihata, H. Hamagashi, O. Hashimoto, S. Nagamiya, Y. Shida, N. Yoshikawa, O. Yamakawa, K. Sugimoto, T. Kobayashi, D. E. Greiner, N. Takahashi, Y. Nojiri, *Phys. Lett. B.* **160** 380 (1985).
- [37] N. Jelley, "Fundamentals of Nuclear Physics"; Cambridge University Press, (1990).